Interactions between Ice Sheets, Climate and the solid Earth

Interacties tussen ijskappen, klimaat en de vaste aarde

(met een samenvatting in het Nederlands)

PROEFSCHRIFT

ter verkrijging van de graad van doctor aan de Universiteit Utrecht
op gezag van de rector magnificus, prof. dr. W.H. Gispen,
ingevolge het besluit van het college voor promoties
in het openbaar te verdedigen op
maandag 21 mei 2007 des middags te 12.45 uur

door

Jojanneke van den Berg

geboren op 31 juli 1979, te Gouda

Promotor: Prof. Dr. J. Oerlemans
Copromotor: Dr. R.S.W. van de Wal

Financial support was provided by NWO through the Spinoza grant awarded to Prof. Dr. J. Oerlemans

In the bleak midwinter Frosty wind made moan
Earth stood hard as iron, Water like a stone;
Snow had fallen, snow on snow,
Snow on snow, In the bleak midwinter
Long ago

Christina Rossetti, A Christmas Carol
English poet (1830-1894)

Members of the dissertation committee:

Dr. H. Gudmundsson
British Antarctic Survey

Dr. G.A. Milne
Department of Earth Sciences,
Durham University

Prof. Dr. Ir. J.D. Opsteegh
Institute for Marine and Atmospheric research Utrecht,
Utrecht University

Prof. Dr. M.J.R. Wortel
Department of Earth Sciences,
Utrecht University

Contents

Chapter 1

Introduction

Climate change is one of today's most discussed topics. The earth's atmosphere works as a greenhouse in the sense that greenhouse gases, like carbon dioxide, water vapour and methane, essentially trap the radiation emitted by the earth's surface, thereby storing heat and eventually warming the surface. Without this greenhouse effect the surface would on average be about 30 degrees cooler than it is now. At present, the burning of hydrocarbons releases additional greenhouse gases,which increases the atmosphere's ability to warm the surface. These few extra degrees affect climate worldwide. For example, rising temperatures warm the sea water and melt ice sheets causing relative sea level rise. This is of particular interest to the coastal regions, which are amongst the most densely populated areas in the world. This is illustrated by Figure 1.1 which shows a cartoon from a Dutch newspaper. The cartoon shows the national airport Schiphol completely flooded as a result of sea level rise.

Observations of relative sea level rise are important indicators for the current state of balance of the Antarctic and the Greenland Ice Sheets. The response of relative sea level to changes in the ice sheets is the result of several interacting physical processes. Figure 1.2 shows a schematic representation of the total system with the principal components and their mutual interactions. The moisture required to create ice sheets is evaporated from the ocean, lowering relative sea level. Ice sheets form if the climate conditions are such that the precipitation is in the form of snow that does not completely melt over summer. The ice sheet represents a huge mass which influences the solid earth by pushing down the crust, a process called isostatic adjustment. This lowering of the surface influences the geometry and size of the ice sheet and thereby indirectly influences relative sea level. Melting ice sheets directly affect relative sea level by returning water to the ocean. Thus, a change in any of the individual components in the ice sheet system affects all the others.

In this thesis, we focus on the dynamical interactions between ice sheets, the climate, and the solid earth. Within this framework, observations of relative sea level change are direct indicators of a changing climate as the ice masses respond to changes in temperature and precipitation. In addition, observational records of past relative sea level changes are an important source of information on the size and geometry of the ice sheets of the past.

Figure 1.1: Cartoon on consequences of climate change in The Netherlands, Fokke en Sukke, NRC. Picture courtesy of J. Reid, B. Geleijnse and J.-M. van Tol.

1.1 Principles of relative sea level change

Relative sea level may rise due to (i) changes in ocean volume and (ii) vertical movement of the land, for example due to tectonics, erosion, or isostatic adjustment. An observer on land cannot distinguish the two effects, see Figure 1.3. The top figure shows the sea level rise due to the melting of ice sheets. When an ice sheet melts it directly adds water to the ocean, thereby changing the ocean volume. If we neglect the gravitational response of the water and changes in the water density, this increases sea level by an amount which is generally called the eustatic sea level change. The bottom figure shows the effect of subsidence of the land. In both cases sea level rises relative to point A. Most available sea level data are relative, that is we can only measure sea level change with respect to a reference level, usually present day sea level. This means we have to assess the cause of the relative change for each measurement.

Isostatic adjustment is an example of vertical land movement with significant influence on relative sea level measurements in regions formerly covered with ice. It is the response of the solid earth to changes in the weight of ice sheets. Over long time scales the earth's material behaves like a fluid. Therefore, the earth responds to the weight of ice sheets similar to a ship in water. According to Archimedes law the ship displaces a volume of water equal to the weight of the ship. When an ice sheet forms on the surface the land will move down under the weight. In case of melting of ice sheets, the earth rebounds.

A clear example of rebound can be observed in Scandinavia where the land has been uplifting extensively due to the melting of the last ice sheet roughly 20,000 years ago. The

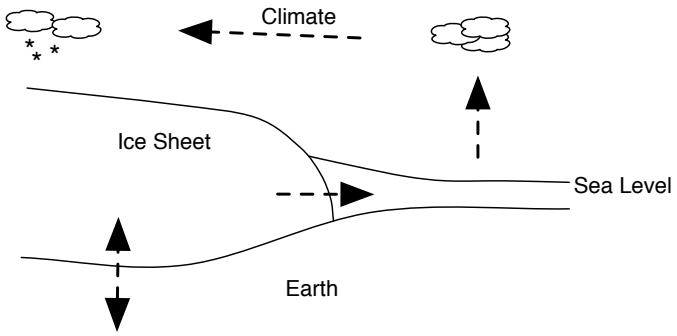

Figure 1.2: Schematic representation of the ice sheet system with the most important components and their mutual interactions.

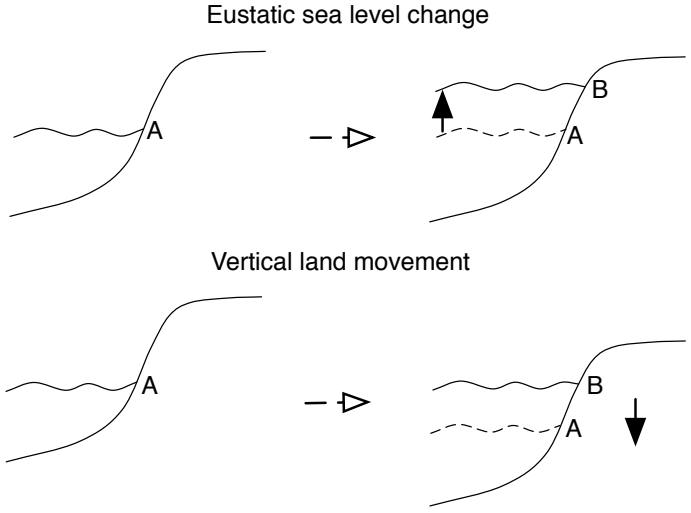

Figure 1.3: Examples of relative sea level rise. The upper and lower panel show a similar relative sea level rise for a local observer. However, the rise in the upper panel is caused by a eustatic change in sea level, whereas the rise in the lower panel is caused by vertical land movement.

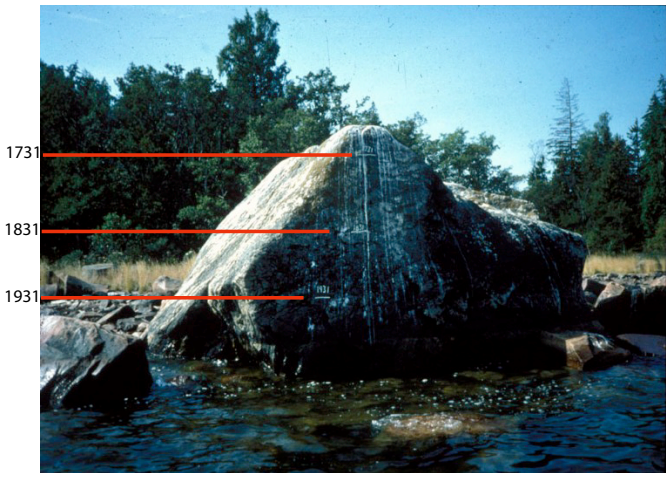

Figure 1.4: Picture of rock in Lövgrund in southwestern Sweden with several sea level marks. Picture courtesy of Prof. K. Lambeck.

rate of uplift exceeds the rate of sea level rise due to the addition of melt water, resulting in a relative sea level fall. Figure 1.4 shows a rock in Lövgrund in southwestern Sweden. In 1731 the Swedish scientist Anders Celsius made a mark indicating the sea level at that time. In 1831 the geologist Lyell made a new mark and it was this mark in combination with other data in the Baltic area that convinced Lyell in 1835 that in fact the land was uplifting rather than that the sea was falling. This eventually led to the concept of isostatic adjustment (e.g. Watts, 2001; Turcotte and Schubert, 2002).

Changes in ocean volume occur mainly as a result of melting or growing of ice sheets and glaciers, and thermal expansion of the water. Here I focus on large scale ice sheets on the time scale of ice ages. We neglect the effects of thermal expansion. Figure 1.5 shows what happens to sea level if one meter from all the ice sheets existing around 20,000 years ago in the Northern Hemisphere melted instantaneously. The top plot shows the ice distribution with large ice sheets over Europe, Greenland and North America. The ice sheets over North America and Europe are usually called the Laurentide and the Fennoscandian or Eurasian Ice sheets respectively. The middle plot shows the instantaneous relative sea level change as a result of the melting. The lower plot shows the relative sea level change 1000 years later. The sea level changes are shown as percentages of the eustatic rise. A value of 100 percent means the relative sea level rise was equal to the eustatic rise, a value lower or higher than 100 means a relative sea level rise smaller or larger than the eustatic rise, a value lower than zero means a relative sea level fall. The figure clearly demonstrates that the melt water is not distributed evenly over the ocean. The relative sea level far from the ice sheets rises more than in the vicinity of the ice sheets. Close to the ice sheets the melting of ice even causes a relative sea level fall instead of a sea level rise.

This is caused by the gravitational attraction of water to mass and by the elastic response of the earth, which is that part of the isostatic adjustment which happens instantaneously. Sea level always coincides with an equipotential surface in the earth's gravity field. The mass distribution on the earth's surface is affected by the growth and decay of ice sheets. When ice melts its gravitational pull decreases resulting in a lowering of the relative sea level near the former ice sheet and a relative sea level rise in regions far away from the former ice sheet. The differences between the middle and lower plot in Figure 1.5 are caused by the non-elastic part of the isostatic adjustment which has relaxation times on the order of 10,000 years. In the vicinity of the ice sheets we see a continuing relative sea level fall caused by the rebound in combination with attraction of water to deep ocean basins causing a subsidence of the sea floor.

Present day relative sea level responds both to current and to past climate changes. Melt water released from the large ice sheets and the consequent rebound of the underlying land around 20,000 years ago still influences modern day sea level adjustment.

Each ice sheet has a different geometry and geographical location. As a result, each ice sheet produces a characteristic spatial pattern of sea level change over the globe. Relative sea level change at any given location is an addition of the contributions of the individual ice masses. Observations from many locations can be inverted for the individual contributions using these characteristic patterns. In this way the melt water fluxes from for example the Greenland and Antarctic Ice Sheets can be estimated as a function of time (e.g. Mitrovica et al., 2001; Clark et al., 2002; Tamiseia et al., 2003).

1.2 Ice history

Figure 1.6 shows sea level records from a number of locations in Europe for the last 300 years as published by the third IPCC climate assessment report (2001). We see many short term fluctuations, but overall there is a general trend of relative sea level rise of about 0.5-1 mm/yr. This European trend is not necessarily globally representative as explained in the previous section.

According to the fourth IPCC climate assessment report (2007) the sea level over the 20th century has risen globally at a rate of 1.7 ± 0.5 mm/yr. Over the last 30 years, the rate was 1.8 ± 0.5 mm/yr increasing to 3.1 ± 0.7 mm/yr over the last 10 years. This means a substantial increase over the course of the 20th century. The most important contributions to the observed sea level change are thermal expansion of the ocean water and the loss of land ice. Between 1960 and 2003 small glaciers contributed 0.5 ± 0.2 mm/yr, and Greenland and Antarctica 1.9 ± 5.3 mm/yr. The largest part and the greatest uncertainty in the latter number is caused by the long term adjustment of the ice sheets to past climate conditions.

The IPCC report (2007) predicts that the contribution from Greenland and Antarctica to sea level rise will grow if temperatures continue to rise. To accurately predict future sea level changes it is essential to reduce the uncertainty in the contributions from Greenland and Antarctica. To accomplish that we need to study the ice sheets throughout the ice ages. Firstly, the uncertainty in the long term response of Greenland and Antarctica can

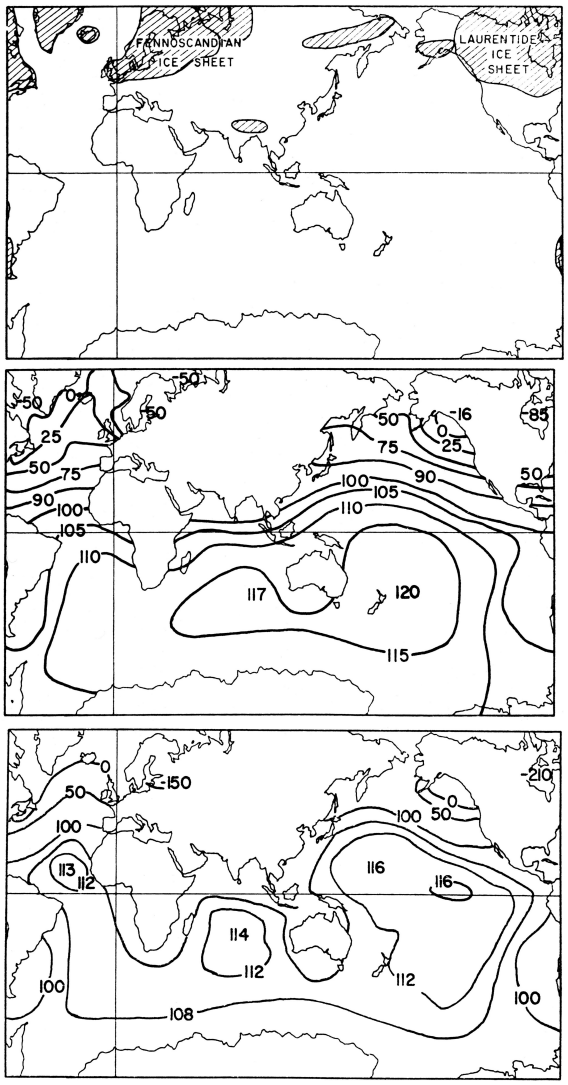

Figure 1.5: The top plot shows the configuration of ice masses used by Farrel and Clark (1976). The middle plot shows the percentage instantaneous change relative to the eustatic sea level change in sea level when 1 meter of ice melts from all shaded areas in the top plot. The lower plot shows the same as the middle plot, but now after 1000 years.

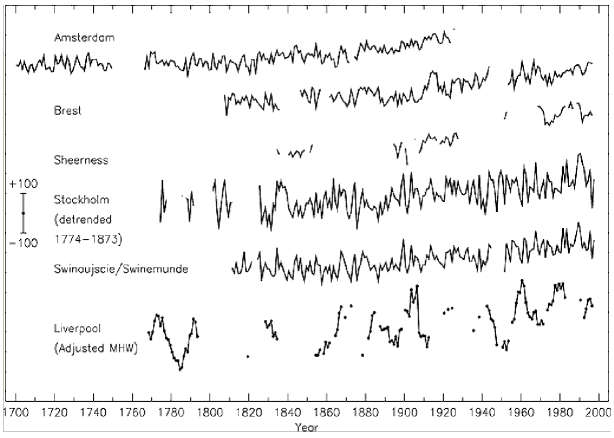

Figure 1.6: Time-series of relative sea level for the past 300 years from Northern Europe: Amsterdam, the Netherlands; Brest, France; Sheerness, UK; Stockholm, Sweden (detrended over the period 1774 to 1873 to remove the first order contribution of isostatic rebound); Swinoujscie, Poland; and Liverpool, UK. figure from the third IPCC climate assessment report (2001).

only be reduced by studying the past. Secondly, understanding of the processes governing the response of ice sheets to climate changes is essential to predict the response of the ice sheets to present and future climate changes. The growth and decay of large ice sheets were among the largest climate changes in the last million years. Figure 1.7 shows the ice cover around the Last Glacial Maximum and present day for both the hemispheres. The ice sheets of the last ice age lowered eustatic sea level with 130 meters. By comparison, if Antarctica would melt today, this causes a eustatic sea level rise of about 60 meters. Within a time period of less than 10,000 years the ice sheets on the Northern Hemisphere, except Greenland, melted, thereby returning this 130 meters to the ocean. The study of these major changes provides important knowledge on the physical processes driving the way ice sheets respond to climate changes in general.

1.2.1 Data

Information on past ice sheets and climate comes from many sources. Ice cores, for example, give information on past atmospheric composition through enclosed air bubbles and the isotopic composition of the ice provides a measure of paleotemperatures (e.g. Grootes et al., 1993; Petit et al., 1999; EPICA Community Members, 2004). Figure 1.8 shows data from Dome C, Antarctica. This is the core with the oldest ice on record today with ice of nearly one million years old. The figure shows a series of approximately 800,000 years. The plots compare data from the Dome C ice core with data from another Antarctic ice core, Vostok and marine sediment cores. All isotopic data show the occurrence of

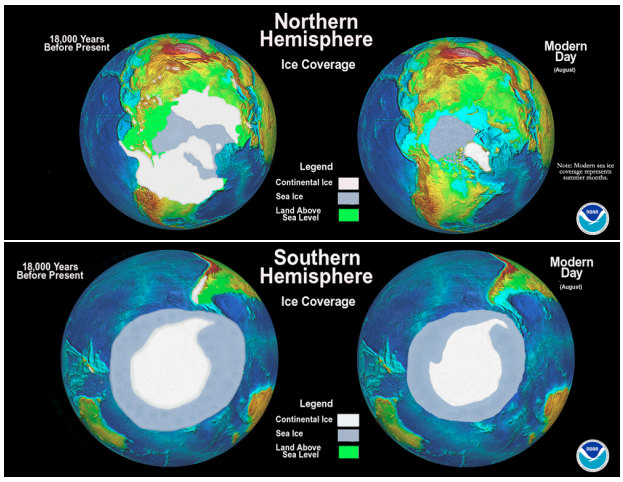

Figure 1.7: Ice cover at the LGM and present day. Pictures courtesy of Marc McCaffrey and the NOAAA Paleoclimatology Program/Department of commerce.

several ice ages with a long slow increase of ice age conditions followed by rapid return to interglacial conditions. From the isotopic measurements a temperature difference with respect to present day conditions can be estimated. The dust records also show a clear distinction between glacial and interglacial periods, with the glacial periods having peaks in the dust concentrations.

Besides ice cores we also know a lot about the past climate and ice sheet extent from geomorphological features. There are many indications in the landscape on past ice sheet geometries and relative sea level. Figure 1.9 shows some examples. Flowing glaciers tend to sculpture the landscape. The ice erodes the bedrock, taking rocks and gravel along with the flow. The gravel polishes the bedrock leaving behind smooth rocks often covered with striae where larger boulders have cut into the rocks. When an ice sheet retreats it leaves a very characteristic landscape behind; smooth elongated hills of glacial debris (drumlins), gravel left behind in flutes and eskers revealing the flow directions. Boulders left as erratics reveal ice extent as do moraine leftovers. Turbulent melt water leaves holes, so-called kettles.

Relative sea level records

An important class of geomorphological indicators of past ice sheet extent are relative sea level measurements. There are many types of these measurements, such as beach deposits, fossil organisms trapped in the sediments, the sediment patterns themselves, for example in salt water marshes and isolation basins, and many more. The reliability and accuracy of these data depend on how well they can be dated and their indicative meaning (e.g. Van de Plassche, 1986). This indicative meaning describes the vertical

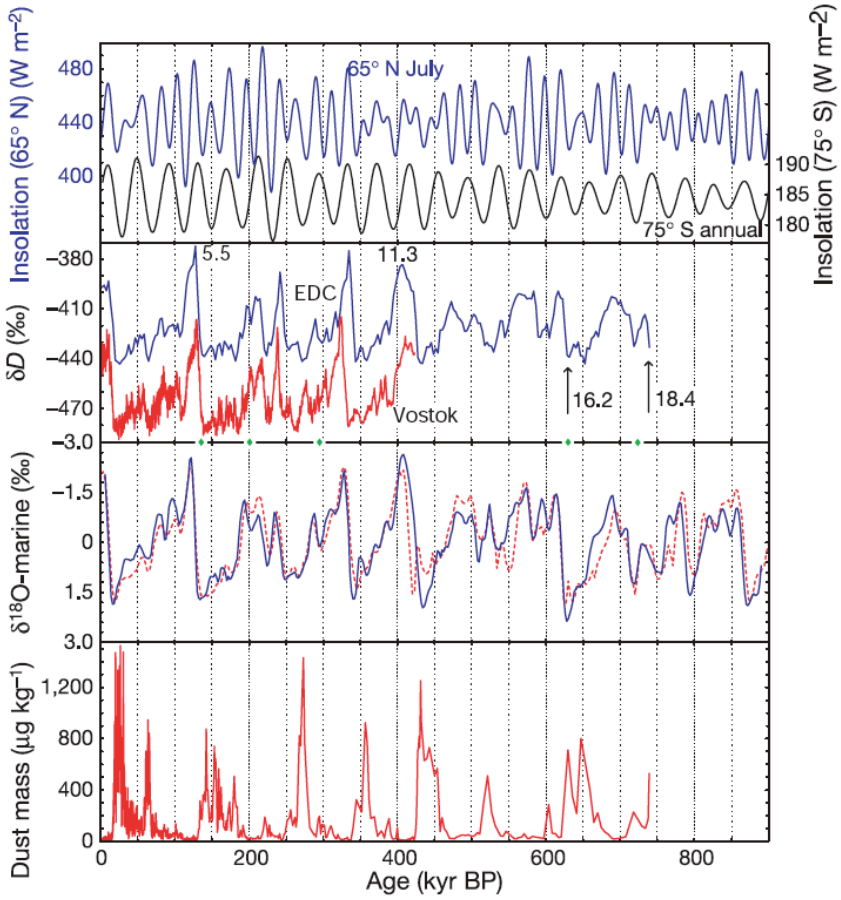

Figure 1.8: Comparison of EPICA dome C data with other paleoclimatic records. Plot a shows the mid-July insolation at 65^{o}N (blue curve) and the annual mean insolation at 75^{o}S (black curve). Plot b shows the deuterium isotopic record for the Dome C (blue) and Vostok (red) ice cores. Plot c shows the δ^{18}O isotopic record from marine sediment cores. Plot d shows the dust record from dome C. Figure from the EPICA community (2004).

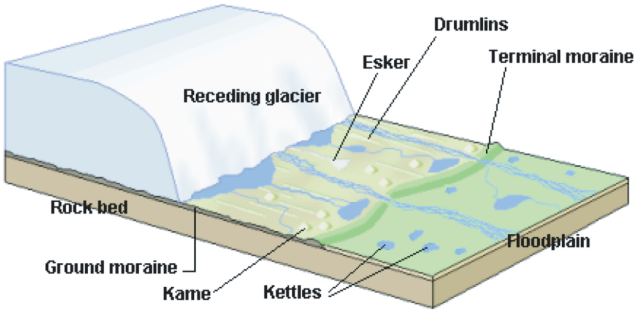

Figure 1.9: Schematic representation of the typical landscape a receding ice sheet leaves behind.

relationship between the local environment in which a sea level-indicator accumulated and a contemporary reference water level. For example, storm beach remains may have been formed two to five meters above mean sea level depending on local conditions. Moreover, since all the material is brought in from elsewhere, storm beaches are difficult to date. On the other hand, there are isolation basins. A retreating ice sheet leaves many lakes behind, for example in Finland and southern Sweden. Many of these lakes once were connected to the sea and became isolated due to the post glacial uplift of the land. The sediments of these lakes often show clear series of sediments from marine towards lacustrine deposits. In some complicated areas there are series of sediments resulting from the alternation of transgressions and regressions of the sea. These sediments are formed in situ and when undisturbed can be dated quite accurately and have an indicative meaning between mean high water spring tide and mean high water.

Figure 1.10 shows examples of relative sea level curves from a number of locations around the world. The errorbars in the figures are deduced from measurement errors, the indicative meaning of the data and dating uncertainties. There are not many data before the Last Glacial Maximum, since growing ice sheets tend to destroy geomorphological evidence formed during earlier stages. In Figure 1.10 we observe that the sea level records are very diverse with large spatial and temporal differences. The total change in sea level ranges from a few tens of meters to over 200 meters. There is a clear distinction between near field and far field data. The near field (close to the ice sheet) is the region influenced by isostatic adjustment. Data from these regions are influenced directly by the post glacial uplift and are therefore primarily indicators of the geometry of the ice load and of the earth properties (e.g. Tushingham and Peltier, 1991; Fjeldskaar, 1997; Velichko et al., 1997; Vermeersen and Sabadini, 1999; Di Donato et al., 2000; Kaufmann et al., 2000; Kaufmann and Wu, 2002; Mangerud, 2004; Svendsen et al., 2004; Lambeck et al., 2006). The far field is the region outside the influence of isostatic adjustment. Data from the far field are often used as indicators for global ice volume (e.g. Milne et al., 2002; Peltier,

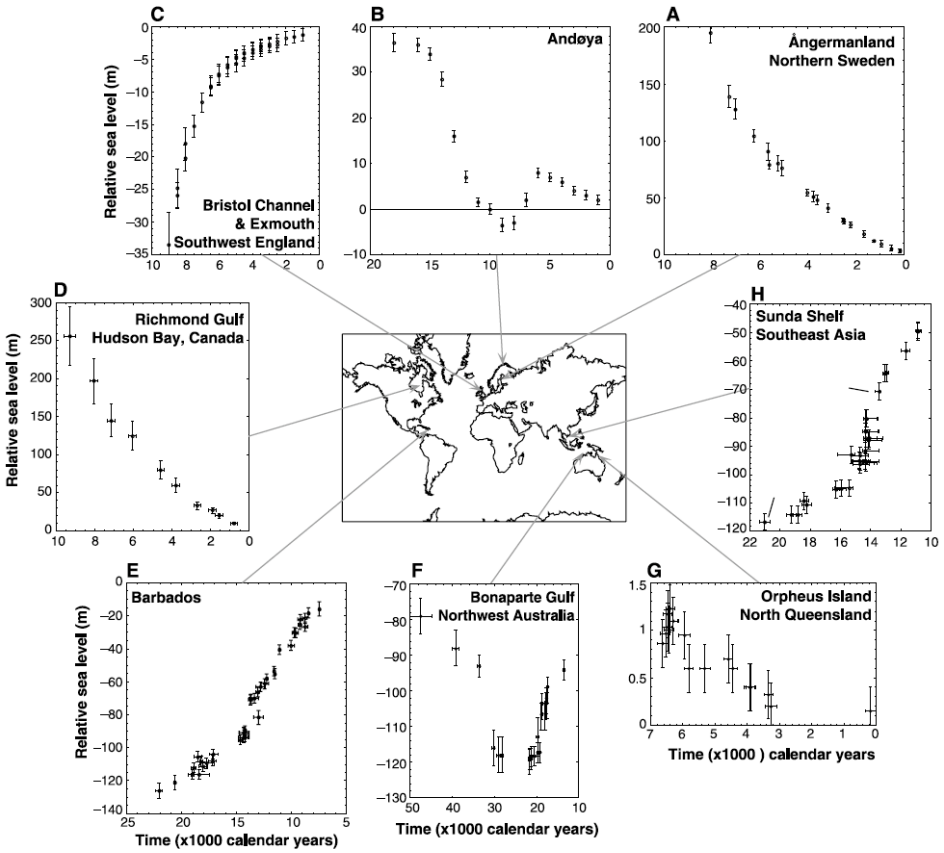

Figure 1.10: Examples of relative sea level curves. Figure from Lambeck and Chappell (2001).

2002).

Figure 1.10, plot A from Ångermanland, northern Sweden, shows an example of a near field relative sea level curve. The data from this curve are mainly based on isolation basins. No data are available before 10,000 BP, because before that time, the ice sheet had not yet retreated. The data show a relative sea level fall in spite of the melting of the ice sheet. The rebound in this region is the dominant process in relative sea level change. The relative sea level fall started fast and decreased over time, indicating that initially the uplift rate was fast compared to the present day uplift. The uplift rate decreased gradually over time, because the ice melt ceased over time.

Barbados, Figure 1.10, plot E, is a typical example of a far field record. The data from this location are mainly based on the dating of coral reefs. Coral reefs only grow close to the sea surface where sunlight can penetrate. When relative sea level rises, the coral

reefs grow with the rising surface as long as the rate of sea level rise is not too large. The age of coral reefs at a specific depth is therefore an indicator of the sea level at that time. Barbados lies in an equatorial region far away from the ice sheets and the influence of rebound. Therefore it is sensitive to changes in the ocean volume, hence to the changing volume of the ice sheets. Barbados shows almost continuous relative sea level rise of about 130 meters between 20,000 BP and 8,000 BP indicating a dramatic decrease of the ice sheets during that period. Barbados has a well-known relatively constant tectonic signal which can be corrected for. Moreover, it is situated in a location where each ice sheet's characteristic signal of sea level change predicts the eustatic signal. Therefore, the Barbados record is generally believed to represent the global eustatic sea level change (e.g. Bassett et al., 2005; Peltier and Fairbanks, 2007).

1.2.2 Ice sheet reconstructions

To reconstruct the ice sheets as a function of time, often optimization methods are used. Relative sea level curves and/or other geomorphological indicators are inverted for optimum ice distribution using simple relations for the shape of ice sheets and the sea level equation (Chapter 2) (e.g. Tushingham and Peltier, 1991; Peltier, 1994; Milne et al., 2002; Peltier, 2004; Lambeck et al., 2006). The resulting ice reconstructions have been used extensively to study the earth structure (e.g. Vermeersen and Sabadini, 1999; Di Donato et al., 2000; Kaufmann et al., 2000; Kaufmann and Wu, 2002; Tarasov and Peltier, 2002; Zhong et al., 2003; Kaufmann et al., 2005; Spada et al., 2006).

Data give us much information on the ice sheets of the past, but they cannot fully constrain the ice. Most geomorphological data give information on ice extent or flow direction, but not on ice thickness. Moreover, geomorphological data are only available for regions currently not covered by ice and in accessible regions. Data older than the LGM are very limited, so virtually no data on the growth of ice sheets exist. The relative sea level data are not spread homogeneously across the earth surface, but are mainly located in areas near the present day coast. As a result, the ice thickness in the centers of the continents remain essentially unconstrained. Also, the results are very much dependent on the assumed earth model (Kaufmann et al., 2000).

Besides from being inconclusive, these ice sheet reconstructions do not provide understanding of the physical processes governing the response of ice sheets to climate changes. For that we need dynamical ice sheet models.

1.3 Dynamical ice sheet models

Dynamical ice sheet models use ice physics, climate conditions, and the earth structure to model the ice extent and thickness as a function of time and location. This has the advantage that the different processes steering the response of ice sheets can be disentangled in the form of sensitivity experiments (e.g. Oerlemans, 1980; Ghil and Le Treut, 1981; Le Meur and Huybrechts, 1996; Van de Wal and Ekholm, 1996; Van de Wal, 1999; Charbit et al., 2002). This allows us to investigate why ice sheets respond to changes in

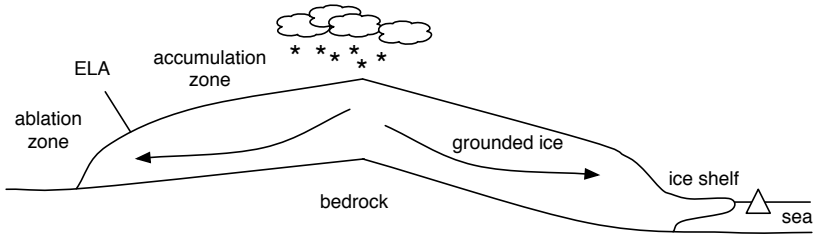

Figure 1.11: Schematic representation of the physical components governing an ice sheet.

environmental conditions in a specific way even when the data are insufficient to fully constrain the ice (e.g. Mahaffy, 1976; Hutter, 1983; Oerlemans and van der Veen, 1984; Huybrechts, 1992; Letréguilly and Ritz, 1993; Huybrechts et al., 1996; Van der Veen, 1999; Payne et al., 2000; Siegert et al., 2001; Bintanja et al., 2002; Huybrechts, 2002; Forsström and Greve, 2004; Zweck and Huybrechts, 2005).

Figure 1.11 shows a schematic representation of an ice sheet with the elementary physical components. In general ice forms in regions with positive surface mass balance; the accumulation area. The annual mass balance is the net result of snow fall and melt over a year. When the annual amount of snow fall exceeds the annual amount of melt, the mass balance is positive and an ice sheet will form. The ice flows under the influence of gravity to lower regions where the mass balance is negative, hence where the annual melt exceeds the annual snow fall. This is called the ablation area. The two regions are separated by the equilibrium line (ELA), where the mass balance is zero, hence annual melt equals annual snow fall. Instead of flowing to an ablation area, the ice may also flow directly into the ocean, where it calves and produces icebergs. In embayments with relatively quiet, shallow water an ice shelf may form, which is floating ice of several hundreds meters thickness attached to the grounded ice, which feeds the ice shelf. This ice shelf is not to be confused with sea ice. Sea ice forms in situ by freezing sea water and never exceeds a thickness of about 10 meters.

The most important theory for three-dimensional ice flow models is explained in Chapter 2. Most ice sheet models are externally forced in three ways; (i) the bedrock subsidence, (ii) the mass balance as the net effect of climate conditions, and (iii) the sea level which influences the ice shelf formation and calving. For the sea level generally a eustatic curve is prescribed based on geological studies. As discussed before, this is not equal to the actual sea level, but to calculate the actual, relative sea level is a large computational burden.

To predict the response of ice sheets to climate changes, an accurate treatment of the mass balance is essential. Observations of past climate conditions are sparse. A few ice cores provide valuable information, as shown in Figure 1.8, but this information is often difficult to interpret in terms of temperature and precipitation. Moreover, an ice core is a point measurement and results are difficult to extrapolate over vast regions. Another

difficult issue is the extrapolation of present day melt rates as a function of temperature into the glacial periods (e.g. Pollard, 1980; Reeh, 1991; Braithwaite, 1995). Nevertheless, various modelling approaches (e.g. Sanberg and Oerlemans, 1983; Hulton and Sugden, 1995; Paul, 1996; Fabre et al., 1997; Huybrechts et al., 2004) have provided insight in the behaviour of ice sheets in changing climate conditions.

1.3.1 Isostatic adjustment

Besides the mass balance and sea level, the ice sheet geometry is also influenced by the earth response. As the local precipitation and melt depend on surface elevation it is clear that including the vertical deformation due to isostatic adjustment is important. This effect influences surface temperature, basal topography, and the stress field in the ice sheet. In addition, the isostatic adjustment of the earth causes higher relative sea level stands which influences the amount of calving and grounding line mechanics.

The Earth consists of three main shells. The outermost part is a thin, brittle, rigid shell called the lithosphere, which has a thickness on the order of 100 kilometers. The next layer extending to approximately 2900 kilometers depth is the mantle, divided in an upper mantle and a lower mantle with the division at a phase transition at 670 kilometers depth. Below 2900 kilometers depth is the core. Whereas rock seems very much undeformable, in reality it continuously deforms under an applied force. Almost all solids, including most rocks, behave elastically when the forces are not too great or of too long duration. Elastic behaviour is similar to a spring; when a load is attached to a spring, the spring will deform instantaneously. When the load is removed, the spring will return to its original state. However, the rocks in the mantle are very hot, and under high pressure. As a result, in addition to the elastic response there is a viscous response. This is similar to a dashpot; attach a load to a dashpot and it will deform slowly towards a final state. In general a typical earth model consists of a combination of springs and/or dashpots. A common combination is a spring and a dashpot in series, which is the visoelastic approach; when a load is placed on the surface, there is an instantaneous elastic response, followed by a slower, viscous response, Figure 1.12 (e.g. Peltier, 1974; Wu and Peltier, 1982; Le Meur, 1996; Le Meur and Huybrechts, 1998; Di Donato et al., 2000; Vermeersen and Sabadini, 1999; Le Meur, 2001; Watts, 2001; Kaufmann et al., 2000; Kaufmann and Wu, 2002; Tarasov and Peltier, 2002; Kaufmann et al., 2005).

To understand the response of the earth to the formation of an ice sheet, we regard a zero-order elastic model or local isostasy. In this approach the earth has no lateral strength, reducing the problem to Archimedes law; the pressure at a given level is equal throughout the earth. When a load is applied the crust will sink down until the mass of displaced mantle material is equal to the added mass of ice. Since the density of ice is approximately one third of the density of the mantle, an ice sheet will cause subsidence of up to one third of its own thickness. A large Pleistocene ice sheet is typically three kilometers thick, yielding a subsidence of over one kilometer. When an ice sheet melts, the earth rebounds to its original state, resulting in an elevation increase of again over one kilometer. The rate of this process forms an indication of the viscosity or fluidity of the mantle.

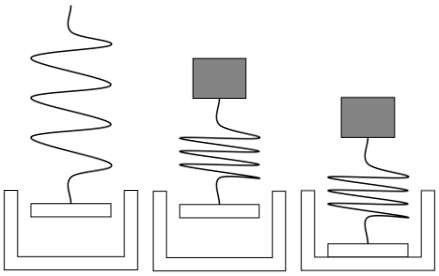

Figure 1.12: Schematic representation of a viscoelastic earth model as a series of a spring and a dashpot.

The most commonly used ways to model isostatic adjustment are discussed in more detail in Chapter 2.

1.4 This thesis

In this thesis we will examine the physical and numerical behaviour of an ice sheet model. We emphasize the dynamical interactions of the ice sheets with the different forcings as mass balance and isostatic adjustment. Modelled ice sheets are very sensitive to the description of the mass balance because of the nonlinear feedback of the mass balance with height. Both melt and precipitation depend on temperature, which is a strong function of altitude, hence of the geometry of an ice sheet. Accurate mass balance parameterizations take this feedback into account by adjusting the mass balance to changes in the ice sheet geometry. As a consequence, small modelling inaccuracies in the ice sheet geometry and earth response accumulate over time, which obscures the response of ice sheets to actual climate changes. Therefore, it is important to keep these inaccuracies to a minimum.

We focus on understanding of the physical processes involved. We use a conceptual modelling approach. This means in practice that we show less interest in whether the geometry of the modelled ice sheets coincides with observations. We try to avoid ad-hoc tuning of the model. Instead we focus on how the different physical processes influence the geometry. We will show several sensitivity tests where we change elements in the forcings and examine the resulting response of the modelled ice sheets.

Chapter 2 will provide a theoretical framework, discussing the most elementary theory with respect to the interactions between ice sheets and the solid earth, as used in this thesis. Chapter 3 will discuss some aspects of the numerical behaviour of the ice sheet model itself. Then, we turn our attention to the forcing mechanisms. Chapter 4 discusses the effects of lateral variations in lithospheric strength and the use of sea level curves in order to resolve these lateral variations. Chapter 5 will then discuss a suitable mass balance model for an application to the Eurasian Ice sheet, which includes the essential climatological processes governing ice sheets with changing geometries. Finally, Chapter

6 shows in more detail the dynamical response of ice sheets to isostatic adjustment. We also compare several earth models using the mass balance model as discussed in Chapter 5.

Chapter 2

Basic theory

In this chapter we discuss some basic theory regarding sea level, ice sheets, and isostatic adjustment. The goal is to provide a concise theoretical framework for the main results in this thesis. More details can be found in key textbooks (e.g. Cathles, 1975; Hutter, 1983; Wu, 1998; Van der Veen, 1999; Watts, 2001; Turcotte and Schubert, 2002) and the references as provided in the sections.

2.1 The sea level equation

In the Introduction we qualitatively discussed the response of the sea level to changes in ice sheets. We showed that changes in sea level are an important source of information regarding changes in ice sheets, and hence, climate changes. To elaborate on the importance of sea level a bit further, we will derive the standard sea level equation as formulated by Farrell and Clark (1976). This sea level equation described the changes in relative sea level as a results of changes in ice sheets.

Since sea level coincides with an equipotential in the earth's gravity field, sea level change due to an ice sheet can be calculated using the theory of gravity. The gravitational potential at distance r from the earth's center is given by

$$\phi(r) = \frac{GM_e}{r}, \qquad \mathrm{r} \geq \mathrm{R}, \tag{2.1}$$

where G is the gravitational constant, R is the earth's radius, and M_e is the total mass of the earth.

Now assume the earth is covered by a thin uniform oceanic shell, Figure 2.1. If a mass M_i is extracted from the ocean and placed on the surface in the form of an ice sheet, the gravitational potential at point r consists of two contributions; one from the earth, where M_e is now reduced with M_i, and one from the ice sheet with mass M_i. This results in

$$\phi^*(r,\theta) = \frac{G(M_e - M_i)}{r} + \frac{G\,M_i}{x}, \tag{2.2}$$

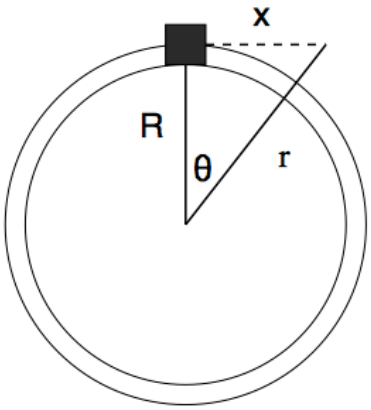

Figure 2.1: Cross-section of the earth with a thin, uniform ocean, from which a mass Mi is extracted to form a weight on the surface. R is the radius of the earth and θ the angular distance from the ice sheet.

where x is the distance between point r and the ice sheet, given by

$$x = \sqrt{r^2 + R^2 - 2Rr\cos(\theta)}, \tag{2.3}$$

where θ is the angular distance from the ice sheet. The earth's surface, $r = R$, is not an equipotential anymore, since

$$\phi^*(R, \theta) = \frac{G(M_e - M_i)}{R} + \frac{G\,M_i}{2R\sin(\theta/2)}. \tag{2.4}$$

In addition, as sea level coincides with an equipotential surface, $r = R$ can no longer be the sea level. Instead, the sea surface is at a small distance $r = R + \epsilon(\theta)$. In other words,

$$\phi^*(R + \epsilon, \theta) = \phi(R). \tag{2.5}$$

This new potential can be written as a Taylor expansion.

$$\phi^*(R + \epsilon, \theta) \approx \phi^*(R, \theta) + \epsilon\frac{\partial\phi^*(R, \theta)}{\partial r}. \tag{2.6}$$

Using that $\partial\phi/\partial r \approx \partial\phi^*/\partial r = -g$, it is possible to solve for ϵ. Together with $g/G = M_e/R$ this results in

$$\epsilon(\theta) = \frac{M_i\,R}{M_e}\left(\frac{1}{2\sin(\theta/2)} - 1\right). \tag{2.7}$$

This is the expression for an equipotential which might be the new sealevel. However, any surface $\epsilon + c$ is also an equipotential and therefore a possible sealevel. The actual sealevel

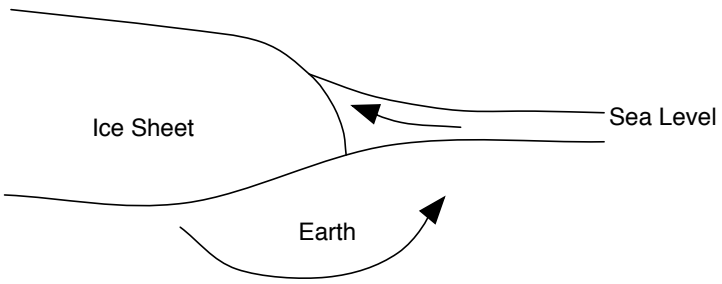

Figure 2.2: Schematic representation of the response of the sea level to the formation of an ice sheet.

is found by imposing conservation of mass; the total mass extracted from the oceans must be equal to the mass contained in the ice sheets, so

$$\int_0^{2\pi}\int_0^{\pi}\int_R^{R+\epsilon+c} \mathrm{d}V = -M_i/\rho_w, \tag{2.8}$$

where ρ_w is the density of water and $\mathrm{d}V = r^2\sin(\theta)\mathrm{d}r\,\mathrm{d}\theta\,\mathrm{d}\phi$. Since both ϵ and c are very much smaller than R, this can be solved to first order. Together with $M_e = 4/3\pi R^3\rho_e$, where ρ_e is the mean density of the total earth, this yields

$$\epsilon^* = \epsilon + c \;\; = \;\; \frac{M_i\,R}{M_e}\left(\frac{1}{2\sin(\theta/2)} - 1 - \frac{\rho_e}{3\rho_w}\right). \tag{2.9}$$

This is the actual sea level change, i.e. the difference between the radial distance to the final surface and the radial distance to the initial sea surface. If masses are positioned on the earth's surface, the center of mass shifts a little from the center and equation (2.9) is actually only valid for that particular coordinate system. However, the deviation is very small. The third term on the right hand side of equation (2.9) actually represents the eustatic sea level change, hence the sea level change if there had not been gravitational attraction of the ice.

The effect of the gravitation can be quite large (e.g. Farrell and Clark, 1976). The relative sea level can actually rise due to formation of an ice sheet close to the margins, as illustrated in Figure 2.2. The ocean volume changes in response to the formation or melting of ice sheets. This volume change must be distributed such that the ocean surface remains an equipotential. However, this is just one of the two effects changing the sea level on earth. When the surface loading on the earth of either ice or water changes, the earth responds to this change by redistributing the material in its interior. This redistribution of mass causes a change in gravitational potential as well and must be taken into account.

It is possible to solve the entire system if we construct a Green function ϕ^G which describes the total potential perturbation due to the addition of a point mass on the earth's

surface and the earth's response to this point mass. By convolving this Green function with the spatial distribution of changed mass on earth, both changes in the ice distribution (I) and sea level change (S), we find the change in potential on the earth's surface, $r = R$, to be

$$\phi_1(\theta, \lambda) = \rho_i \phi^G *_i I(\theta, \lambda) + \rho_w \phi^G *_o S(\theta, \lambda), \tag{2.10}$$

where θ and λ are coordinates on the earth's surface describing angular distance from the ice, $*_{i,o}$ describe convolutions over the ice or ocean area, and

$$M_i = \int\int_{ice} \rho_i I(\theta', \lambda') \, \mathrm{d}\Omega, \tag{2.11}$$

$$M_o = \int\int_{oceans} \rho_w S(\theta', \lambda') \, \mathrm{d}\Omega, \tag{2.12}$$

where M_i and M_o are the mass changes of the ice and oceans respectively, and ρ_i and ρ_w are the densities of ice and water. The integrals describe integrations over the ice and ocean area.

The change in sea level $S(\theta, \lambda)$ is then given by

$$S(\theta, \lambda) = \frac{\phi_1(\theta, \lambda)}{g} + c, \tag{2.13}$$

where the constant c again follows from the conservation of mass $M_o - M_i = 0$, which states that the change in ice mass is opposite to the change in ocean mass. This constant c shifts the entire equipotential with the eustatic sea level change added with the average change in potential over the oceans.

Note that the change in sea level S is a function of itself.

$$S(\theta, \lambda) = \frac{\rho_i}{g} \phi^G *_i I(\theta, \lambda) + \frac{\rho_w}{g} \phi^G *_o S(\theta, \lambda) + c, \tag{2.14}$$

The first term in this equation describes the change in potential from all the ice loads, the second term describes the change in sea level from the redistribution of the sea water. This equation describes the change in sea level in a spherical geometry for any earth model and any load, where the earth model determines the expression for the Greens function ϕ^G.

2.2 Earth models

To calculate the sea level change as a result of changing ice masses we need to formulate the isostatic response of the solid earth to these changing ice masses.

2.2.1 Airy or local isostasy

The simplest way to represent the earth response to an ice loading is called Airy or local isostasy. Local or Airy isostasy assumes that the pressure at a given depth in any column

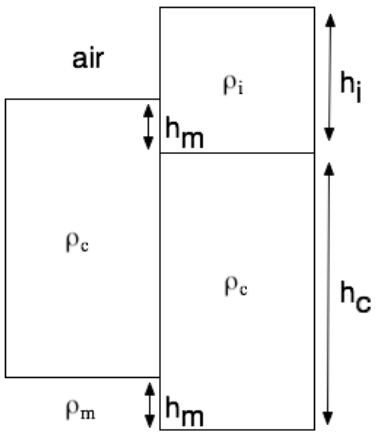

Figure 2.3: Geometry of the ice and crust for calculating h_m using local isostasy

of earth is the same. Hence, if a column is loaded with ice, this column will sink until the weight of the ice is balanced by an equivalent drop in height of the surface (e.g. Turcotte and Schubert, 2002).

Using the geometry as shown in Figure 2.3, the subsidence of the crust because of a pack of ice on top of the crust is given by

$$h_m = \frac{\rho_i}{\rho_m} h_i \tag{2.15}$$

where h_i represents the ice-thickness, and $\rho_{i,m}$ the density of ice and mantle respectively.

Despite the simplified approach to earth rheology, this model has been used extensively in glaciological applications. In this thesis we prefer to use a more realistic approach as explained in the next sections.

2.2.2 Flexure

A more realistic approach to earth modelling is by assuming the earth responds to surface loading similar to an elastic plate (e.g. Zienkiewicz and Taylor, 2000). Figure 2.4 shows a one-dimensional infinite plate subjected to a pressure load. We assume that the bending is cylindrical and that sections which are originally normal to the middle plane remain plane during deformation, thus only experience rigid translations and rotations. The total displacement can then be described as $\mathbf{u} = (u, v, w)$ or (u_1, u_2, u_3) with

$$u(x, y, z) = u_0(x, y) - z\theta_x(x, y), \tag{2.16}$$
$$v(x, y, z) = v_0(x, y) - z\theta_y(x, y), \tag{2.17}$$
$$w(x, y) = w_0(x, y), \tag{2.18}$$

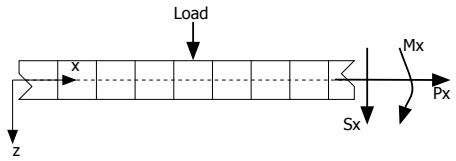

Figure 2.4: Geometry of a one-dimensional bending plate with directions of deformation and stress resultants.

where u_0, v_0 and w_0 are rigid translations and $\theta_{x,y}$ are rotations of the normals to the middle plane. We finally assume that the thickness of the plate is small compared to the horizontal dimensions of the load. As a result, the vertical shear forces are small (Zienkiewicz and Taylor, 2000). We want to solve for $\mathbf{u}$. This implies solving for five parameters u_0, v_0, w_0, θ_x and θ_y.

When regarding a plate, instead of the infinitesimal stress balance, the stress resultants determine the deformational behaviour. Figure 2.4 shows the stress resultants M_x (bending moment), S_x (shear stress) and P_x (normal stress). These stress resultants can be calculated using

$$M_x = -\int_{-h/2}^{h/2} z\,\sigma_{xx}\,\mathrm{d}z, \tag{2.19}$$

$$S_x = \int_{-h/2}^{h/2} \sigma_{xz}\,\mathrm{d}z, \tag{2.20}$$

$$P_x = \int_{-h/2}^{h/2} \sigma_{xx}\,\mathrm{d}z. \tag{2.21}$$

where the integration is over the entire thickness of the plate h. The bending moment M_x can be regarded as a leverage, the other resultants are total stresses.

In two dimensions, in addition to M_x, S_x and P_x, we also have M_y, S_y, P_y, P_{xy} and a twisting moment M_{xy}. These are defined similar to M_x, S_x and P_x.

We can solve for the displacement $\mathbf{u}$, equations (2.16) to (2.18), by writing down the stress equilibrium equations. These equations can be formulated by integration of a local stress balance over the plate thickness (e.g. Zienkiewicz and Taylor, 2000):

$$\int_{-h/2}^{h/2} \left[\frac{\partial \sigma_{xx}}{\partial x} + \frac{\partial \sigma_{xy}}{\partial y} + \frac{\partial \sigma_{xz}}{\partial z}\right] \mathrm{d}z = \frac{\partial P_x}{\partial x} + \frac{\partial P_{xy}}{\partial y} = 0, \tag{2.22}$$

$$\int_{-h/2}^{h/2} \left[\frac{\partial \sigma_{yx}}{\partial x} + \frac{\partial \sigma_{yy}}{\partial y} + \frac{\partial \sigma_{yz}}{\partial z}\right] \mathrm{d}z = \frac{\partial P_{xy}}{\partial x} + \frac{\partial P_y}{\partial y} = 0, \tag{2.23}$$

$$\int_{-h/2}^{h/2} \left[\frac{\partial \sigma_{xz}}{\partial x} + \frac{\partial \sigma_{yz}}{\partial y} + \frac{\partial \sigma_{zz}}{\partial z}\right] \mathrm{d}z = \frac{\partial S_x}{\partial x} + \frac{\partial S_y}{\partial y} + q = 0. \tag{2.24}$$

where q is the resultant from the normal traction on the top and bottom surfaces, hence the loading. Notice that in q not only the load, but also the buoyancy at the bottom of the plate is incorporated as $q = q_{load} - q_{buoy}$, where $q_{buoy} = \rho_m g w$, where ρ_m is the density of the mantle.

Since three equations are insufficient to solve for the five parameters in equations (2.16) to (2.18), we have to use the bending moments:

$$\int_{-h/2}^{h/2} z \left[\frac{\partial \sigma_{xx}}{\partial x} + \frac{\partial \sigma_{xy}}{\partial y} + \frac{\partial \sigma_{xz}}{\partial z} \right] \mathrm{d}z = \frac{\partial M_x}{\partial x} + \frac{\partial M_{xy}}{\partial y} + S_x = 0, \tag{2.25}$$

$$\int_{-h/2}^{h/2} z \left[\frac{\partial \sigma_{yx}}{\partial x} + \frac{\partial \sigma_{yy}}{\partial y} + \frac{\partial \sigma_{yz}}{\partial z} \right] \mathrm{d}z = \frac{\partial M_y}{\partial y} + \frac{\partial M_{xy}}{\partial x} + S_y = 0, \tag{2.26}$$

The equations containing P describe the horizontal displacement u_0 and v_0 and decouple from the rest of the equations describing w_0, θ_x and θ_y.

We assume all deformation is elastic, which results in the following expression for the stress tensor

$$\boldsymbol{\sigma} = \frac{E}{1+\nu} \begin{pmatrix} \frac{1}{1-\nu}\left(\epsilon_{xx} + \nu \epsilon_{yy}\right) & \epsilon_{xy} & \epsilon_{xz} \\ \epsilon_{xy} & \frac{1}{1-\nu}\left(\nu \epsilon_{xx} + \epsilon_{yy}\right) & \epsilon_{yz} \\ \epsilon_{xz} & \epsilon_{yz} & 0 \end{pmatrix}, \tag{2.27}$$

where E and ν are Young's modulus and Poisson's ratio. The deformation tensor ϵ_{ij} is defined as

$$\epsilon_{ij} = \frac{1}{2}\left(\frac{\partial u_i}{\partial x_j} + \frac{\partial u_j}{\partial x_i} \right). \tag{2.28}$$

If we now write the stress resultants in terms of u, v and w and use equations (2.24) to (2.26), we find $\theta \approx \nabla w$, and

$$(\mathbf{L}\nabla)^T \mathbf{D}' \mathbf{L} \nabla w - q = 0, \tag{2.29}$$

where $(\mathbf{L}\nabla)$ is given by

$$(\mathbf{L}\nabla) = \begin{bmatrix} \frac{\partial^2}{\partial x^2} & \frac{\partial^2}{\partial y^2} & 2\frac{\partial^2}{\partial x \partial y} \end{bmatrix}^T. \tag{2.30}$$

The matrix $\mathbf{D}'$ is given by

$$\mathbf{D}' = D \begin{bmatrix} 1 & \nu & 0 \\ \nu & 1 & 0 \\ 0 & 0 & (1-\nu)/2 \end{bmatrix}, \tag{2.31}$$

where D is called the flexural rigidity and given by

$$D = \frac{E h^3}{12(1-\nu^2)}. \tag{2.32}$$

If we now assume the flexural rigidity or bending stiffness D' to be constant throughout the medium, we find the equation widely used for the calculation of flexure in geophysics

$$D\left(\frac{\partial^4 w}{\partial x^4} + 2\frac{\partial^4 w}{\partial x^2 \partial y^2} + \frac{\partial^4 w}{\partial y^4}\right) - q = 0. \tag{2.33}$$

This equation can be solved analytically (e.g. Brotchie and Silvester, 1969; Le Meur and Huybrechts, 1996; Van der Veen, 1999; Turcotte and Schubert, 2002).

For situations where D is not constant however, the equation is given by (Van Wees and Cloetingh, 1994)

$$\frac{\partial^2}{\partial x^2}\left(D\frac{\partial w}{\partial x^2}\right) + \nu\frac{\partial^2}{\partial y^2}\left(D\frac{\partial^2 w}{\partial x^2}\right) + \nu\frac{\partial^2}{\partial x^2}\left(D\frac{\partial^2 w}{\partial y^2}\right) + \frac{\partial^2}{\partial y^2}\left(D\frac{\partial^2 w}{\partial y^2}\right) + 2(1-\nu)\frac{\partial^2}{\partial x \partial y}\left(D\frac{\partial^2 w}{\partial x \partial y}\right) - q = 0 \tag{2.34}$$

The flexural approach is used throughout this thesis. We use equation (2.34) in Chapter 4 where we model lateral variations in lithospheric strength. Chapters 5 and 6 use the simplified equation (2.33).

2.3 Time dependent behaviour

2.3.1 Exponential relaxation

Equations (2.15) and (2.34) describe an instantaneous response. The earth however cannot respond instantaneously, since the mantle below the lithosphere has a nonzero viscosity. Therefore, the temporal response has a time delay and is calculated as (e.g. Van der Veen, 1999):

$$\frac{\partial b}{\partial t} = -\frac{1}{\tau}\left(b + w - b_0\right). \tag{2.35}$$

This is a simple first order approach in which we characterize the response of the mantle with one single relaxation time τ. The parameter w is the total displacement as calculated by the lithospheric model, b is the height of the bedrock, and b_0 is the initial topography, hence topography without ice.

Equation (2.35) can be combined with either equation (2.15) or (2.34) to form a complete earth model, which can be used to estimate the isostatic response of the earth to ice loading. This type of earth model is commonly used in glaciology for its computational efficiency. This approach is used throughout this thesis.

2.3.2 Self-gravitating viscoelastic earth models (SGVE)

A physically more comprehensive treatment of the physical properties of the mantle can be made by describing the mantle and lithosphere as a viscoelastic medium. This means

that the mantle has an initial elastic response followed by a slower viscous response. Models of this type generally consist of a series of concentric spherical shells. The models are self-gravitating, which means that the changes in the gravitational potential interact with the density structure of the model (e.g. Wu and Peltier, 1982). Similarly to the flexural equation we start with a stress balance, but instead of a thin plate, we now regard an infinitesimal volume with density ρ:

$$\nabla \cdot \boldsymbol{\sigma} + \rho \mathbf{F} = 0, \tag{2.36}$$

where $\boldsymbol{\sigma}$ is the stress tensor and $\mathbf{F}$ the body forces. For the rest of this derivation the earth is assumed to be hydrostatically pre-stressed. This means the surface is assumed to be in hydrostatic equilibrium and the stresses are corrected for this effect. Furthermore, the rheology is assumed to be linear and viscoelastic, and the earth's rotation is neglected. Then, the radial pressure gradient is given by

$$\frac{dp_o}{dr} = -\rho_0(r) g_0(r), \tag{2.37}$$

where ρ_0 and g_0 are the density and gravitational acceleration of the unperturbed earth. If the block is now moved elastically by an amount $\mathbf{u}$, the pressure will change as

$$p = p_0 - \mathbf{u} \cdot \nabla p_0. \tag{2.38}$$

Thus, the only change in pressure comes from the advection of pre-stress (Cathles, 1975). These equations are combined with the hydrostatical condition

$$\sigma^h_{ij} = -p\delta_{ij}, \tag{2.39}$$

where $\boldsymbol{\sigma^h}$ is the hydrostatical pre-stress related to the total stress by $\boldsymbol{\sigma} = \boldsymbol{\sigma^h} + \boldsymbol{\sigma^{nh}}$, where $\boldsymbol{\sigma^{nh}}$ is the non-hydrostatically applied stress. The following linearized balance of forces in the deformed situation is then obtained:

$$-\nabla p_o + \nabla \cdot \boldsymbol{\sigma}^{nh} - \nabla(\rho_0 g_0 \mathbf{u} \cdot \hat{\mathbf{e}}_\mathbf{r}) + \rho \mathbf{F} = 0, \tag{2.40}$$

where $\hat{\mathbf{e}}_\mathbf{r}$ is a unit vector in radial direction. If the deformation was purely viscous, the equation would have been the same except for the term arising from the advection of pre-stress $\nabla(\rho_0 g_0 \mathbf{u} \cdot \hat{\mathbf{e}}_\mathbf{r})$. This term accounts for the initial elastic response of the earth (Cathles, 1975).

The force $\mathbf{F}$ can be split in different types of forcings, like tidal and centrifugal forces, but here $\mathbf{F}$ will just represent the gravity and can be written as the negative gradient of a potential field ϕ,

$$\mathbf{F} = -\nabla\phi. \tag{2.41}$$

In the perturbed state ϕ can be written as $\phi = \phi_0 + \phi_1$, where ϕ_1 is the perturbation and ϕ_0 the unperturbed potential. In the same way the density ρ can be written as $\rho = \rho_0 + \rho_1$

where again ρ_1 is the perturbation and ρ_0 the unperturbed density. Combining this leads to the linearized equation of momentum of the perturbed system

$$\nabla \cdot \boldsymbol{\sigma}^{\boldsymbol{nh}} - \nabla(\rho_0 g_0 \mathbf{u} \cdot \hat{\mathbf{e}}_\mathbf{r}) - \rho_0 \nabla \phi_1 - \rho_1 g_0 \hat{\mathbf{e}}_\mathbf{r} = 0. \tag{2.42}$$

In this equation, the first term on the left hand side describes the contribution from the non-hydrostatical or perturbation stress, the second term describes the advection of hydrostatic pre-stress the third term represents the changed gravity field and the fourth term describes the changed density. This latter term is zero in the case of incompressibility. The third term is zero when the effect of self-gravitation is neglected (the effect that masses in and on the earth attract each other).

Together with the Poisson equation

$$\nabla^2 \phi_1 = -4\pi G \rho_1, \tag{2.43}$$

where G is the gravitational constant and the constitutional equation

$$\dot{\sigma}_{ij} + \frac{\mu}{\eta}\left(\sigma_{ij} - \frac{1}{3}\sigma_{kk}\delta_{ij}\right) = 2\mu\dot{\epsilon}_{ij} + \lambda\dot{\epsilon}_{kk}\delta_{ij}, \tag{2.44}$$

where λ and μ are the Lamé parameters, η the viscosity and ϵ_{ij} the strain tensor, equation (2.42) forms a closed system that can be solved.

For a spherically symmetric layered earth model, the response of the model to an impulse load can be calculated analytically (e.g. Peltier, 1974). The response of the SGVE model to the growth and decay of ice sheets is then calculated by convolving the loading history with this impulse response of the system. The impulse response for the vertical displacement at the surface (w) is commonly expressed as a series of Legendre polynomials

$$w(R, \gamma, t) = \frac{\phi_{2,l}(R)}{g} \sum_{l=0}^{\infty} h_l^L(t)\, P_l\left(\cos(\gamma)\right), \tag{2.45}$$

where R is the radius of the earth, γ is the great circle angle between the implus load and the observation point, t is the time after loading, $\phi_{2,l}(R)$ is the degree l component in the Legendre expansion of the perturbation of the gravity field, g is the gravitational acceleration, and P_l are Legendre polynomials. The coefficients $h_l^L(t)$ are the Love numbers for the radial displacement, and can be written as

$$h_l^L = h_l^E \delta(t) + \sum_{k=1}^{K} r_k^l \exp(-s_k^l\, t), \tag{2.46}$$

where $\delta(t)$ is the Dirac delta function. The temporal response consists of an instantaneous elastic h_l^E component and a series of exponential functions. These exponential functions are characterized by the amplitude r_k^l, and an inverse decay time s_k^l. These parameters are defined by the density, and the elastic and viscous structure of the earth model as is the number of relaxation modes K. Compared to the flexural model, which used only one relaxation time, this SGVE model uses a relaxation spectrum.

This self-gravitating viscoelastic earth model is used in Chapter 6 of this thesis as a physically more realistic alternative to the flexural approach.

2.4 Ice flow models

The ice model is based on the vertically integrated continuity equation (e.g. Huybrechts, 1992; Van der Veen, 1999; Oerlemans, 2001):

$$\frac{\partial H}{\partial t} = -\nabla \cdot (H\,\mathbf{U}) + B, \tag{2.47}$$

where H is the ice thickness, B is the mass balance, and $\mathbf{U}$ is the vertical mean velocity

$$\mathbf{U} = \frac{1}{H}\int_b^{H+b} \mathbf{v}\,\mathrm{d}z, \tag{2.48}$$

where $\mathbf{v} = (v_x, v_y)$ is the velocity vector.

The velocity $\mathbf{v}$ is connected to the strain rate tensor $\dot{\epsilon}_{ij}$ as (Van der Veen, 1999)

$$\dot{\epsilon}_{ij} = \frac{1}{2}\left\{\frac{\partial v_i}{\partial x_j} + \frac{\partial v_j}{\partial x_i}\right\}. \tag{2.49}$$

Strains and strain rates can be measured directly. In practice however this is generally an impossible task, so we need an additional equation to relate the strain rate to a force balance.

The strain rate is coupled to the deviatoric stress tensor τ_{ij} through Glen's flow law, which is an experimentally determined law, hence not exact;

$$\dot{\epsilon}_{ij} = A\tau_e^{n-1}\tau_{ij}, \tag{2.50}$$

where τ_e is the effective stress defined as

$$2\tau_e^2 = \tau_{xx}^2 + \tau_{yy}^2 + \tau_{zz}^2 + 2\left(\tau_{xy}^2 + \tau_{xz}^2 + \tau_{yz}^2\right). \tag{2.51}$$

A and n are the flow parameters. From laboratory experiments the "best" n for ice deformation is probably around 3. A is very much temperature dependent and defined as

$$A = m\,A_0\,\exp\left(-\frac{Q}{RT_i}\right), \tag{2.52}$$

where Q is the activation energy, R is the gas constant, T_i is the ice temperature, and m is an enhancement factor (Huybrechts, 1992). throughout this thesis we neglect this temperature dependence and adopt a constant representative value for A of 6x10^{-17}Pa^{-3}yr^{-1}.

In general the force balance is given by (Huybrechts, 1992; Van der Veen, 1999)

$$\frac{\partial \sigma_{xx}}{\partial x} + \frac{\partial \sigma_{xy}}{\partial y} + \frac{\partial \sigma_{xz}}{\partial z} = 0, \tag{2.53}$$

$$\frac{\partial \sigma_{yx}}{\partial x} + \frac{\partial \sigma_{yy}}{\partial y} + \frac{\partial \sigma_{yz}}{\partial z} = 0, \tag{2.54}$$

$$\frac{\partial \sigma_{zx}}{\partial x} + \frac{\partial \sigma_{zy}}{\partial y} + \frac{\partial \sigma_{zz}}{\partial z} = \rho_i g. \tag{2.55}$$

Here, ρ_i is the ice density, taken constant, σ is the stress tensor, and g is the gravitational acceleration. If we now assume that the deviatoric vertical normal stress is equal to the weight of the ice above ($\tau_{zz} = -\rho g(H+b-z)$), and we incorporate the incompressibility criterion ($\tau_{xx} + \tau_{yy} + \tau_{zz} = 0$), we can rewrite this force balance in terms of deviatoric stresses as

$$\frac{\partial \tau_{xz}}{\partial z} = \rho_i g \frac{\partial (H+b-z)}{\partial x} - 2\frac{\partial \tau_{xx}}{\partial x} - \frac{\partial \tau_{yy}}{\partial x} - \frac{\partial \tau_{xy}}{\partial y}, \tag{2.56}$$

$$\frac{\partial \tau_{yz}}{\partial z} = \rho_i g \frac{\partial (H+b-z)}{\partial y} - 2\frac{\partial \tau_{yy}}{\partial y} - \frac{\partial \tau_{xx}}{\partial y} - \frac{\partial \tau_{xy}}{\partial x}. \tag{2.57}$$

We now further assume that variations in the normal or longitudinal stresses are negligible compared to the variations in shear stresses. This is called the shallow ice approximation and is equivalent to assuming that the normal stress tensor is isotropic and hydrostatic equilibrium prevails (e.g. Hutter, 1983; Huybrechts, 1992). We can then express the shear stress in terms of variations in the ice surface, by integrating the previous equations from the surface to a height z in the ice:

$$\tau_{xz}(z) = -\rho_i g\,(H+b-z)\,\frac{\partial (H+b)}{\partial x}, \tag{2.58}$$

$$\tau_{yz}(z) = -\rho_i g\,(H+b-z)\,\frac{\partial (H+b)}{\partial y}. \tag{2.59}$$

Now we can combine these equations with the flow law and integrating with respect to z, assuming that the vertical variations in horizontal velocities are small. This results in the following expression for the horizontal velocity vector $\mathbf{v}$ (Huybrechts, 1992; Van der Veen, 1999):

$$\mathbf{v}(z) = \mathbf{v}(b) - 2(\rho_i g)^3 \left[\nabla (H+b) \cdot \nabla (H+b)\right] \nabla (H+b) \int_b^z A\,(H+b-z')^3 \,\mathrm{d}z', \tag{2.60}$$

where $\mathbf{v}(b)$ is the basal sliding velocity U_s. The total vertical mean velocity is given by

$$\mathbf{U} = \mathbf{U_s} + \mathbf{U_d}, \tag{2.61}$$

where $\mathbf{U_d}$ is the deformation velocity and $\mathbf{U_s}$ the sliding velocity. The vertical mean deformation velocity is given by

$$\mathbf{U_d} = -\frac{2}{5}(\rho\, g)^3 A \left[\left(\frac{\partial h}{\partial x}\right)^2 + \left(\frac{\partial h}{\partial y}\right)^2\right] \nabla h\, H^4, \tag{2.62}$$

with ρ the ice density and g the gravitational acceleration.

The sliding velocity is a difficult quantity, since it requires knowledge on basal properties as stress, hydraulic pressure, temperature and bed roughness. We adopt a Weertman

type sliding velocity, which is commonly used in glaciological applications and is written as

$$\mathbf{U_s} = f_s \left[\left(\frac{\partial h}{\partial x} \right)^2 + \left(\frac{\partial h}{\partial y} \right)^2 \right] \nabla h \, H^2, \tag{2.63}$$

with f_s a sliding parameter which incorporates bed roughness and material properties. Since sliding requires a water film present at the base, it normally takes place when the temperature of the ice is above the pressure-melting point. However, since we neglected thermodynamics, we can only allow sliding in areas where the mass balance is negative.

Equation (2.47) can be rewritten as

$$\frac{\partial H}{\partial t} = -\nabla \cdot \mathbf{F} + B, \tag{2.64}$$

where $\mathbf{F}$ is the horizontal ice flux. It is defined as

$$\mathbf{F} = -D \nabla h, \tag{2.65}$$

where h is the ice surface height and D is the diffusion. For a two-dimensional model, the diffusion D is then given as

$$D(x, y) = \frac{2}{5} (\rho \, g)^3 A \left[\left(\frac{\partial h}{\partial x} \right)^2 + \left(\frac{\partial h}{\partial y} \right)^2 \right] H^5. \tag{2.66}$$

For a diffusion type equation there exist many stable solution schemes, hence the preference of writing the equations in this form.

Chapter 3

Effects of spatial discretisation in ice sheet modelling using the shallow ice approximation (SIA)

This paper assesses a two-dimensional, vertically integrated ice model for its numerical properties in the calculation of ice sheet evolution on a sloping bed using the shallow ice approximation. We discuss the influence of initial conditions and individual model parameters on the model's numerical behaviour, with the emphasis on varying spatial discretisations. The modelling results suffer badly from numerical problems. They show a strong dependence on grid cell size and we conclude that the widely used grid cell spacing of 20 kilometers is too coarse. The numerical errors are small in each single time step, but increase nonlinearly over time and with volume change, as a result of feedback of the mass balance with height. We propose a new method for the calculation of the surface gradient near the margin, which improves the results significantly. Furthermore, we show that we may use dimension analysis as a tool to explain in which situations numerical problems are to be expected.

3.1 Introduction

Since the 1970s, the knowledge of the dynamical behaviour of ice sheets and their interaction with climate has greatly expanded through the development of ice flow models, which simulate the evolution of ice under changing climatic conditions. All ice sheet models are based on the principle of mass conservation; the ice flows under its own weight (e.g. Oerlemans and van der Veen, 1984; Paterson, 1994). However, a hierarchy of these

This chapter has been published as: J. van den Berg, R.S.W. van de Wal and J. Oerlemans (2006). Effects of spatial discretisation in ice sheet modelling using the shallow ice approximation (SIA), *Journal of Glaciology*, **52**, 89-98.

models has evolved with models differing in many aspects, like applied rheology, treatment of the boundaries, coupling to the atmosphere, and numerical details, such as the use of finite element or finite difference schemes. More fundamental differences come from how many elements of the full system of equations are actually solved. Besides solving the complete system, an approach called the shallow ice approximation (SIA) is widely used (Hutter, 1983). This approximation is based on the assumption that large ice bodies are mainly deformed by basal shear stress, and therefore neglects longitudinal stresses. Whereas solving the full system of equations obviously results in more realistic results (especially near the margin and ice divide), the SIA simulates the essential processes of ice flow quite well (Leysinger Vieli and Gudmundsson, 2004). The most important advantage of models based on the SIA is their computational speed. It is not yet possible to calculate the evolution of large ice sheets throughout complete ice age cycles with the full system of equations, which is one of the reasons why the SIA is still widely used today (e.g. Mahaffy, 1976; Oerlemans, 1981a,b; Fastook and Chapman, 1989; Huybrechts, 1990; Calov and Hutter, 1996; Greve, 1997; Pollard and Thompson, 1997; Pfeffer et al., 1998; Huybrechts and de Wolde, 1999; Van de Wal, 1999; Van de Wal et al., 2001; Bintanja et al., 2002; Näslund et al., 2003; Plummer and Philips, 2003). We are interested in the modelling of large ice sheets throughout ice ages. Therefore, we limit ourselves in this paper to a model using the shallow ice approximation.

An attempt to compare and assess many different (SIA) ice models on continental scales was made as part of the European Ice Sheet Modelling INiTiative (EISMINT, funded by the European Science Foundation). Several models were evaluated for their physical properties and accuracy by using tests with simplified geometries (Huybrechts et al., 1996; Payne et al., 2000). These tests, however, did not focus on the numerical properties of the models. Greve and Calov (2002) investigated numerical behaviour. They focussed on the use of different numerical schemes, whereas the present paper addresses the behaviour of a single numerical scheme as a function of varying spatial discretisation. Greve and Calov (2002) only used two different grid point spacings. Even more importantly, neither EISMINT nor Greve and Calov (2002) combined any experiments for numerical properties with mass balance parameterisations, which included the nonlinear feedback with height. Instead, mass balance was parameterised as a function of distance only. This is an essential modelling element (Oerlemans and van der Veen, 1984) as numerical errors can grow nonlinearly over time due to this feedback mechanism. The mass balance feedback with height is especially important for research which deals with ice sheet inception, where the integration periods of model runs are very large and the climatic conditions remain relatively uncertain.

In this study we have assessed a two-dimensional, vertically integrated, finite-difference (SIA) ice model specifically for dependency of modelling results on varying grid point spacings (1-20 km) in cases where the mass balance was a function of altitude. When we say varying grid point spacings, we mean variations between model runs, not variations within one grid. All our experiments used spatially uniform grids. We stress that we did not attempt to assess the modelling errors from solving the SIA instead of the full system of equations. We focussed on the numerical errors arising from inaccuracies in the numerical treatment of the SIA. As Bueler et al. (in press) discuss, these two approaches are

fundamentally different. Although we focussed on the effects of varying spatial discretisations, this did not include the resolving power of small-scale structures. We investigated the ability of each discretisation to solve for the global behaviour of a large, smooth ice sheet as well as the influence of initial conditions and the sensitivity of the model results to the individual model parameters. Details of the ice model are discussed in Sections 3.2 and 3.3. Section 3.4 is divided in two parts; the first part is concerned with the effects of initial conditions on the resulting numerically calculated ice sheets. The second part deals with the sensitivity of the modelling results to values of individual model parameters, such as bedrock slope and the maximum value for the mass balance. The results are discussed in Section 3.5, after which conclusions are drawn in Section 3.6.

3.2 Theory

The ice model is based on the vertically integrated continuity equation (e.g. Huybrechts, 1992; Van der Veen, 1999; Oerlemans, 2001):

$$\frac{\partial H}{\partial t} = -\nabla \cdot (H\,\mathbf{U}) + B, \tag{3.1}$$

where H is the ice thickness, $\mathbf{U}$ is the vertical mean horizontal velocity, and B is the mass balance. Equation (3.1) can be rewritten as

$$\frac{\partial H}{\partial t} = -\nabla \cdot \mathbf{F} + B, \tag{3.2}$$

where $\mathbf{F}$ is the horizontal ice flux. It is defined as

$$\mathbf{F} = -D\nabla h, \tag{3.3}$$

where h is the ice surface height and D is the diffusion. We used the shallow ice approximation (e.g., Hutter, 1983; Huybrechts, 1992; Van der Veen, 1999), which assumes that the horizontal scale of the ice extent is much larger than the vertical scale. For a two-dimensional model, the diffusion D is then given as

$$D(x,y) = 2(\rho\, g)^n A \left[\left(\frac{\partial h}{\partial x} \right)^2 + \left(\frac{\partial h}{\partial y} \right)^2 \right]^{(n-1)/2} \frac{1}{n+2} H^{n+2}, \tag{3.4}$$

with ρ the ice density, g the gravitational acceleration, and A and n the flow parameters. The value for n is set to 3. The parameter A is known to be temperature-dependent, but we set A to a constant value, for simplicity. The vertical mean horizontal velocity is given by

$$\mathbf{U} = \mathbf{U_s} + \mathbf{U_d}, \tag{3.5}$$

where $\mathbf{U_d}$ is the vertical mean horizontal deformation velocity (denoted hereafter as deformation velocity) and $\mathbf{U_s}$ the sliding velocity. We tried several parameterisations for

the sliding velocity, but as long as the sliding velocity was smaller than the deformation velocity, the numerical properties of the model did not change. Therefore, we set $\mathbf{U_s}$ to zero everywhere. For the two-dimensional model, the expression for the vertical mean horizontal velocity then reduces to the deformation velocity, which is given by (e.g. Oerlemans and van der Veen, 1984; Huybrechts, 1992).

$$\mathbf{U} = -2(\rho\, g)^n A \left[\left(\frac{\partial h}{\partial x} \right)^2 + \left(\frac{\partial h}{\partial y} \right)^2 \right]^{(n-1)/2} \nabla h \, \frac{1}{n+2} H^{n+1}. \tag{3.6}$$

We also used a one-dimensional model, which is based on the two-dimensional model and is equivalent to a two-dimensional plane strain approximation. It is discussed in detail by Oerlemans (2001). The final expression for the vertical mean horizontal velocity is parameterised as

$$U = f_d H S_d^n. \tag{3.7}$$

The flow parameter f_d ($1.1 \cdot 10^{-24}$ Pa^{-3}s^{-1}) represents the situation on a large sheet ice sheet like Greenland (Van de Wal, 1999). The driving stress S_d is caused by the gravitational force of the ice. In the one-dimensional model, the diffusion D is given by

$$D(x) = (\rho\, g)^n \left(\frac{\partial h}{\partial x} \right)^{n-1} f_d H^{n+2}. \tag{3.8}$$

We prescribed the mass balance as a linear profile for which the only variable is height above a reference level

$$B = min\left(B_{max}, \beta\,(h - E)\right), \tag{3.9}$$

where β is the mass balance gradient in a^{-1} and E the equilibrium line altitude in m. The mass balance is zero at E and increases with elevation until a positive upper limit B_{max} (in m a^{-1} ice equivalent). Above that elevation, the mass balance remains constant with height.

3.3 Numerical methods

3.3.1 Discretisations

The one-dimensional model is solved on a staggered grid (Figure 3.1). At each time step, between each two grid points (marked by circles in Figure 3.1), F is calculated either as

$$F_{i+1/2}^t \approx -D_{i+1/2}^t \left(\frac{h_{i+1}^t - h_i^t}{\Delta x} \right), \tag{3.10}$$

or as

$$F_{i+1/2}^t \approx -\left(\frac{D_{i+1}^t + D_i^t}{2} \right) \left(\frac{h_{i+1}^t - h_i^t}{\Delta x} \right). \tag{3.11}$$

Equations (3.10) and (3.11) correspond to respectively type I and II ice models of the EISMINT experiments (Huybrechts et al., 1996), which are widely used by ice sheet modellers. The difference between the two types is whether the diffusion D is calculated at the staggered grid points (I) (marked by the circles in Figure 3.1) or the regular (II) grid points with central differencing on the regular grid points (marked by crosses in Figure 3.1). For type I the diffusion is calculated as

$$D^t_{i+1/2} \approx (\rho g)^3 \left(\frac{h^t_{i+1} - h^t_i}{\Delta x} \right)^2 f_d \left(\frac{H^t_i + H^t_{i+1}}{2} \right)^5 . \tag{3.12}$$

For type II the diffusion is given by

$$D^t_i \approx (\rho g)^3 \left(\frac{h^t_{i+1} - h^t_{i-1}}{2\Delta x} \right)^2 f_d {H^t_i}^5 . \tag{3.13}$$

Type I models are numerically more precise, but require much smaller time steps than type II models (Huybrechts et al., 1996; Hindmarsh and Payne, 1996).

Finally, the time integration is calculated with forward differencing as

$$H^{t+1}_i \approx H^t_i + \frac{\Delta t}{\Delta x} \left(F^t_{i-1/2} - F^t_{i+1/2} + B^t_i \Delta x \right) \tag{3.14}$$

The numerical approach in the two-dimensional model is similar to the one used in the one-dimensional model. All spatial derivatives are calculated with central differencing on a staggered grid (Figure 3.2). However, the time integration is calculated differently, since explicit integration requires very small time steps which results in a long computation time. Instead, an Alternating Direction Implicit method is used as described by several authors (Mahaffy, 1976; Huybrechts, 1992). In this method, each time step is divided into two steps. In the first step, the time integration for all the x-direction components of the equations is performed implicitly, whereas the y-direction components remain explicit. In the second step, this is reversed. All calculations were performed in double precision.

3.3.2 Boundary conditions

At the left side of the domain, we impose a boundary condition that corresponds to an ice divide, i.e., the surface gradient is zero:

$$\frac{\partial h}{\partial x}|_{x=0} \approx \frac{h_1 - h_0}{\Delta x} \quad = \quad 0. \tag{3.15}$$

At the right-hand side, we impose that the ice thickness H is equal to zero. In the two-dimensional model, the ice thickness at all domain boundaries is set to zero.

At each timestep the new ice thickness is calculated from the old ice thickness and the mass balance throughout the grid, where all grid points are treated the same, whether the ice thickness is positive, zero or negative. Then, all negative ice thicknesses are set to zero. The initial ice thickness, i.e. the ice thickness distribution at timestep $t = 0$, is free as long as the grid boundary conditions are fulfilled.

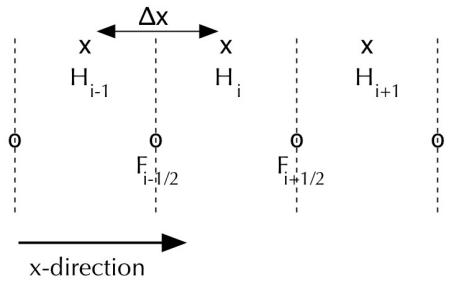

Figure 3.1: Staggered grid in one dimension.

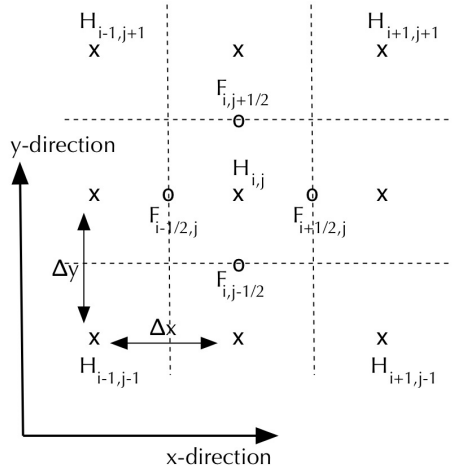

Figure 3.2: Staggered grid in two dimensions.

3.3.3 Weertman analytical solution

The models were tested in one dimension for an analytical solution based on the Weertman (1961) solution, which is the steady state solution of the equations from the shallow ice approximation for a mass balance as a function of distance along the surface. We prescribed the mass balance as a constant positive quantity a until a specific distance R, and a constant negative quantity $-a'$ for distances larger than R. The mass balance was not a function of altitude and did not change in time.

For this case both type I and II models performed well in one as well as in two dimensions, reaching the analytical solution for all the discretisations used throughout this paper to within five percent. The stability of the two-dimensional type I model was very poor. Hindmarsh and Payne (1996) already noted that this type of models generate lead to results with slow, long oscillations. Our experiments confirmed this behaviour, but also showed that this behaviour is time-dependent. The effect increased for larger time steps and decreased, and even disappeared, for smaller time steps. Type I models in general need smaller time steps than type II models. In this paper the calculations were over long integration times for very fine discretisations, hence we required very small time steps even for type II models. This implied, however, that the experiments with the two-dimensional model described in the next sections were not computationally feasible for the type I model. Results from coarser spatial discretisations, however, confirmed the Weertman analytical solution. The one-dimensional model also required very small time steps, but this was still computationally feasible.

3.4 Results

We performed experiments with both the one- and two-dimensional (type I and II) models. In each experiment, the ice margin evolved freely as a function of ice flux and mass balance. We calculated steady-state solutions by integrating over a period of 250,000 years for parameter sets listed in Table 3.1. For the two-dimensional model, a grid cell size of 2 by 2 km was the finest grid feasible. The ice sheet was too flat for the surface gradients to be calculated within the limits posed by the use of double precision for smaller grid cell sizes. The one-dimensional model did not show this problem.

We did not include any bedrock response, but prescribed the bedrock profile as

$$b(r) = b_{max} - \lambda\, r \tag{3.16}$$

with b the bedrock height in m, b_{max} the maximum bedrock height, which we kept at 400 m for all experiments. The bedrock slope is given by λ, and r is the distance from the centre in km, which in one dimension is given by x and in two dimensions by $\sqrt{x^2 + y^2}$. The combination of a sloping bedrock and an altitude dependent mass balance parameterisation is similar to an ice sheet developing on a flat bed with a sloping equilibrium line. According to Weertman (1961) this kind of situation has at least one stable solution, as long as the slope is finite and non-zero. This means that under changing climate conditions the ice sheet is able to approach a new equilibrium.

	λ (m km^{-1})	β (10^{-3} a^{-1})	B$_{max}$ (m a^{-1})	E (m)	initial condition
exp. 1	1.3	5	0.1	250	no ice
exp. 2	1.3	5	0.1	250	steady state exp.1, ref, Δx 1 km
exp. 3	1.3	5	0.1	250	steady state E_0 = 150 m, ref., Δx = 1 km
exp. 4	1.1-2	5	0.1	250	no ice
exp. 5	1.3	1-10	0.1	250	no ice
exp. 6	1.3	5	0.1-1.4	250	no ice

Table 3.1: Parameter values for the experiments, with λ the bedrock slope, β the mass balance gradient, B$_{max}$ the cut-off value of the mass balance, E the equilibrium line altitude, and initial condition of the ice sheet at the start of the experiment. The ice sheets used as initial conditions in experiments 2 and 3 are calculated with the original solution. The starting condition for experiment 2 is the result of experiment 1 for Δx=1 km. For experiment 3, instead of the result from experiment 1, the steady-state ice sheet for E=150 m was used.

3.4.1 Initial conditions

Experiment 1: Growth to steady state

As a start, we evaluated ice growth towards a steady state with the parameters listed in Table 3.1 (experiment 1). We started the time integration without ice and at time t=0, we set the equilibrium line altitude E to 250 m and let the ice sheet evolve to steady state. Figure 3.3 shows the results. We scaled all calculated ice volumes with the volumes from the type II model associated with a grid cell size Δx of 2 by 2 km in the two-dimensional case, such that the volume curve for Δx=2 km was always equal to 1. In the one-dimensional case, all curves were scaled with the areas from the type II model associated to a grid cell size of 1 km.

The dashed lines in the upper panels of Figure 3.3 show the ice volumes as a function of time for both the two-dimensional (a) and the one-dimensional (b) type II model for several discretisations. (The solid lines will be discussed later.) In the one-dimensional case, the curves were calculated as the integral over all ice thicknesses, and represent the area of a cross-section in an infinite plane. The dashed lines are based on the standard type II model as described in Sections 3.2 and 3.3.

The dash-dotted lines in Figure 3.3b show the ice area for the one-dimensional type I model. We do not show the corresponding ice volumes for the two-dimensional type I model, since (see Section 3.3.1) the required time steps were so small that the calculation time was not feasible anymore. Tests at coarser grids confirmed that the numerical behaviour in two dimensions was similar to the behaviour in one dimension. The type I models generally perform better than the type II models.

The lower panel (c) of Figure 3.3 shows the steady-state solutions for the different discretisations for the one-dimensional type II model. The results in Figure 3.3 are striking: the results from the individual discretisations differ by tens of percents. This is observed in both the one-dimensional and the two-dimensional model, calculated with different numerical methods.

Since both models gave similar results, and since the one-dimensional model required less computation time, all other experiments were performed with the one-dimensional model only. Even though type I models generally performed better than type II models, the fundamental behaviour was the same. For this reason, we performed the sensitivity tests in this paper only for type II models.

Experiment 2: Maintaining steady state

In this experiment (Table 3.1, experiment 2), we studied the dependence on the initial conditions by starting the test with the steady-state ice sheet for Δx=1 km from experiment 1, instead of starting without ice. We kept the equilibrium line E at 250 m and continued the calculations for the different discretisations for the one-dimensional model. Figure 3.4 shows the results. In principle, the ice sheet should not change. As coarse grids introduce larger inaccuracies in the calculation of the surface gradient than fine grids, the modelled ice sheets adjust to slightly lower volumes for the different discretisations. The jumps in the curves are caused by the retreating ice margin. Each jump corresponds to the ice margin retreating over a distance of one grid point.

Experiment 3: Retreat to steady state

In this experiment, we studied the retreat of a steady-state ice sheet towards a smaller steady-state ice sheet corresponding to a warmer climate. In this third experiment, the initial conditions were given by the steady-state ice sheet for E=150 m, calculated with Δx=1 km (Table 3.1, experiment 3). At time t=0, the value of E was shifted to 250 m. Figure 3.5 depicts the results. The jumps in the curves represent the moving ice margin. For the finest grids, the curves are practically smooth. The effects as shown in Figure 3.5 are remarkably smaller in this retreat scenario than in the growth scenario and are of the same order of magnitude as the minor adjustments shown in Figure 3.4. This suggests that, for coarse grids, results are strongly dependent on initial conditions.

To further examine this we calculated steady state ice sheets for a wide range of initial conditions from no ice to very large ice sheets. Figure 3.6 summarizes the results; it shows the resulting area as a function of equilibrium line altitude E for Δx=1 km (Figure 3.6a) and for Δx=20 km (Figure 3.6b). We only show stable solutions. With stable we mean that when the steady states are locally perturbed while keeping the equilibrium line altitude constant, the model returns to the steady state solution belonging to that equilibrium line altitude. Figure 3.6a shows three different regimes. The first is the regime for equilibrium line altitudes smaller than 400 meters. In this regime there is only one stable solution possible for each equilibrium line altitude. The second regime is the regime for equilibrium line altitudes higher than 800 meters. In this regime there is also only one

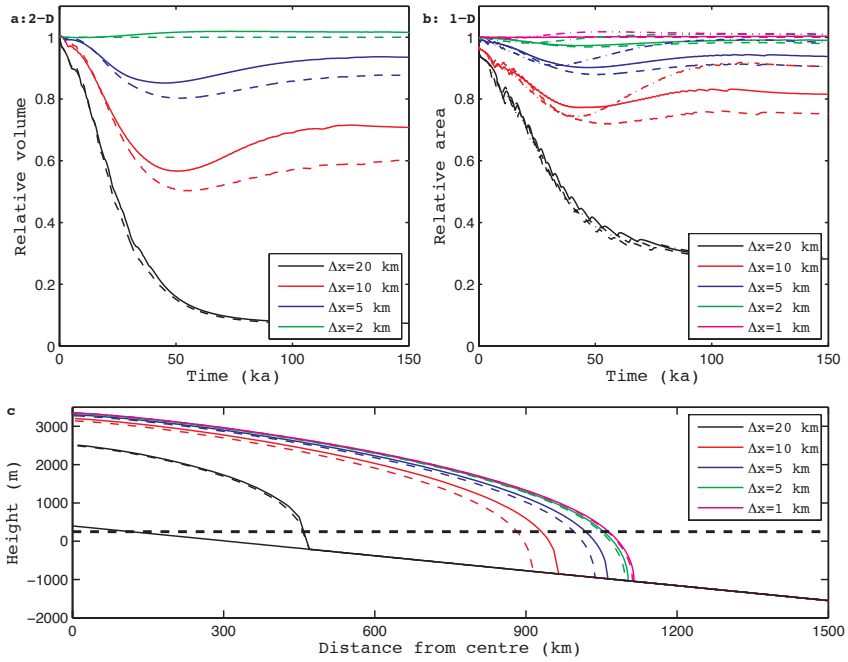

Figure 3.3: Top: Ice volume/area as a function of time for the parameter values listed in Table 3.1, experiment 1, for several grid point distances Δx for (a) the two-dimensional type II model (volumes) and (b) the one-dimensional type I and II models (areas). The dashed lines represent the reference type II solutions, the solid lines the type II solutions calculated with a modified surface gradient, and the dash-dotted lines represent solutions calculated with a type I model. All volume curves are scaled such that the reference type II solution with Δx=1 km is equal to 1 for the one-dimensional case and the type II reference solution for Δx=2 km is equal to 1 for the two-dimensional case. The lower panel (c) shows steady-state profiles for the same discretisations with height in metres on the y-axis and distance from the centre in km, calculated with the one-dimensional type II model. The thick, black, dashed line is the equilibrium line altitude, in this case constant at 250 m.

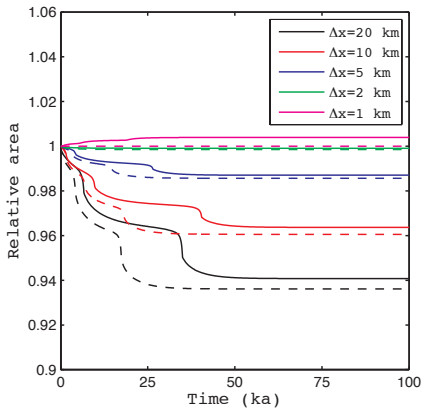

Figure 3.4: Relative ice area as a function of time for several discretisations for experiment 2 (See Table 3.1). All curves are scaled relative to the reference solution calculated with Δx=1 km. The solid lines represent the solutions calculated with a modified surface gradient, and the dashed lines represent the type II reference solutions.

stable solution possible, namely no ice. In between these two regime is a third regime where for each equilibrium line altitude there are two stable solutions. Depending on the initial conditions the numerical integration of Equation (3.1) will result in either of the two stable steady states.

Whereas for Δx=1 km type I and II models produced the same results, this is not longer true for Δx=20 km, Figure 3.6b. The open and closed circles do not coincide. In addition, instead of clear lines with stable solutions, as shown in Figure 3.6a, there are now regions of possible steady state solutions. Depending on initial conditions the numerical integration of Equation (3.1) will result in a stable steady state somewhere in the grey area. There are three different grey regions in the plot; the two lightest shades represent the regions with possible stable steady states for type I (darker of the two) or type I (lighter of the two) models. The third and darkest region represents the region where the regions for type I and II models overlie each other. This different behaviour for Δx= 1 km and Δx=20 km is the result of numerical inaccuracies.

An interesting aspect is that the maximum possible steady states (indicated by the upper row of open and closed circles) for Δx=20 km are slightly too big for type I and too small for type II, compared to the solutions for Δx=1 km. We will come back to this in the next section when we discuss the reasons for the numerical problems.

A slope correction formula

One reason for the inconsistencies between the results from the different spatial grid cell sizes is the discontinuity in the surface gradient at the ice margin, as illustrated in Figure

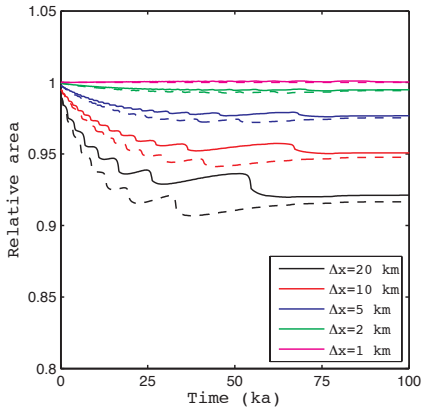

Figure 3.5: Relative area as a function of time for experiment 3, (SeeTable 3.1). All curves are scaled relative to the reference solution calculated with Δx=1 km. The solid lines represent the solutions calculated with a modified surface gradient, and the dashed lines represent the type II reference solutions.

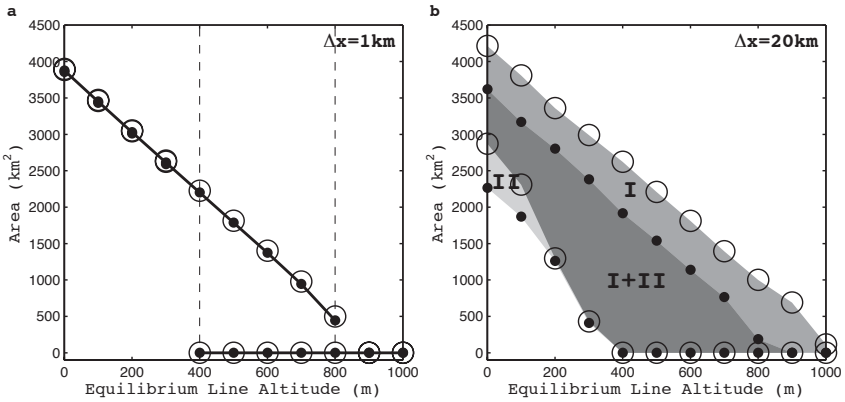

Figure 3.6: Steady state ice areas for two discretisations Δx=1 km (a) and Δx=20 km (b) both for the type I (open circles) and the type II model(closed circles) as a function of equilibrium line altitude. The solid lines in figure a show branches of possible stable steady state solutions. The grey areas in figure b show regions for possible stable steady state solutions; lightest grey is the region for the type II model, the slightly darker grey for the type I model, and the darkest is the region where the regions for both model types overlie each other.

3.7. The discretised surface gradient at the last point with ice is too small, as illustrated in Figure 3.7a by the difference between lines 1 and 2. Hence, the ice flux through the margin is underestimated. This hampers the growth of the ice sheet in the model. For one time step, this is a small effect. However, for many time steps, this error is significant since the feedback of height with mass balance is nonlinear. Since the mass balance is limited to a maximum value, the ice sheet can only compensate up to a certain degree by thickening. This suggests that this value for the maximum mass balance is an important parameter. We will examine this in the next section.

Figure 3.7b shows the numerically estimated surface gradients at the last few grid points before the ice margin, which are not influenced by the discontinuity of the surface. Assuming a smooth ice surface, the difference between these surface gradients, which is the curvature of the surface, contains information about the surface gradient at the last grid point before the ice margin. So, as an alternative to the central differencing operator, we defined a new, forward operator for the type II model by using a Taylor expansion. For the one-dimensional case, this operator is given by

$$\frac{\partial h}{\partial x}|_i \approx \frac{\partial h}{\partial x}|_{i-1} + \frac{\partial^2 h}{\partial x^2}|_{i-1}\,\Delta x. \tag{3.17}$$

In this way, we avoid having to use any points beyond the ice margin, thus avoiding the discontinuity. We cannot use this for the type I model, because in that scheme the surface gradients are calculated on the staggered grid:

$$\frac{\partial h}{\partial x}|_{i+1/2} \approx \frac{\partial h}{\partial x}|_{i-1/2} + \frac{\partial^2 h}{\partial x^2}|_{i-1/2}\,\Delta x. \tag{3.18}$$

It can be seen that in this case, the curvature term is zero. Hence, it is not possible to use the curvature information, which was the basis for the new operator. The solid lines in Figures 3.3 to 3.5 show the results for this improved surface gradient method. While this approach clearly improves the solution, it does not remove the fundamental problems. The results with this new operator are not better than the type I model, because the flux through the margin is also calculated with the diffusion of the first point outside the ice margin, which is zero. The method implicitly assumes that the diffusion goes to zero in a linear way, which is of course not the case. This problem however is not easily solved.

The bifurcation curves in Figure 3.6 show a different effect. It seems that for a retreating ice sheet two numerical effects are competing. The first is the already described effect of the underestimated slope. The other effect is also the result of grid-coarseness. When the equilibrium line altitude is moved up with 100 meters, an ice sheet evolving on a fine grid will notice that the ablation area is larger and that a part of the accumulation area receives less snow. On a coarse grid of Δx=20 km, however, the difference in surface elevation between the grid points are so large that the ablation area actually remains the same. Also, the first point in the accumulation area is already so high that it continues to receive the maximum value of the mass-balance B_{max}. Hence, the ice sheet evolving on a coarse grid will hardly feel any difference when the equilibrium line altitude is moved up with 100 meters, hence will stay larger than an ice sheet evolving on a fine grid. Since

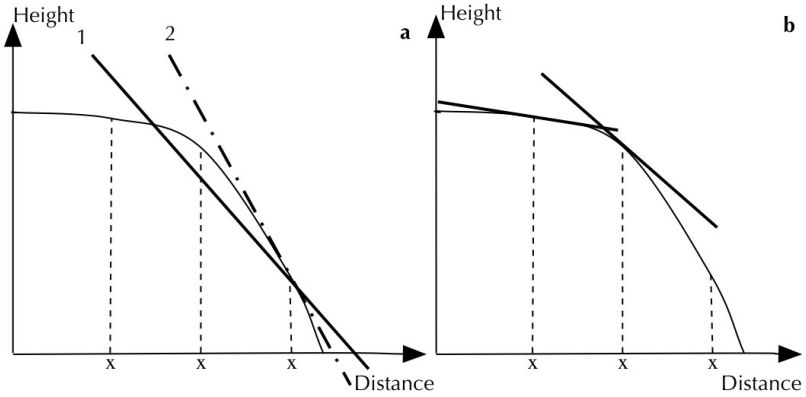

Figure 3.7: Schematic drawing of the ice margin. a: line (1) represents the numerically calculated surface gradient at the last point before the ice margin. The thick dash-dotted line (2) represents the true surface gradient. b: the lines represent the surface gradient at the last few points before the ice margin, except the last point, which is given by line 2 in figure a.

type I models suffer less from the effect of the underestimated slope, this latter effect is detectable. For type II model the latter effect is obscured by the underestimated slope effect.

3.4.2 Sensitivity of modelled ice sheets to individual parameters

This section discusses the results of sensitivity tests to individual model parameters. In each experiment, we used both the original model, which we refer to as reference model, and the improved gradient model, as defined by Equation (3.17). Again, all tests were performed for the one-dimensional type II model only. Tests with the type I model showed similar behaviour. Table 3.1 (exp. 4-6) shows the sensitivity tests that were carried out with the specific parameters. In addition we varied the equilibrium line altitude E. The results were not sensitive to the actual value of E as long as enough points covered the ice, which was only a problem at Δx=20 km. This, however, is a normal numerical effect and is not related to the effects studied in this paper. Again, all curves were scaled with the reference solution for Δx=1 km, such that the areas for Δx=1 km were always equal to 1. Each experiment started without ice. At time t=0, the parameters were set to the values presented in Table 3.1 (exp. 4-6) after which the ice sheet freely evolved to steady state.

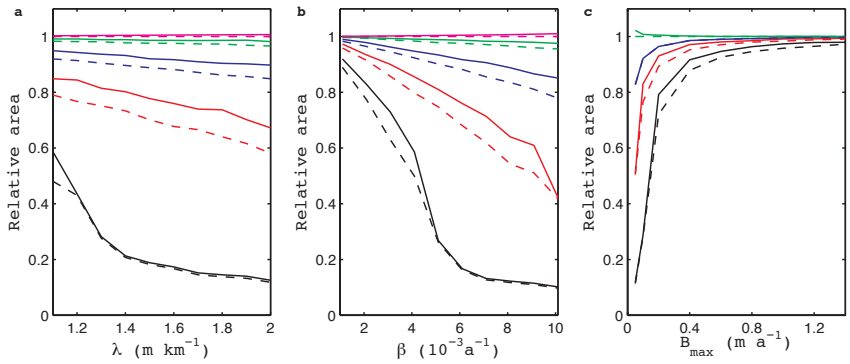

Figure 3.8: a: Steady-state areas as a function of bedrock slope λ in m km^{-1} for several discretisations (Table 3.1, experiment 4). b: Steady-state areas as a function of mass balance gradient β in 10^{-3} a^{-1} (Table 3.1, experiment 5). c: Steady-state areas as a function of maximum mass balance B_{max} in m a^{-1} (Table 3.1, experiment 6). All curves are scaled relative to the reference solution calculated with Δx=1 km. The solid lines represent the solutions calculated with a modified surface gradient, and the dashed lines represent the type II reference solutions.

Experiment 4: Bedrock slope, λ

In experiment 4, we varied λ, the slope of the underlying bedrock, as shown in Table 3.1. The changes in mass balance between individual grid points are larger for a steeper slope than for a smaller slope. Figure 3.8a demonstrates that the larger the bedrock slope, the worse the results. As in the case of the varying equilibrium line altitude, the smaller the ice sheet, the fewer grid points actually cover the ice. However, this only has an effect on the results for Δx=20 km.

For large slopes between the bedrock and the equilibrium line, the results are worse than for small slopes. However, with a slope equal to zero, the mass balance would be equal in the entire domain and no stable ice sheet would develop.

Experiment 5: Mass balance gradient, β

Here, the mass balance gradient β was varied. A large mass balance gradient increases the differences between the values of the mass balance at the individual grid points. Figure 3.8b shows that the larger the mass balance gradient β, the larger the differences between the solutions for the different grid point distances. So, the solution turns out to be sensitive for the mass balance difference between grid points.

Experiment 6: Maximum precipitation, B_{max}

The maximum precipitation B_{max} was varied. Figure 3.8c demonstrates that the problem with discretisation only occurs when the maximum precipitation is lower than approximately 1 m a^{-1} ice equivalent for this particular set of parameters, hence only in dry areas. The quantity B_{max} is strongly related to the total mass budget of an ice sheet, to which the solution is very sensitive. We will clarify this further in the discussion (Section 3.5).

3.4.3 Ice inception

Experiments 1 to 6 used a linearly sloping bedrock and the resulting solutions turned out to be sensitive to the specific slope. In practice, the bedrock slope is seldom linear. Therefore, the next and final experiment had a nonlinear bedrock slope. Figure 3.9 shows the results. We superimposed a sinusoidal perturbation on the linear bedrock of experiment 1 (see Table 3.1) but now with b_{max}=800 m instead of the previously used value of 400 m, thus creating a bedrock with smoothly varying slopes (Figure 3.9b). Furthermore, we used an equilibrium line altitude of 130 m. The first 5,000 model years, the ice lies on relatively small local slopes, resulting in minor differences between the area curves (Figure 3.9a). Once the ice reaches larger slopes, the differences between the area curves grow to the same order of magnitude as in the case of a purely linear bedrock. Finally, the ice sheets for the two finest discretisations meet and merge into a larger ice sheet. The coarser-discretisation runs suffered from severely underestimated ice volumes, as a result of which the ice did not merge. Figure 3.9b shows the steady-state solutions for all discretisations; the different discretisations resulted in completely different ice histories. Hence, the reduced-volume effect, caused by the discretisation, could have serious implications for the modelling of ice sheet inception.

3.5 Discussion

We performed a series of sensitivity experiments on the model parameters in a one-dimensional and a two-dimensional ice flow model. From these experiments it emerges that the model's numerical behaviour is very sensitive to the precise initial conditions, local geometry and climate. This may result in very unpredictable numerical behaviour and thus unreliable results for complex ice sheets. The cause of this behaviour is the sensitivity to the discretisation of the ice margin. For a fine grid, the ice flux at the ice margin is large enough to overcome the negative mass balance at the next grid point in the model. The ice sheet will grow and continue to the next grid point and so forth. However, for a coarse grid, the same ice flux may not be large enough to overcome the more negative mass balance of the next grid point much farther away, hence ice growth in the model will stop. Because of the height-mass balance feedback this seemingly small error can grow rapidly over time. The sensitivity tests in experiments 5 and 6 both affected the difference in mass-balance between points. The most important parameter however, was the maximum value for the mass balance, B_{max}. This parameter affects the ability for the

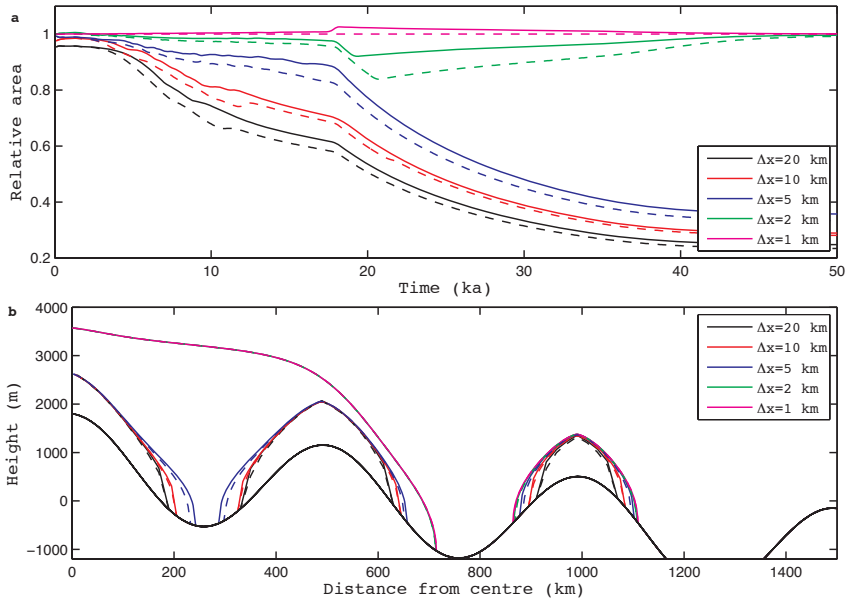

Figure 3.9: a: Area as a function of time for a sinusoidal bedrock and E=130 m for several discretisations. The dashed lines represent the reference solutions, the solid lines the solutions calculated with a modified surface gradient. All curves are scaled relative to the reference solution calculated with Δx=1 km. b: Steady-state solutions for the same discretisations with height in metres on the y-axis and distance from the centre in km.

ice sheet to thicken and compensate.

We can explain the model's numerical behaviour more fundamentally through the use of dimension analysis. Let us define new dimensionless variables according to Saltzman (2002)

$$H' = \frac{H}{L_v},\ t' = \frac{t}{L_v/a},\ U' = \frac{U}{U_c},\ x' = \frac{x}{L_h} \quad \text{and} \quad B' = \frac{B}{a}, \tag{3.19}$$

where L_v is a characteristic vertical length scale of the ice, a a characteristic velocity scale for changes in ice thickness, U_c a characteristic velocity scale for the horizontal ice motion, and L_h a typical horizontal length scale. Whereas Saltzmann (2002) used these dimensionless variables to study the thermodynamic equations, the variables are equally suited to study Equation (3.1). This leads to a new dimensionless equation,

$$\frac{\partial H'}{\partial t'} = -\frac{L_v U_c}{L_h a} \nabla \cdot (H' \mathbf{U}') + B' \tag{3.20}$$

The mass balance B' is prescribed analytically. The ice flux $\nabla \cdot (H' \mathbf{U}')$ therefore contains all numerical errors. The factor in front of the ice flux, henceforth called flux number, determines the relative effect of these numerical errors in the total ice thickness change. On the one hand, if the flux number is small, the ice thickness change is dominated by the mass balance. This implies that the results do not suffer much from the numerical problems as shown in Figures 3.3 to 3.9. On the other hand, if the flux number is high, the ice flow, rather than mass balance, dominates the ice thickness change, which implies that the numerical errors may cause serious problems in the model results. For wet areas, for example, a is large and the mass balance is dominant. For dry areas, however, the numerical effects in the calculation of the ice flux dominate.

Figures 3.3 to 3.9 show that we need extremely small grid cells even when the modelled ice sheets are large and smoother than small glaciers. For small glaciers, the flux number $L_v U_c / L_h a$ will be relatively small (compared with the value on large, growing ice sheets). For example, a typical ice velocity for a mountain glacier is approximately 100 m a^{-1}. Typical mass balances have an order of magnitude of 1 to 10 m a^{-1}, and a typical size for a mountain glacier is 10 km with a typical thickness of 100 m. This results in a typical flux number value of 0.1.

We also need to distinguish between the centre and the margin of ice sheets. In the centre, the ice velocities are small, less than 1 m a^{-1}. The mass balance in the centre is small too, around 0.1 m a^{-1}. Together with a typical ice thickness of 1000 m and horizontal dimensions between 100 and 1000 km, this results in values for the flux number between 0.01 and 0.1. This is comparable to or smaller than for mountain glaciers. Thus, in the centre of the ice sheet the numerical effects in the ice flux term are not important. However, near the ice margin, the typical velocity is in the order of 100-1000 m a^{-1} and the mass balance around 1 m a^{-1}, resulting in values for the flux number between 0.1 and 10. This is larger than for a typical mountain glacier. Hence, compared with mountain glaciers, numerical effects in the ice flux calculation are much more important in the ice margin of large ice sheets. These marginal zones are also the sensitive locations that determine ice growth. Note that for a typical size L_h of 100 km, the flux number is higher

than for a typical size of 1000 km. This confirms the test results that the numerical problems mostly occur during the growth phase of an ice sheet model. Results of numerical tests for glaciers can not be extrapolated to ice sheets; we must expect different numerical behaviour for ice sheets and glaciers.

3.6 Conclusions

We assessed the effects of varying spatial discretisations through a series of experiments with simplified geometries in a one-dimensional and a two-dimensional vertically integrated ice flow model based on the shallow ice approximation. This approximation is widely used by climate researchers, making it essential to understand its numerical behaviour. The focus was not on resolving power of fine structures, but on the global behaviour of large, smooth ice sheets, where we included the feedback of the mass balance with height. Note that we cannot extend our results directly to situations where the mass balance does not agree with such a parameterisation. Note also that these results are only valid for stationary grids. We expected each of the discretisations that we used to perform well, given the size and geometry of the ice sheets. However, after testing for the sensitivities to initial conditions and the individual model parameters, we found that not all discretisations performed well:

- The widely used grid cell spacing of 20 km is far too coarse.
- The model's numerical behaviour is a strong function of initial conditions, local geometry and climate.
- The numerical errors increase nonlinearly over time due to the feedback between mass balance and surface height. This could have serious implications for research regarding the inception of large ice sheets.
- The numerical errors are associated with the calculation of the surface gradient. We improved the calculation of the surface gradient at the ice margin for type II models. This led to an improvement of the modelling results ranging from 0 to 10 percent.
- Type I models perform better than type II models. However, the poor stability properties of a type I model are a major disadvantage. It is not intrinsically clear which method should be preferred in which type of experiment.
- Dimension analysis can be used as a tool to explain in which cases numerical problems are to be expected.

3.7 Acknowledgments

The calculations were performed on the RADON cluster of IMAU, which was partly funded by the Utrecht Centre for Geosciences. This work was financed by Spinoza,

awarded by NWO to Professor J. Oerlemans. We wish to acknowledge Dr. R.C.A. Hindmarsh, Professor T.J. Hughes and an anonymous reviewer for their valuable comments.

Chapter 4

Recovering lateral variations in lithospheric strength from bedrock motion data using a coupled ice sheet-lithosphere model

A vertically integrated two-dimensional ice flow model was coupled to an elastic lithosphere-earth model to study the effects of lateral variations in lithospheric strength on local bedrock adjustment. We used a synthetic bedrock profile and a synthetic climate to model a characteristic ice sheet through an ice age cycle. Realistic differences in lithospheric strength altered the local bedrock adjustment up to 100 meters, the ice extent by tens of kilometers and the ice volume by several percent. Hence, when modeling ice sheets, it is essential to include information on lithospheric structure.

In addition, we used the coupled ice flow-lithosphere model to construct synthetic bedrock motion time series to assess their potential in resolving lithospheric structure. Inverse experiments showed that the model can resolve lateral variations in lithospheric strength from these bedrock motion time series, provided that we have data from both sides of a lateral transition in lithospheric strength. The inversion that solved for a lateral transition was able to find a solution that was consistent with all data, even if they were noisy. In the presence of lateral variations in lithospheric strength, there was no solution to the inverse problem for which all data were modeled correctly by a uniform lithospheric model. The synthetic data showed no significant sensitivity to the location of the tran-

This chapter has been published as: J. van den Berg, R.S.W. van de Wal and J. Oerlemans (2006). Recovering lateral variations in lithospheric strength from bedrock motion data using a coupled ice sheet-lithosphere model, *Journal of Geophysical Research*, **111**, B05409, doi: 10.1029/2005JB003790.

sition. Hence, we require information from independent sources, such as seismology or gravity, about the locations of transitions in lithospheric strength.

4.1 Introduction

To understand the earth's climate and to predict future climate change, it is essential to study the sensitivity of the earth's system to change. The growth and decay of large ice sheets were amongst the largest climate changes in the past million years. The physical processes controlling the evolution of ice sheets are generally studied with dynamical ice flow models. Most studies consider the response of the ice to the upper boundary conditions, i.e. climate and sea level. However, in this paper we focus on the lower boundary, i.e. the lithosphere.

Bending of the outer layers of the earth as response to the added weight of ice results in a isostatic adjustment of the bedrock of up to one third of the ice thickness. This effect influences surface temperature, basal topography, and the stress field in the ice. To calculate the ice evolution as accurately as possible, dynamical ice flow models incorporate this vertical displacement by assuming an Earth rheology. Le Meur and Huybrechts (1996) have shown that a simple Earth model, namely a purely elastic lithosphere with uniform thickness and strength underlain by a uniform mantle with a single relaxation time, works reasonably well compared to more realistic, but also computationally more demanding, viscoelastic earth models, with several laterally uniform layers.

However, seismological and gravitational methods have suggested large lateral differences in lithospheric structure (Poudjom Djomani et al., 1999; Bannister et al., 2003; Darbyshire et al., 2004; Pérez-Gussinye and Watts, 2005). For example, there are strong indications for a large transition under the Trans Antarctic Mountains from weak lithosphere in the western part of the continent to strong lithosphere in the eastern part (Stern and Ten Brink, 1989; Bannister et al., 2003). Seismological and gravitational methods are very useful in retrieving information on lithospheric structure, but they have some drawbacks as well. For instance, seismological data are difficult to interpret in terms of actual strength, since lithospheric strength is a function of composition, structure, and tectonic history (Braitenberg et al., 2002). Gravitational methods experience difficulties when the bedrock is not in isostatic equilibrium, or if the load is not well known or highly variable, for example in regions with a glaciation history.

To be able to use gravitational methods in (formerly) glaciated regions, an ice history, such as ICE-3G and its descendants, was constructed from glacial isostatic adjustment data (e.g. Tushingham and Peltier, 1991; Milne et al., 2002). This ice history was then assumed to be a known loading history to study the rheological properties of the earth (e.g. Wolf, 1993; Vermeersen and Sabadini, 1999; Di Donato et al., 2000; Kaufmann and Wu, 2002). Such an ice history is derived from (mostly sea level) observations and does not include ice mechanics.

Recently, experiments have been performed using these ice loading histories on the occurrence of possible lateral transitions in lithospheric strength. For example, Kaufmann and others (2000), Kaufmann and Wu (2002), and Zhong and others (2003) have

experimented with the effects of lateral variations in lithospheric strength on local glacial isostatic adjustment data. Kaufmann and others (2000) concluded that realistic lateral variations in strength underneath these prescribed ice loads (no ice dynamics) could give differences in local sea level data up to ten meters. Kaufmann and others (2005) showed that modeled isostatic adjustments strongly depended on the chosen ice history. In this latter paper one of the ice histories was based on a dynamical ice flow model. To resolve lateral variations in lithospheric strength both Kaufmann and Wu (2002) and Zhong and others (2003) proposed an inverse procedure with several laterally homogeneous models and local data. Variations in local estimates between different regions indicated variations in lithospheric structure. In this paper we present a new approach to retrieve information on lateral variations in lithospheric strength. This new method is based on the addition of a dynamical ice flow model to the inverse procedure.

Usually, ice evolution in a dynamical ice flow model is forced by a climate model. Such a climate model is derived from isotope measurements from ice and/or ocean sediment cores. This procedure is completely independent from the glacial isostatic adjustment data ice histories, such as ICE-3G. Moreover, the ice thickness distribution in these ice histories is generally based on optimization procedures, whereas dynamical ice flow models use a description of ice rheology. Hence, ice histories, such as ICE-3G, and dynamical ice flow models differ in both the underlying dataset and the modeling approach. Therefore, dynamical ice flow models provide an additional, independent source of information, which can be used to invert for lithospheric structure.

As mentioned before, dynamical ice flow models need to include isostatic adjustment calculations to reach the most accurate understanding of the ice thickness and extent throughout glacial cycles. Therefore, we constructed a new dynamically fully coupled ice sheet-earth model. We used a relatively simple earth model based on a purely elastic lithosphere including lateral variations in strength underlain by a uniform mantle with a single relaxation time as described in Section 4.2. This earth model was coupled to an ice model based on the shallow ice approximation as described in Section 4.3. Section 4.4 shows a characteristic ice sheet evolution for three different earth models to illustrate the full model. This ice-earth model was then used in a synthetic approach to assess an inverse procedure to resolve lateral variations in lithospheric strength from vertical isostatic bedrock adjustment data (Section 4.5).

4.2 The lithospheric model

The response of the solid earth to an ice-load can to first order be described by the bending or flexure of an elastic lithosphere combined with a time delay due to the viscous properties of the mantle below. If we assume that the elastic properties and the thickness of the lithosphere are constant throughout the plate, the behavior of the lithosphere can be described by a well-known fourth-order differential equation (e.g Turcotte and Schubert, 2002; Van der Veen, 1999; Brotchie and Silvester, 1969), which can be solved analytically for a given load, q_{load}:

$$D\nabla^4 w - q = 0, \tag{4.1}$$

where w is the vertical deflection, ∇ is the two-dimensional biharmonic operator, $q = q_{load} - \rho_m g w$ is the load minus the buoyancy of the mantle, and D is called the flexural rigidity and is a measure for the strength of the lithosphere. This is defined as

$$D = \frac{Eh^3}{12\left(1-\nu^2\right)}, \tag{4.2}$$

where h is the thickness of the elastic lithosphere, and E and ν are elastic parameters, respectively Young's modulus and Poisson's ratio.

For the general case where the elastic properties are not homogeneous, we cannot use the standard flexural equation presented in equation (4.1). For those cases we have to use a more general equation (for a more detailed derivation, see Chapter 2),

$$(\mathbf{L}\nabla)^T \mathbf{D}' \mathbf{L}\nabla w - q = 0, \tag{4.3}$$

where $(\mathbf{L}\nabla)$ is given by

$$(\mathbf{L}\nabla) = \left[\begin{array}{ccc} \frac{\partial^2}{\partial x^2} & \frac{\partial^2}{\partial y^2} & 2\frac{\partial^2}{\partial x \partial y} \end{array} \right]^T, \tag{4.4}$$

and the matrix $\mathbf{D}'$ is given by

$$\mathbf{D}' = D \left[\begin{array}{ccc} 1 & \nu & 0 \\ \nu & 1 & 0 \\ 0 & 0 & (1-\nu)/2 \end{array} \right], \tag{4.5}$$

Note that when D is constant, equation (4.3) reduces to equation (4.1).

As we are interested in lateral variations in lithospheric strength we use equations (4.3) to (4.5) to describe the vertical motion of the lithosphere.

Equations (4.3) to (4.5) describe an instantaneous elastic response. The earth however cannot respond instantaneously, since the mantle below has a nonzero viscosity. Therefore, the temporal response has a time delay and is calculated as (e.g. Van der Veen, 1999):

$$\frac{\partial b}{\partial t} = -\frac{1}{\tau}\left(b + w - b_0\right). \tag{4.6}$$

This is a simple first order approach in which we characterize the response of the mantle with one single relaxation time τ, commonly used in glaciological applications with a value of 3000 years. The parameter w is the total subsidence as calculated by the lithospheric model, b is the height of the bedrock, and b_0 is the initial topography, hence topography without ice. The Earth was not adjusted each time step of the ice model, but every ten years instead. This is allowed, since this is much less than τ.

4.2.1 Numerical properties of the lithospheric model

We have numerically solved equation (4.3) on a square equidistant grid with first order central differencing, resulting in a completely implicit procedure. At the boundaries we set the deflection w as well as its gradient over that specific boundary to zero.

We performed several discretisation tests for varying gridpoint distances. For coarse grids (Δx>40 kilometers), the solution was inaccurate. For fine grids (Δx<20 kilometers), the solutions were numerically unstable because the ice sheet surface was too smooth to calculate surface derivatives up to fourth order within machine precision. Therefore, we used a gridpoint distance Δx of thirty kilometers. Note that these results are valid for the typically smooth, large ice sheets we used in this manuscript. For specific applications the grid-requirements could be different.

We know from the analytical solution to equation (4.1) that the response of the lithosphere to an arbitrary load is characterized by a large deflection underneath the load and a positive, and small peripheral bulge outside the load. The total vertical movement is controlled by the flexural rigidity (D). Since the boundary conditions require that the deflection is zero at the boundaries of the domain, the calculated deflections are valid as long as the domain boundaries are after the bulge, where the deflections are very small. For this reason we used a domain of 3000 by 3000 kilometers where the ice load never had a radius larger than approximately 600 kilometers.

In this paper we modeled transitions in flexural rigidity over several orders of magnitude. Several tests with varying taper lengths showed that these very large transitions require a horizontal scale of approximately 300 kilometers width to avoid numerical instabilities. As our interest is in the continental scales, this is not a severe restriction.

4.2.2 Response of the lithosphere to a parabolic load

As an example of the lithospheric part of the algorithm we show the response of three lithospheric models to a radially symmetric parabolic load with a radius of 500 kilometers (Figure 4.1b). Figure 4.1a shows the flexural rigidities of the three lithospheric models. We used two lithospheric models with a constant flexural rigidity; one with $D = 10^{22}$ Nm (a typical value for oceanic lithosphere) and one with $D = 10^{25}$ Nm (a typical value for strong, continental lithosphere). The third model contained a transition with a width of 300 kilometers from $D = 10^{25}$ Nm to $D = 10^{22}$ Nm, with the center of the transition at a radial distance of 500 kilometers. As such, the ice margin is directly located above the transition. This corresponds to a situation where the ice margin is positioned on the transition from continental to oceanic lithosphere. The transition is modeled with a combination of two error-functions, characterized by a rapid change followed by a more gradual asymptotic behavior towards the final values. Figure 4.1c shows the resulting deflections as a function of distance. We see differences up to 100 meters between the solutions. Underneath the load the curve for the variable lithosphere resembles the one for the strong lithosphere, which makes sense since the transition only occurs at 500 kilometers distance from the center. At the transition however, the curve for the variable lithosphere shifts towards the one for the weak lithosphere; the bulge moves closer to the margin of the load and is higher than for both other curves. These results are generally in agreement with Kaufmann and others (2000) and Kaufmann and Wu (2002). The result implies that the possible magnitude of a peripheral bulge strongly depends on the lateral variation in lithospheric strength.

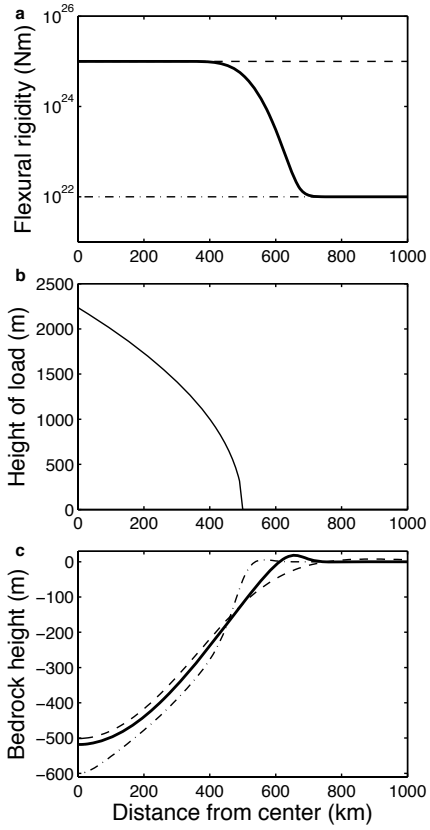

Figure 4.1: (a) Flexural rigidity as a function of distance from the center. (b) Height of load as a function of distance from the center. (c) Deflection as a function of distance from the center. The dashed and dash-dotted lines represent the analytical solutions for $D = 10^{25}$ Nm and $D = 10^{22}$ Nm, respectively.

4.3 The ice model

The ice model is based on the vertically integrated continuity equation (e.g. Van der Veen, 1999):

$$\frac{\partial H}{\partial t} = -\nabla \cdot (H\,\mathbf{U}) + B, \tag{4.7}$$

where H is the ice thickness, $\mathbf{U}$ is the vertically averaged horizontal velocity, and B is the mass balance, which is the net increase or decrease of local ice thickness in meters of ice per unit time due to snow fall or ice melt at the surface of the ice sheet. We used the shallow ice approximation (e.g. Hutter, 1983; Van der Veen, 1999), which assumes that the horizontal extent is much larger than the ice thickness. For a two-dimensional model without sliding, the expression for the vertical mean horizontal velocity reduces to the deformation velocity, which is given by

$$\mathbf{U} = \frac{-2}{n+2}\,(\rho_i\,g)^n\,A\left[\frac{\partial h_s}{\partial x}^2 + \frac{\partial h_s}{\partial y}^2\right]^{\frac{n-1}{2}} \nabla h_s\,H^{n+1}, \tag{4.8}$$

where h_s is the surface height, ρ_i is the ice density, g the gravitational acceleration, and A and n are rheological parameters, where n is set to 3. The parameter A is assumed to be constant throughout the ice.

A good first order approximation for the mass balance is a linear profile for which the only variable is height above a reference level;

$$B = min\left(B_{max}, \beta\,(h_s - ELA)\right), \tag{4.9}$$

where β is the mass balance gradient in yr^{-1} and ELA the equilibrium line altitude in meters. In general temperatures decrease with increasing altitude. We assume that the total precipitation is constant with altitude. The slope of the mass balance profile is then caused by the net effect of decreasing melt with altitude and the simultaneous increase of the snow fraction of the precipitation. The part of the profile where B approaches the value B_{max} reflects the absence of melt at high elevations where all precipitation falls as snow. At the ELA the mass balance is zero, hence no net change in ice thickness due to accumulation or melt.

We solved the system, given by equations (4.7) to (4.9), on a two-dimensional equidistant square grid with central differencing in the spatial domain and a gridpoint distance of two kilometers for a total domain of 1500 by 1500 kilometers. The model corresponds to the type II ice models from the EISMINT experiments (Huybrechts et al., 1996), which is widely used by ice sheet modelers. For the time integration an Alternating Direction Implicit (ADI) method is used (e.g. Mahaffy, 1976; Huybrechts, 1992). The ice thickness at all boundaries is set to zero.

The gridpoint distance and the domain size are not the same as for the lithospheric model. We required a fine grid for the ice to be calculated accurately. To obtain the response for a gridpoint in the earth-domain, we applied an average of the overlapping

β (yr^{-1})	0.005
ELA (m)	150 (first 100,000 years), 500 (final 20,000 years)
B_{max} (m yr^{-1})	0.1
τ (yr)	3000
b_{max} (m)	400
γ (m km^{-1})	1.3

Table 4.1: Parameters for the experiments: β is the mass balance gradient, ELA the altitude where the mass balance is zero, B_{max} is the maximum mass balance, τ is the characteristic relaxation time for the mantle, b_{max} is the highest point in the bedrock topography without ice, and γ is the gradient in the bedrock topography without ice.

gridpoints in the ice-domain. Once the earth response was calculated, we interpolated the calculated bedrock elevation using bicubic splines to the ice-domain. This procedure works as long as the bedrock response is a smooth function of x and y.

4.4 A coupled synthetic ice sheet-bedrock evolution

To illustrate the combined effect of the ice and lithosphere model, we considered the development of an ice sheet over a period of 100,000 years followed by partial melt over a period of 20,000 years. We used three lithospheric models: two models with a constant rigidity; one weak lithosphere with $D = 10^{22}$ Nm, and one strong lithosphere with $D = 10^{25}$ Nm. The third lithospheric model contained a transition of 300 kilometers width from $D = 10^{22}$ Nm in the western (or left) half of the domain to $D = 10^{25}$ Nm in the eastern (or right) half of the domain (Figures 4.2a and 4.3a). This synthetic geometry was inspired by the geological structure of Antarctica, where there are strong indications for a transition between weak lithosphere west of the Trans Antarctic Mountains (TAM) and strong lithosphere to the east. The values for the flexural rigidity are representative for that transition (Stern and Ten Brink, 1989).

We prescribed the initial bedrock profile as

$$b_0(r) = b_{max} - \gamma\, r, \tag{4.10}$$

with b_0 the initial bedrock height in meters, b_{max} the maximum initial bedrock height, γ the initial bedrock gradient, and $r = \sqrt{x^2 + y^2}$ the distance from the center in kilometers. The parameterization of the mass balance as an altitude-dependent parameter requires the introduction of a surface slope. Without the surface slope, the ice model is numerically unstable.

Table 4.1 shows the parameter values for this experiment. In spite of the lithospheric model, the prescribed mass balance profile is not inspired by the climate on Antarctica, making this a purely theoretical experiment. The equilibrium line altitude ELA was 150

meters during the first 100,000 years. Results are presented in Figure 4.2. Figure 4.2b shows an east-west profile through the domain at this time, which we will call Last Glacial Maximum (LGM). After these 100,000 years ELA was consecutively moved up to 500 meters for a duration of 20,000 years. Figure 4.3 shows the results after this deglaciation. Figure 4.3b shows an east-west profile through the domain after this total of 120,000 years, which we will call present day (PD). Note that these profiles are not steady-state profiles, but time-slices. Figures 4.2c and 4.3c show the differences in bedrock heights between the different Earth models. Figures 4.2d and 4.3d show the resulting differences in ice thickness.

For the case with the variable lithosphere, the ice sheet resembles the ice sheet for the weak lithosphere on the weak part of the domain. On the strong part of the domain, the ice sheet resembles the ice sheet for the strong lithosphere. In the center of the domain the differences with the variable lithospheric model are smallest for the strong lithosphere. Since strong lithosphere has a larger region of influence (or larger flexural wavelength) than weak lithosphere, the strong part of the lithosphere dominates the transition region.

Fast melting occurs during the final 20,000 years of the cycle (Figure 4.3). The ice decreases more rapidly in ice extent than in ice thickness. The resulting ice sheet is almost as large as the transition in rigidity itself. As a result, the transition is much more noticeable in the bedrock response, giving more widespread differences between the three lithospheric models.

The ice extent is different for each earth model, causing the differences in ice height to be 100 meters or more in the sensitive marginal areas. The differences in ice extent for the realistic strengths used in Figures 4.2 and 4.3 are tens of kilometers, making this an important feature. This marks the importance for ice modeling of taking into account the dynamical response of the ice to the strength of the lithosphere.

Figure 4.4 shows the corresponding bedrock height-change for specific locations as a function of time together with the resulting ice volume. Differences in bedrock deflection between the different lithospheric models are approximately 20-30 percent. We observe that not only the ice extent, but also the ice volume is a function of lithospheric strength. Differences in lithospheric strength lead to differences in resulting ice volume of up to ten percent. We performed tests with different ice rheologies by varying the flow parameter A by thirty percent. This did not influence these relative volume differences between the different Earth models. Varying the climate parameters such as the mass balance β and the maximum mass balance B_{max} did not have a large effect either. Again, this clearly marks the importance of taking into account the dynamical coupling between ice and earth for the modeling of ice. Not just taking into account changes in the rigidity, but also knowing the absolute value of the strength is important.

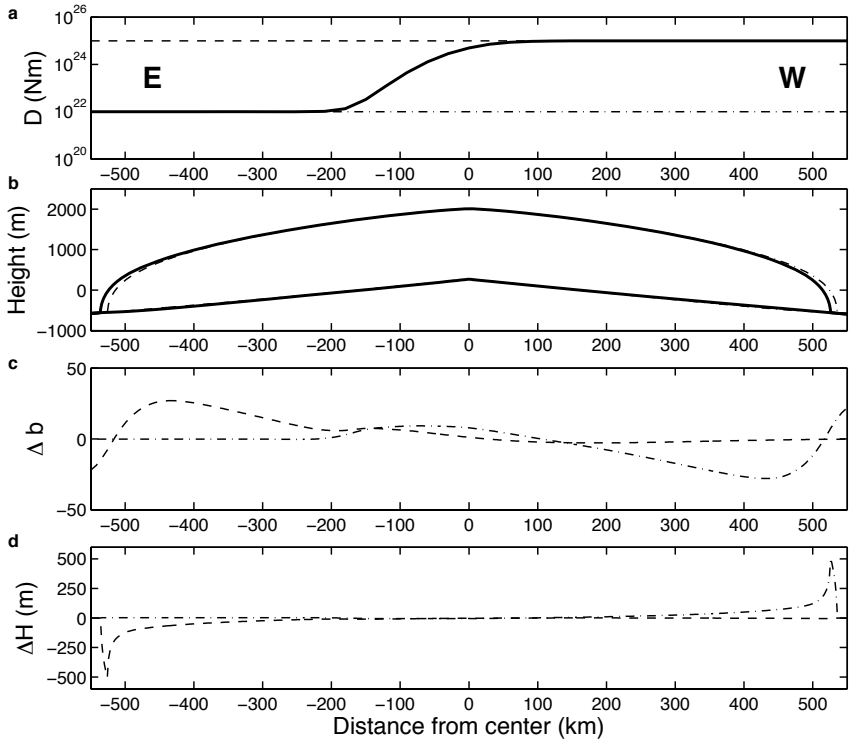

Figure 4.2: Results after 100,000 years of ice growth. (a) Flexural rigidity for the three lithospheric models; the variable rigidity (solid), $D = 10^{22}$ Nm (dash-dotted), and $D = 10^{25}$ Nm (dashed). (b) West-East cross-section of an ice sheet at LGM. (c) Differences in bedrock height of the constant lithospheric model with the variable lithospheric models, i.e. $b_{constant} - b_{variable}$, as a function of distance from the center along the cross-section. (d) Similar as (c), but now for ice thickness differences.

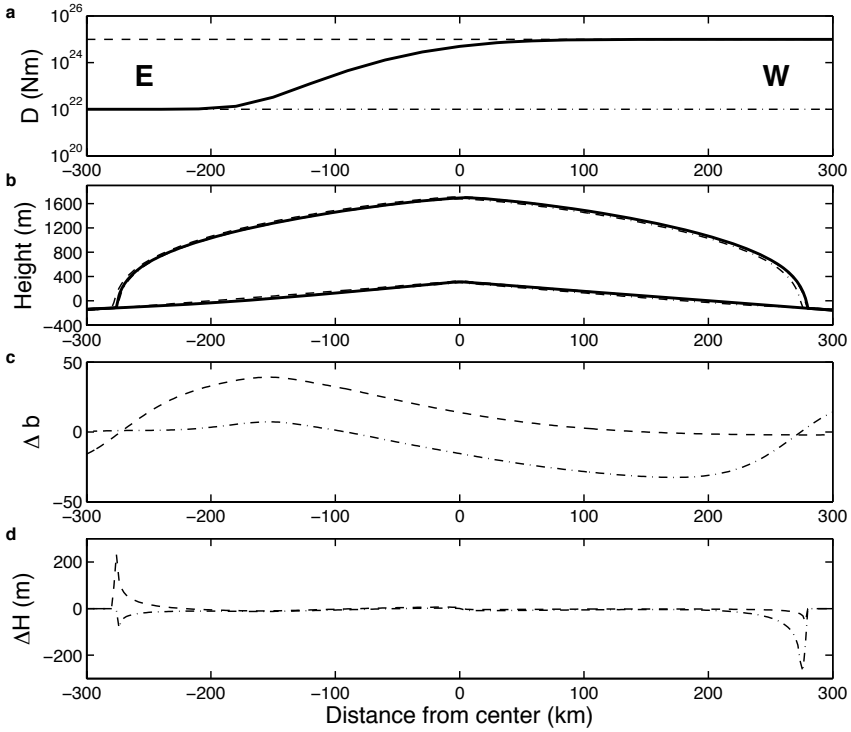

Figure 4.3: Results after 20,000 years of deglaciation. (a) Flexural rigidity for the three lithospheric models; the variable rigidity (solid) and $D = 10^{22}$ Nm (dash-dotted) and $D = 10^{25}$ Nm (dashed). (b) West-East cross-section of an ice sheet at PD. (c) Differences in bedrock height of the constant lithospheric model with the variable lithospheric models. i.e. $b_{constant} - b_{variable}$, as a function of distance from the center along the cross-section. (d) Similar as (c), but now for ice thickness differences.

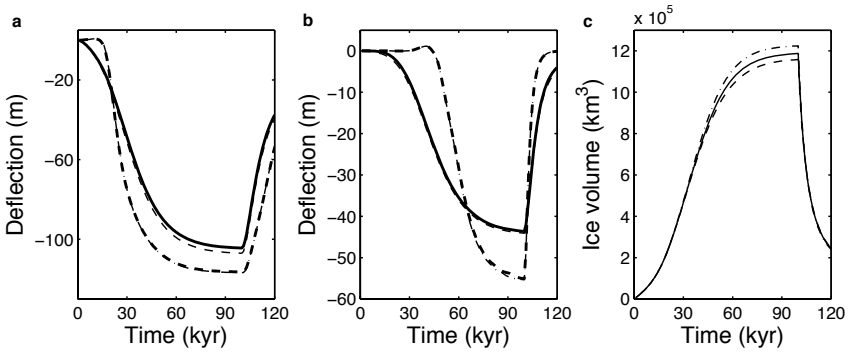

Figure 4.4: (a) Bedrock data at 250 km distance from the center for the eastern part of the variable lithosphere (solid, thick curve), the western part of the variable lithosphere (dashed, thick curve), and the two constant lithospheres (Strong-dashed, thin curve, weak-thin, dash-dotted curve). (b) Same figure for a distance of 500 km from the center. (c) Ice volume curve for the variable lithosphere and the two constant lithospheres. (Weak-dash-dotted curve, strong-dashed curve).

4.5 Reconstruction of lithospheric strength from synthetic bedrock data

Relative sea level curves contain both the signals from actual sea level changes and information about the bedrock motion. Close to the ice sheet they contain information on the flexural behavior of the lithosphere (e.g. Milne et al., 2002). The use of these data requires coupling of the dynamical models presented here to a full gravitational sea level model. We assume that we can extract the isostatic adjustment of the bedrock from the sea level curves. Hence, we only use the data of the bedrock motion and perform several experiments to assess their ability to provide information on lithospheric strength.

The climate, initial bedrock topography, and calculated bedrock height yield the ice thickness. This is in turn input for the bedrock model. The output from the bedrock model is bedrock height, which is used for the next time step in the ice model and so on. Note the dynamical coupling between ice and Earth. In the following experiments the climate and initial bedrock topography are assumed to be known and fixed to the values of the previous section, presented in Table 4.1. The data are given by the resulting bedrock height time series. This leaves only the lithospheric strength model as unknown parameter, which we aim to recover from the bedrock height data. The ice sheet responds both to climate and to the lithosphere, hence will differ in ice thickness and extent for different lithospheric models, as shown in Section 4.4.

Figure 4.5a shows the ”true” synthetic geometry of the lithosphere, with an eastern and western value for D with the transition in the center of the continent (as indicated by the thick solid line in the center of the domain), which we aim to recover from synthetic

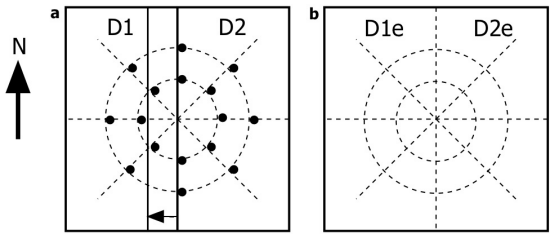

Figure 4.5: Geometry of the inversion. Plot a shows the geometry of the true model with $D1 = 10^{22}$ Nm and $D2 = 10^{25}$ Nm. It also shows the locations of the bedrock-data in eight directions from the center (North, North-East, East, South-East, South, South-West, West and North-West) and at two distances from the center (r=250 and 500 km). In total there are 16 bedrock curves as a function of time. Plot b shows the geometry of the inversion. We invert for two parameters ($D1e$ and $D2e$). The generated bedrock data are in the same locations as in the left plot.

bedrock data. We used a square domain with a transition from weak to strong lithosphere in the center, such that the western part of the domain is weak ($D1 = 10^{22}$ Nm), and the eastern part is strong ($D2 = 10^{25}$ Nm). The transition width is 300 kilometers. Figure 4.5a also shows a thin, vertical, solid line and an arrow. We will come back to this in Section 4.5.2.

For this "true" lithospheric strength model we created the "true" bedrock response data d^t. Figure 4.5a shows the locations; we took data d^t from eight directions (North, North-East, East, South-East, South, South-West, West, and North-West) and at two distances from the center (250 and 500 kilometers). In total we generated 16 bedrock height curves as a function of time. A data point was calculated every 1000 years, hence we generated 120 data points for each location for the glacial-interglacial run of 120 kyears. We only used the last twenty time points of the total 120, since these are from the deglaciation-part of the curves, which in practice is the only part of the bedrock curves we may expect to be available from real observations.

4.5.1 Single strength inversion

In the first experiment we investigated whether we could find a single strength for the entire continent (Figure 4.5b, $D1e = D2e = De$) which provides approximately the same bedrock adjustment data as obtained from the "true" lithospheric strength model with a transition from weak to strong lithosphere. We modeled bedrock adjustment data d^e for several single strengths De at the same times and locations as the "true" data d^t. We then compared these different data d^e with the "true" data d^t. For the comparison we

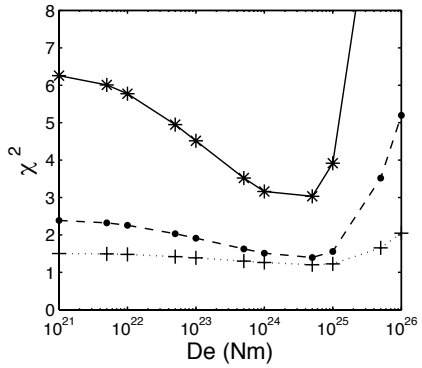

Figure 4.6: χ^2-distribution as a function of De for bedrock data for five percent noise (solid), ten percent noise (dashed) and twenty percent noise (dotted).

used a cost function based on the χ-squared test:

$$\chi^2 = \frac{1}{NT} \sum_n \sum_k \left(\frac{\left(d^t_{n,k} - d^e_{n,k} \right)^2}{\left(\sigma^t_{n,k} \right)^2} \right) \tag{4.11}$$

where the sum n is over all the data locations (N=16) and the sum k is over all times (T=20). The value for χ^2 is different for each single strength De and has a minimum for that value of De where the modeled bedrock data d^e are closest to the "true" data d^t. Once χ^2 is equal to one, the modeled bedrock data d^e match the "true" data d^t within one standard deviation.

Figure 4.6 shows χ^2 as a function of De for an addition of either five, ten or twenty percent gaussian noise in the "true" data d^t. The resulting best estimate De is roughly at the average of both true rigidities. An uncertainty of twenty percent is not uncommon for sea level data, but the resulting estimate for the lithospheric strength is quite robust; the minimum in misfit remains significant.

Figure 4.7a shows χ^2 for data from a specific direction only. We do not show results from the South-East and the North-West, because these data are the same for the North-East and the South-West respectively due to symmetry. The data from the western part of the domain yield as best estimate for De the "true" value $D1$. Similarly, for data from the eastern part of the domain, the best estimate for De is equal to the "true" value $D2$. If the direction is not perpendicular (i.e. North-East or South-West) to the transition, the resulting best estimate De does not change much compared to the perpendicular directions East and West; the strong estimate is not affected, the weak estimate is a little different, but the minimum is very flat, which is a result the logarithmic scale. When the data from the North are used, we find the average between $D1$ and $D2$. This value is also equal to the local value, but it is not possible to distinguish whether the result is based on the local

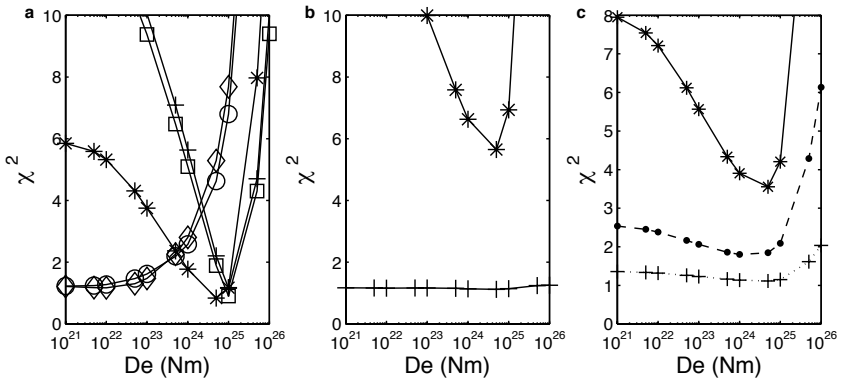

Figure 4.7: χ^2-distribution as a function of De for the bedrock data with five percent noise. (a) Cost function for all data in one specific direction (stars for North, plusses for North-East, squares for East, circles for South-West and diamonds for West) are used. (b) Misfit when all data at specific distances are used (stars for 250 km, plusses for 500 km). (c) Similar to Figure 4.6, but now the estimates De are calculated with a prescribed ice history.

value or the average. The values of χ^2 in Figure 4.7a do approach one unlike the values for low noise levels in Figure 4.6. This implies that there is no single value De for the entire domain for which data on both sides of the transition are modeled well. This means that it is not possible to perform a good inversion for a single strength in a consistent model if the true situation has a variable lithospheric strength.

Figure 4.7b shows χ^2 for data from one distance only, but using all directions. The curve with the clearest minimum is the one for a distance of 250 kilometers from the center. The bedrock at these locations is covered by ice for a large part of the ice history, but is located near the ice margin for the present day situation, Figure 4.3. Further from the margin, not much happened to the bedrock, hence a value for χ^2 close to one, but also hardly a minimum. This implies that, as expected, we need data as close to the ice as possible in order to discriminate between several values for lithospheric strength.

Effects of uncertainties in the ice and earth model

To assess the effects of uncertainties in the ice model, we also performed the experiment without the full dynamical coupling of ice and lithosphere. To acquire an ice history, we calculated, with the dynamical coupling, for a uniform lithospheric strength the corresponding ice sheet evolution. For this specific ice history, we saved the ice thicknesses every 500 years. These ice thicknesses were then used as a prescribed ice history. Hence, the modeled bedrock adjustment data d^e for each lithospheric strength De now shared the same input, namely this ice history prescribed every 500 years, instead of the dynamically

corresponding ice sheet. This procedure did not influence the "true" data d^t, these were kept the same as in the previous experiments. Only the estimates De were assessed with the new ice history.

Figure 4.7c shows the resulting χ^2 for an ice history corresponding to a lithospheric strength De of 10^{22} Nm. We repeated this experiment with several ice histories corresponding to several lithospheric strengths, but the results were similar to the result in Figure 4.7c. A few things can be observed. First, when the uncertainties in the "true" data are high, there is no change in the χ^2 values compared to the fully coupled results, Figure 4.6. Only for small (five to ten percent) uncertainties in the "true" data d^t there is a difference. The minimum is unaffected. However, the χ^2 values surrounding the minimum are higher. Interestingly, the χ^2 value for De=10^{22} is also higher than with the full dynamical coupling, even though this value was used to calculate the ice history. This indicates the effect of adjusting the ice history only every 500 years instead of each timestep.

To further assess the influence of uncertainties in the ice model we calculated new "true" data d^t corresponding to a different climate. We then used the original climate to estimate the lithospheric strength De, this time with the full dynamical coupling between ice and earth. In the case of a warmer "true" climate, this meant that the estimated values of De were assessed with an ice sheet that was too large. In the case of a colder "true" climate, the estimated ice sheets were too small. The resulting χ^2 values were very sensitive to the climate used to calculate the ice sheets. This is in agreement with the results of Kaufman and others (2005), who found that modeled crustal motions depended strongly on the specific ice history. The minimum value was shifted to a smaller value for De for the colder "true" climate, and to a larger value for De for the warmer "true" climate. This shift was associated with the bedrock adjustment near the ice margin. This is as expected since large ice sheets are generally not sensitive to the lithosphere in the center of the ice sheet.

To assess the influence of uncertainties in the earth model, we calculated new "true" data d^t corresponding to a different relaxation time τ and performed the experiment similarly to the different climate scenario, hence with the fully coupled model. The resulting χ^2 values were again very sensitive to this parameter. The resulting best estimate of the lithospheric strength was influenced, indicating the well known strong sensitivity of bedrock data to the viscosity of the mantle. This is in agreement with Kaufmann and Wu (2002), who found a trade-off between lithospheric structure and asthenospheric viscosity. The current lithosphere model however, is not adequate to study mantle viscosities. Therefore, we assume the relaxation time is known.

4.5.2 Variable strength inversion

Fixed location of transition

We continue the experiments with an inversion for variable strength of the lithosphere. Figure 4.5a again shows the geometry of the "true" model, which is the same as in the previous section. Instead of estimating a single value $D1e = D2e = De$, our objective is to find estimates for both a western value $D1e$ for the left part of the domain and an eastern

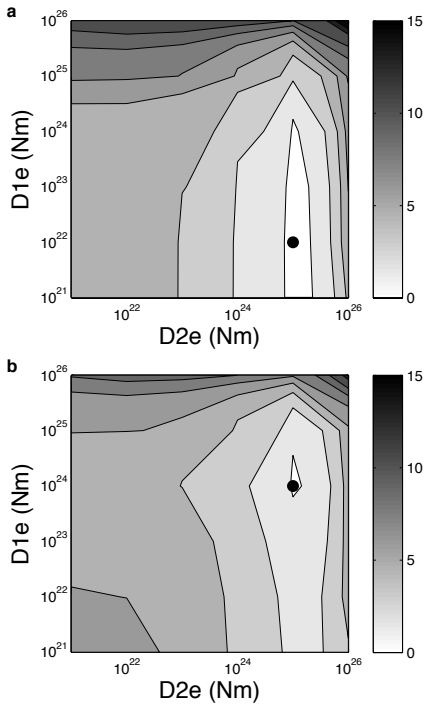

Figure 4.8: (a) The χ^2-distribution as a function of $D1e$ and $D2e$ for the case where the transition is in the center of the domain. (b) Similar to (a), but now the transition is moved 200 km to the west. The inversion, however, is still performed with the boundary between cells in the center of the domain, Figure 4.5. The contour lines are drawn at intervals of 1.5 starting at zero.

value $D2e$ for the right part of the domain. We modeled data d^e with the full lithospheric model for several transitions in strengths from $D1e$ to $D2e$ and compared these data with the "true" data d^t with equation (4.11). The ice sheets were again calculated with the dynamical coupling between ice and Earth. Figure 4.8a shows the cost function χ^2 for each value of $D1e$ and $D2e$ for a five percent gaussian noise level in the true data d^t. The minimum reflects the "true" values $D1$ and $D2$. The values for χ^2 are much closer to one than in Figure 4.6 (solid line), indicating that, as expected, this inversion leads to a better result.

Figure 4.5 also shows the geometry of the next experiment. Figure 4.5a again depicts the geometry of the "true" model. The transition from weak (west) to strong (east) lithosphere no longer coincides with the highest point on the domain. Instead, the transition is shifted to the west by 200 kilometers as indicated by the arrow and the thin solid line in Figure 4.5a. Otherwise all parameters remain unchanged. Figure 4.5b shows the ge-

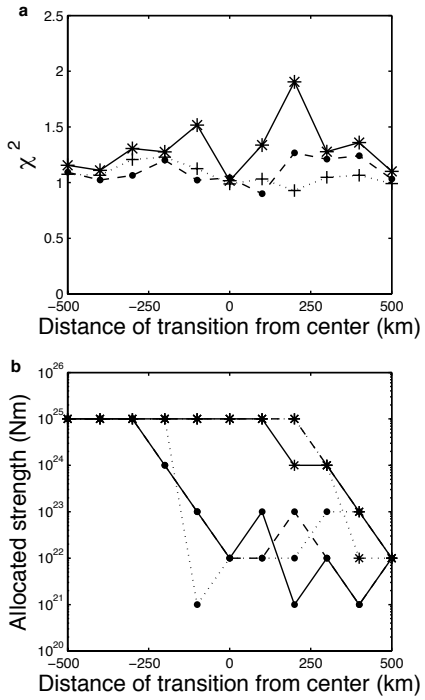

Figure 4.9: (a) Minimum of the χ^2-distributions for each of the locations of the transition for five percent noise (solid), ten percent noise (dash-dotted) and twenty percent noise (dotted). (b) The corresponding allocated strengths for the eastern half of the domain (stars) and the western half (closed circles) for the same noise-levels.

ometry of the model we used to estimate $D1e$ and $D2e$. Notice that in this figure the transition still coincides with the highest point of the domain. Thus, in this experiment we have changed the "true" data d^t rather than changing the estimated data d^e. Since no combination of $D1e$ and $D2e$ equals the "true" geometry, we expect the χ^2-distribution from this inversion to be worse than the χ^2-distribution from the second experiment. Figure 4.8b shows the resulting χ^2 for the third experiment for a five percent gaussian noise level. Indeed we see that the minimum value for χ^2 is slightly higher than in the previous experiment (1.5 compared to 1). More significantly however, the minimum is at different values for $D1e$ and $D2e$.

Moving transition

To examine this further, we performed the same experiment for varying locations of the transitions from weak to strong lithosphere. Furthermore, we added more noise to the

"true" data d^t to address the robustness of the results. Figure 4.9a shows the minimum values of the individual χ^2-distributions as a function of location of the transition. The solid curve is the curve calculated with five percent noise in the "true" data d^t. The curves show that we only find a value χ^2 equal to one if the location of the transition used to estimate $D1e$ and $D2e$ agrees with the position of the transition used for the calculation of the "true" data. However, if we add more noise to the "true" data, the differences in the values of the misfit at their minima turn out to be insignificant. Each inversion is equally good. Figure 4.9b shows the corresponding allocated values of $D1e$ (west) and $D2e$ (east) as a function of location of the transition. Whereas each estimate for $D1e$ and $D2e$ is equally good given the value of the misfit functions, the allocated values for the strength do change as a function of location of the transition, see also Figure 4.8b. If the transition lies more to the west, the allocated value in the west will be slightly larger.

So, we cannot distinguish between different locations of the transition given the values of the misfit functions, but we do have different estimates for $D1e$ and $D2e$. Hence, we conclude that we need some a priori information on the position of transitions in lithospheric strength from independent sources to estimate the rigidity of the lithosphere in the presence of lateral variations .

4.6 Discussion and conclusions

To resolve the strength of the lithosphere from sea level data we coupled a vertically integrated two-dimensional ice model to an Earth model. The Earth model consisted of an elastic lithosphere, where we incorporated lateral variations in lithospheric strength, with a single relaxation time due to the viscosity of the mantle.

To illustrate the performance of the model we used a synthetic bedrock profile and a synthetic climate to model a characteristic ice sheet through an ice age cycle. The ice sheet had a maximum radius of about 600 kilometers and was completely land-based. The example demonstrated the importance for ice modeling of including the coupling between ice and earth. Both the ice extent and the ice thicknesses were influenced resulting in significant differences in bedrock motions and ice volume. The ice volume differences resulting from different lithospheric strengths to calculate the isostatic bedrock adjustment, are about ten percent.

To exclude numerical instabilities, variations in D over several orders of magnitude are modeled over distances of 300 kilometers. We cannot model local anomalies. However, since our objective is to have a good representation of ice on continental scales, this is not considered to be a drawback of this approach. For example, the Trans Antarctic Mountains, which served as inspiration for the examples in this paper and cover a transition in flexural rigidity over several orders of magnitude, are about 300 kilometers wide.

The inverse method presented in this paper yields comparable results to previous studies based on prescribed ice histories (e.g. Kaufmann and Wu, 2002; Zhong et al., 2003). Our results indicate that it is possible to constrain lateral variations in lithospheric strength from vertical bedrock motions, as long as there are data on both sides of the transition and a-priori indications of the location. We stress that dynamical ice flow models are based on

different assumptions and datasets than the generally used ice histories, such as ICE-3G. In addition, our inverse procedure, yields the best fitting ice history for the most likely lithospheric model.

Our results show little sensitivity to gaussian noise in the data, as long as the noise levels do not exceed about twenty percent. The algorithm is most sensitive to data from underneath former ice sheets. The method is sensitive to systematic biases due to for example insufficient knowledge on mantle viscosities, i.e. relaxation times, or past climate conditions. However, the current lithospheric model is not suitable to study the effect of viscosity structure of the mantle. For example, the model only uses one relaxation time, while visco-elastic earth models generally have a spectrum of relaxation times. Therefore, more sensitivity studies should be done in practical applications, for example Antarctica and Scandinavia.

The model contains a purely elastic lithosphere. In reality, the lithosphere is probably visco-elastic and anomalies are more complicated than only a change in rigidity. The thin-plate model remains a mechanical tool which is able to model the accurate deflection underneath loads. The elastic thickness has no proven connection to the actual thickness of the lithosphere. Thus, the derived material properties are by no means the actual material properties of the lithosphere. Therefore, geodynamical implications should be examined critically. For now, if the elastic properties can be resolved this is enough to correctly model the ice sheets.

The method described here can be applied everywhere, provided that there are good constraints on the local climate as a function of time. Possible interesting applications include for example Antarctica, where indications exist for a large transition in lithospheric strength across the Trans Antarctic Mountains (e.g. Bannister et al., 2003; Stern and Ten Brink, 1989). Another possible application is Scandinavia where we expect an increase in lithospheric strength from the Atlantic coast towards cratonic Eurasia (e.g. Poudjom Djomani et al., 1999; Pérez-Gussinye and Watts, 2005).

4.7 Acknowledgments

The calculations were performed on the RADON cluster of IMAU, which was partly funded by the Utrecht Center for Geosciences. This work was financed by the Spinoza Award of NWO of Professor J. Oerlemans. We thank John Wahr and an anonymous reviewer for their valuable comments.

Chapter 5

A mass balance model for the Eurasian Ice Sheet for the last 120,000 years

We present a mass balance model for Eurasia which is based on the calculation of accumulation from a moisture balance concept. The model is forced with 500 hPa temperatures from GCM time slices at LGM and present day. The model simulates key characteristics, such as control on the size of ice sheets through the advection of moisture, asymmetric ice sheets due to advection of moisture and orography, and the drying of ice sheets when they grow. A simulation of the Eurasian ice sheet through a full glacial cycle shows that the model reproduces realistic ice sheets that compare well with geomorphological data. During the Middle Weichselian and the Late Weichselian, the model picks up the trend that the Scandinavian part of the ice grows towards the south and east whilst the ice sheet covering the Barents and Kara Seas remains relatively stable. However, the model seriously underestimates the observed ice extent in the Baltic area. Uncertainties in the temperature and the wind field limit the reliability of regional modelling results.

5.1 Introduction

The simulation of ice sheets throughout ice ages is very sensitive to the description of past climate conditions, and the conversion of the climatological variables into ice melt or accumulation, i.e. the mass balance. Methods to prescribe the mass balance in ice flow models are very diverse and range from simplified parameterizations to complicated procedures to calculate snowfall and ice melt. Simple methods, such as prescribing a dependence on location or altitude work fine for synthetic experiments, but are difficult to apply in realistic situations. The geometry of the Eurasian Ice Sheet, for example, is

This chapter has been submitted by to *Global and Planetary Change*.

strongly affected by the availability of moisture sources and wind direction (e.g. Velichko et al., 1997).

A calculation of the mass balance therefore usually consists of two steps; (i) the calculation of the ice mass melt or accumulation from the temperature and precipitation, and (ii) prescribing the historic variations in temperature and precipitation. In step (i) the accumulation is generally determined from the total precipitation with a simple relation between temperature and snow fraction. Several methods exist to estimate the amount of melt from an ice sheet, for example a Positive Degree Day (PDD) method, which models the ablation only as a function of temperature (Reeh, 1991; Braithwaite, 1995; Fabre et al., 1997; Charbit et al., 2002; Forsström and Greve, 2004; Huybrechts et al., 2004; Zweck and Huybrechts, 2005). As an alternative a parameterization as a function of both surface temperature and insolation can be used (Pollard, 1980; Oerlemans, 2001; Bintanja et al., 2002). Both methods produce equally good results, but have different sensitivities to temperature changes. In this paper we focus on step (ii); the description of temperature and precipitation as a function of time.

In regions currently covered with ice (e.g. Greenland and Antarctica) the observations are both spatially and temporally sparse. As such, prevailing climate conditions must be estimated with models. Recent attempts to force ice sheets with results from General Circulation Models (GCMs) are promising (e.g. Fabre et al., 1997; Bintanja et al., 2002; Charbit et al., 2002; Forsström and Greve, 2004; Huybrechts et al., 2004; Zweck and Huybrechts, 2005). These studies either dynamically couple the GCM for a short model run or steady state experiment, or they use one or more time slices of precipitation and temperature fields. In addition, temperature series deduced from ice cores as GRIP and Vostok or inverse experiments (Bintanja et al., 2005) are used to describe the transient changes from one climate state to the next. It is computationally impossible to dynamically couple a GCM to an ice flow model at sufficiently fine grid throughout a transient run for an entire ice age.

Despite this limitation, GCM runs at LGM, such as performed in the Paleoclimate Modelling Intercomparison Project (PMIP) 1 and 2 experiments, provide useful information on climate changes during the ice ages. Nevertheless, there are some severe drawbacks. A major issue is the sensitivity of the precipitation and surface temperatures to the ice distribution prescribed in the GCM. Another problem is resolution; local precipitation and temperature are not well resolved in areas such as Norway where the topography is highly variable and the land-sea contrast is large. Hence, it is problematic to interpolate and extrapolate the climatological fields from time slices.

Instead of prescribing the precipitation field, we propose to calculate the precipitation from a moisture balance as a function of temperature, wind and altitude (e.g. Sanberg and Oerlemans, 1983). Since altitude is directly coupled to ice sheet geometry, we can explicitly calculate changes in the precipitation pattern caused by changes in the configuration of the ice sheet. Hence, the ice sheet and calculation of the precipitation field are dynamically coupled. The precipitation model is tuned to present day conditions only, and otherwise evolves freely together with the ice sheet. Key characteristics of the model include (i) the advection of moisture governing the dimensions of ice sheets, (ii) the drying effect as ice sheets grow larger and higher, and (iii) the generation of asymmetric mass

balance profiles in the direction of the wind as a result of orography. These are generally believed to be essential features in modelling large ice sheets like the Eurasian Ice Sheet. A limitation of the model is that we do not calculate the general circulation. Hence, we cannot calculate changes in precipitation related to changes in the large scale circulation. Since the only variable is temperature, the model is ideally suited for sensitivity experiments to assess the important processes in the development of ice sheets.

Instead of forcing the mass balance model with surface temperatures from GCM time slices at present day and LGM conditions, we force the model with 500 hPa temperatures. These temperatures are far less sensitive to the ice distribution used in the GCM, and as such represent a more robust parameter to incorporate in a dynamical ice sheet model than surface temperatures. Moreover, 500 hPa temperatures are better representative for the calculation of the precipitation. In addition, the 500 hPa temperatures are still representative when surface properties change in time, whereas for surface temperatures this is not the case.

A similar precipitation model was successfully used to simulate present day climate in the UK and Patagonia (Hulton and Sugden, 1995; Purves and Hulton, 2000). In addition, Hulton and Sugden (1995) also studied the Patagonian climate under glacial conditions. These studies did not use a coupled ice flow model to directly model the response of an ice sheet. Letréguilly et al. (1993) did couple a similar precipitation model to an ice flow model, but only performed some sensitivity tests in Eurasia, hence not a full glacial run with representative temperature changes. Fabre et al. (1997) obtained bad results using a similar precipitation model coupled to an ice flow model for the entire Northern Hemisphere, which suggests that the model should be tuned locally. Moreover, Fabre et al. (1997) did not study a full glacial cycle.

We apply the mass balance model to a full glacial cycle over the last 120,000 years in Eurasia. Eurasia represents an interesting test case for the mass balance model; geomorphological data predict that whereas the Scandinavian part of the ice sheet generally showed growth towards LGM around 20 kyr BP, the ice sheet over the Barents and Kara Sea had its maximum early in the last ice age after which the trend was towards smaller ice cover (e.g. Svendsen et al., 2004). This opposite trend of growth versus shrink is a much debated feature; it may be an effect of a change in background wind field, orography, advection of moist or even dust deposition (Krinner et al., 2006). This trend has proven to be difficult to reproduce in dynamical ice flow modelling. To reproduce this different trend for different regions Siegert (Siegert et al., 2001; Svendsen et al., 2004) divided Eurasia into several prescribed climatological areas. Using the mass balance modelling approach as described here with a uniform tuning over the entire Eurasian domain may help us distinguish the importance of some of these essential processes such as advection of moisture and effects of orography in modelling climate change and dynamical ice sheets over time.

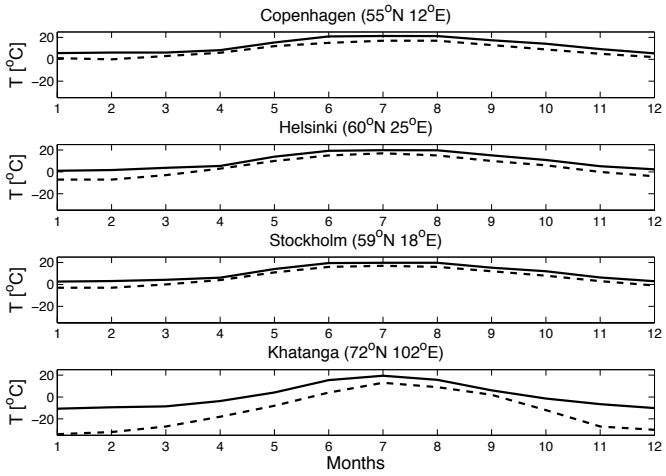

Figure 5.1: Monthly present day surface temperatures for several locations. The dashed line is the actual surface temperature, the solid line is the extrapolated 500 hPa temperature from HADCM3M2.

5.2 Climate forcing

5.2.1 Temperature

We force the mass balance model with monthly present day 500hPa temperatures of the model HADCM3M2 from the PMIP2 experiments which are extrapolated to the surface with a constant lapse rate of -6.5 ^{o}/km. A constant lapse rate does not include seasonal, geographical and altitudinal variations, but the available parameterizations are inadequate for the precise local conditions around ice sheets (Rennick, 1979).

Figure 5.1 shows monthly temperature series for several locations. Since the locations do not match completely with gridpoints, the solid line is calculated as the average temperature within one degree latitude, longitude of the location. All locations shown are in relatively flat areas close to the coast, which has considerable influence on the mean temperature. Taking this into account, the extrapolated 500hPa represent the surface temperatures well, except for the winter season in Khatanga. This is probably due to the extreme stability of the atmospheric boundary layer for these temperatures and the location far to the east in Siberia.

To calculate the ice history over the last 120,000 years, the present day monthly temperatures from HADCM3M2 are perturbed every 100 years with values representative for the Northern Hemisphere between 60^{o}N and 80^{o}N as published by Bintanja et al. (2005), Figure 5.2. Since these values represent average values for the entire model domain, the temperature perturbations are distributed locally over the model domain according to the distribution of relative temperature anomalies over the grid at LGM with respect to

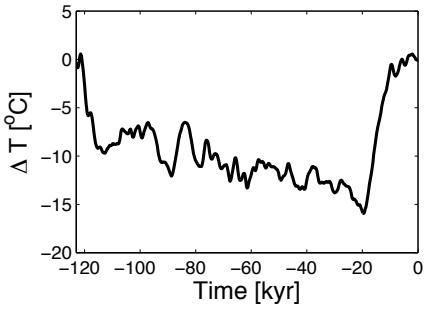

Figure 5.2: Temperature anomalies for the Northern Hemisphere between approximately 60^oN and 80^oN as deduced by Bintanja et al. (2005) for the last 120,000 years.

present day from HADCM3M2. This results in a larger temperature perturbation in the Barents and Kara Seas region than in Scandinavia. Temperature as a function of time is then calculated as

$$T_{z0}(x, y, t) = T_{z0}(x, y, 0) + \Delta T(t)\, Fr(x, y), \tag{5.1}$$

where $T_{z0}(x, y, t)$ is the temperature at zero altitude at location (x, y) and time t, where $t = 0$ corresponds to present day, $\Delta T(t)$ is the temperature perturbation a function of time as shown in Figure 5.2, and $Fr(x, y)$ is the distribution of relative temperature anomalies over the grid as calculated by HADCM3M2. Hence, we fix the seasonal cycle in temperature at the present day seasonal cycle due to a lack of sensible alternatives.

5.2.2 Precipitation

The precipitation is calculated from the following equation for the conservation of moisture (Sanberg and Oerlemans, 1983):

$$\frac{\partial W}{\partial t} = -\mathbf{v} \cdot \nabla W - (f_0 + f_1 S)\, W + (W_m - W)\, /t^*. \tag{5.2}$$

In this equation W is the amount of water vapour in an atmospheric column extending from the surface to the top of the atmosphere. The first term on the righthand side describes the advection of moist air by a horizontal wind field $\mathbf{v}$. The second term is the precipitation, which consists of two parts. The first part of the precipitation is the background precipitation governed by the constant f_0, the second part represents precipitation that occurs when air is forced upslope and saturation occurs. This process is governed by the constant f_1 and a slope term S ($S = max(0, \mathbf{v} \cdot \nabla h_s)$), where h_s is the surface altitude. The last term on the righthand side is the evaporation which is a function of a characteristic time scale t^* and the maximum amount of water vapour W_m. The evaporation is very important since it is the only source term in equation (5.2). The maximum

amount of water vapour in a column of air has a strong dependency on temperature and altitude, and is approximated using an integrated Clausius-Clapeyron curve (Paul, 1996) as

$$W_m(T, h_s) = \frac{e(T_0)}{\gamma R_v} \exp\left(\frac{L_v}{R_v T_0}\right) \left[\mathrm{Ei}\left(\frac{-L_v}{R_v (T - \gamma H_q)}\right) - \mathrm{Ei}\left(\frac{-L_v}{R_v (T - \gamma h_s)}\right)\right], \quad (5.3)$$

where $e(T_0)$ is the saturation vapour pressure at T_0=273.15 K, R_v is the gas constant for moist air, L_v is the latent heat of evaporation, H_q is the altitude of the top of the atmosphere, γ is the lapse rate of temperature with altitude, T is the annual mean surface temperature in degrees Kelvin and Ei is the exponential integral.

For a given annually averaged temperature field, topography, and wind field, a steady state W can be found by numerically evaluating equation (5.2). The parameters $f_{0,1}$ and t^* are tuned to present day conditions as provided by the IPCC Data Distribution Centre. The wind field is prescribed in the Cartesian grid as (v_x, v_y) =(3,0) m/s in the Scandinavian area, and (v_x, v_y) =(0.5,0) m/s in the Barents and Kara Seas area. These values are roughly based on the present day circulation as calculated by HADCM3M2 in the PMIP2 experiments. This wind field is shown interpolated for the Cartesian grid in Figure 5.3. The parameterization, also shown in Figure 5.3, is a strong simplification of the present day circulation as modelled by HADCM3M2. However, it does capture the essential advection of moist air from the Atlantic Ocean over Scandinavia. We compared the resulting precipitation for the parameterized wind field and the wind field from HADCM3M2. The results were very similar for present day conditions. Since the actual, local wind field is poorly known for paleo conditions, we preferred to continue with the computationally more efficient simple parameterization. In the Section Sensitivity tests we will show the effects of this choice. Figure 5.4 shows the resulting present day modelled annual precipitation. Figure 5.5 shows the differences with the IPCC data set. On average, Russia and Siberia are too dry, while Denmark, and the Baltic area are too wet. The maxima in Western Norway and the overall patterns however are well reproduced. The mean absolute difference over the entire grid is approximately 200 mm/year, which is a small misfit given the range of values of 100-3000 mm/yr over the grid.

Values and units of the various parameters are listed in Table 5.1. The resulting tuned parameters differ from the original tuning from Sanberg and Oerlemans (1983) for several reasons, of which different resolution and different input temperature field are the most important.

5.3 Mass balance

Once the moisture balance W is known, the monthly solid precipitation can be estimated from the distribution of precipitation throughout the year as calculated by HADCM3M2 in the PMIP2 experiments, where the monthly temperature determines if precipitation falls as snow.

f_0	s^{-1}	0.00001
f_1	s^{-1}	0.0001
t^*	s	3 days over water
		12 days over land
		30 days over (sea)ice
$e(T_0)$	Pa	610
γ	$^o\,m^{-1}$	-0.0065
R_v	$J\,kg^{-1}\,K^{-1}$	461.5
L_v	$J\,kg^{-1}$	2.5008x10^6
L_m	$J\,kg^{-1}$	3.34x10^5
H_q	m	10,000

Table 5.1: Values for the parameters, where f_0 and f_1 are parameters governing precipitation, t^* is a characteristic time scale for evaporation, $e(T_0)$ is the saturation vapour pressure, γ is the lapse rate, R_v is the gas constant for moist air, L_v is the latent heat of evaporation, H_q is the top of the atmosphere, and L_m is the latent heat of melt.

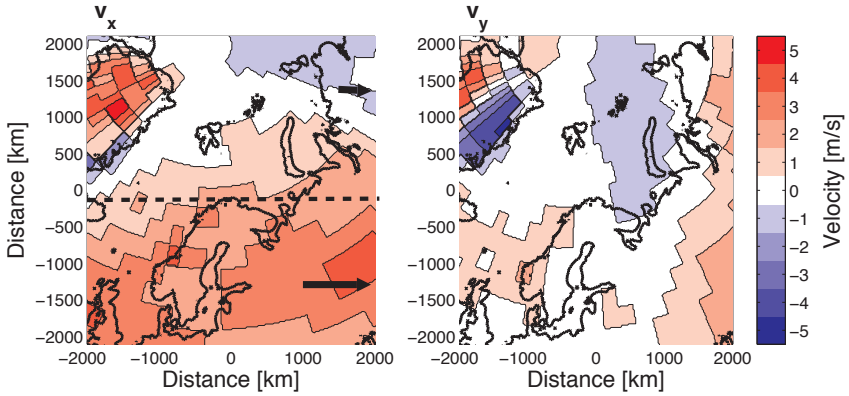

Figure 5.3: Wind field for present day conditions from HADCM3M2 interpolated in the Cartesian model domain. The left plot shows v_x and the right plot shows v_y, where the x and y axes coincide with the horizontal and vertical plot boundaries respectively. The black arrows and dashed line show the parameterized wind field as used in this paper with (v_x, v_y)=(3,0) m/s in the bottom half of the domain, and (v_x, v_y)=(0.5,0) m/s in the top half of the domain.

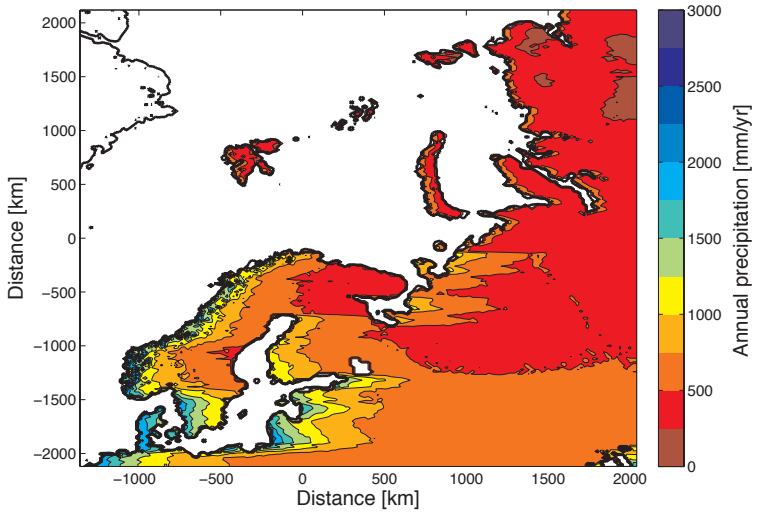

Figure 5.4: Annual precipitation in mm/yr according to model.

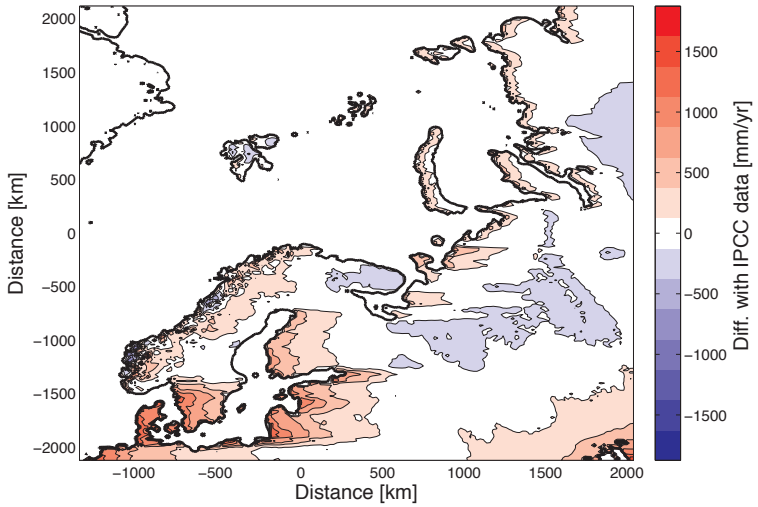

Figure 5.5: Differences in precipitation (mm/yr) between IPCC data and model results for optimum combination of parameters.

The melt is calculated from monthly temperatures using a parameterization that contains a direct temperature and insolation effect (e.g. Pollard, 1980; Oerlemans, 2001):

$$M = \Delta t * [\tau\,(1-\alpha)\,Q + c + 10\,T]\,/(1000\,L_m), \tag{5.4}$$

where M is the monthly melt in meters water equivalent, Δt is the number of seconds in a month, τ is the total transmissivity of the atmosphere, taken here as 0.5, $c + 10\,T$ is the sum of the longwave radiation and turbulent exchange, T is the surface temperature in degrees Celsius, Q is the monthly insolation at the top of the atmosphere in W/m^2, which is adjusted every 1000 years, and L_m is the latent heat of melt (Table 5.1). When calibrating the model on Nigardsbreen a value for c of about -10 was found. Comparing modelling results with geomorphological evidence on ice extent resulted in an optimum value for c of -117 for our set of parameters and ice flow model. The large difference with the value found at Nigardsbreen is mostly due to the coarser resolution of the topography and the ice flow model, but also due to the difference in input temperatures and the fact that in this study it is used as a tuning parameter to compensate for other processes that are not accounted for.

The albedo is calculated as (Bintanja et al., 2002)

$$\alpha = \min\left(\alpha_g + 10\,(\alpha_s - \alpha_g)\,d, \alpha_s\right), \tag{5.5}$$

where α_g is the ground albedo (0.2 for a bare surface, 0.45 for ice), α_s is the albedo for snow (0.8) and d is the snow depth in meters water equivalent. The snow depth varies throughout the year based on the cumulative monthly mass balance, but is limited to 10 meters.

5.4 A synthetic example

To illustrate the effect of the mass balance formulation on ice sheet evolution we show the results of a synthetic example. We coupled the mass balance model to the ”type 2” (e.g. Huybrechts et al., 1996) vertically integrated shallow ice approximation model as presented in Van den Berg et al. (2006a). We neglected the effects of thermodynamics by keeping the flow parameters constant through time and throughout the ice sheet. We included a simple sliding parameterization based on a Weertman type sliding law. Ice shelves were calculated using an empirical parameterization (Oerlemans and van der Veen, 1984; Bintanja et al., 2002). To calculate the isostatic response, we used a flexural model with a rigidity $D = 10^{25}$Nm and a single relaxation time of 3000 years, values commonly used in glaciological applications. Oceans were assumed to be covered by sea ice when monthly temperatures were below -1.7^{o}C.

We prescribe an initial topography as a ridge of 1500 meters height and 300 kilometers wide (Figure 5.6), a wind field of 3 m/s from left to right and a constant temperature at zero meters altitude. We used a constant insolation of 236.6 W/m^2, which is the average present day value for 60^{o}N. Since the temperature and insolation are constant, the precipitation is also evenly distributed over the year. There is no ocean in this concept, just initial bare earth.

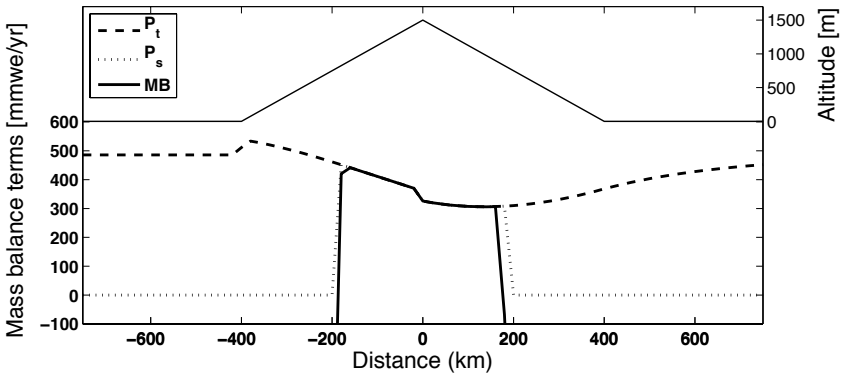

Figure 5.6: Mass balance (MB), solid precipitation (P_s) and total precipitation (P_t) for the initial geometry as shown by the thin solid line above the mass balance terms and a wind field of 3 m/s from left to right.

Figure 5.6 shows the total precipitation, solid precipitation and total mass balance profile for this initial situation. At low elevations, all precipitation falls as rain and the melt is large, making the mass balance negative (off scale). For higher elevations the snow fraction increases and the melt decreases. At the highest elevations there is no melt and mass balance, solid precipitation and total precipitation are equal.

The orographic effect enhances precipitation where the slope faces the wind. The effect of advection of moisture is small in this example, due to absence of ocean nearby, but still contributes to the asymmetry in precipitation over the ridge. The asymmetric precipitation results in an asymmetric mass balance profile.

For this situation a steady state ice sheet develops. Figure 5.7 shows a cross section of the final ice sheet together with the mass balance, solid precipitation and total precipitation. Clearly, the asymmetric pattern in the initial mass balance profile generates an asymmetric ice sheet. Because the ice sheet margin is steeper than the original topography, the orographically induced enhancement of the precipitation increases. This results in an increasing asymmetry in the mass balance. The more the ice sheet grows, the further to the left in the domain the maximum in mass balance occurs. Hence, the ice sheet grows ”against” the wind. The larger the left part of the ice sheet, the less moisture is advected to the right part. There is little evaporation over the ice itself. Without advection of moist air and with little in situ evaporation the right part of the ice sheet is very dry. This makes it difficult for this part of the ice sheet to expand.

When we compare the total precipitation in the right part of the domain at the same altitude in Figures 5.6 and 5.7, we observe that the values in the steady state situation are about half of the values of the initial state. This illustrates that ice sheets reduce the precipitation when they grow. This is a combined effect of less in situ evaporation and increasing distance from moisture sources.

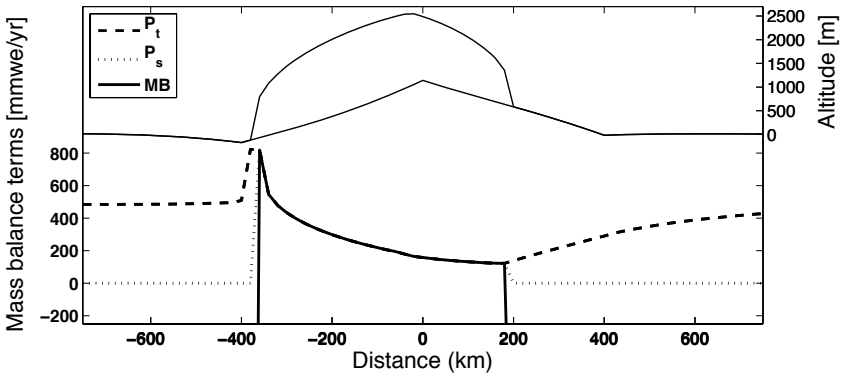

Figure 5.7: Mass balance (MB), solid precipitation (P_s) and total precipitation (P_t) for the steady state ice geometry as shown by the thin solid line above the mass balance terms and a wind field of 3 m/s from left to right.

A similar experiment was performed with a nearby ocean on the left side of the domain (sea level was set to 0 meters altitude throughout the experiment). An ocean has more evaporation than bare earth, so the amount of moisture available for advection towards the ridge increases. More moisture means more precipitation, which in turn increases the mass balance. Figure 5.8 shows the resulting steady state ice sheet together with the mass balance, solid precipitation and total precipitation. Since there is more moisture available the ice sheet grows faster. Also, more moisture is available for advection of humid air over the ice divide. This increases the right part of the ice sheet. However, even in this case, advection of moisture only has a limited range. Moreover, as the ice sheet grows it becomes increasingly difficult to transport moisture over the cold, high ice sheet. The left part of the ice sheet is actually smaller than in Figure 5.7, because the ice cannot grow far into the ocean. Thus, the total size of the ice sheet is controlled by the advection of humid air and by the ocean itself as limiting factor for the ice extent.

To summarize, the model captures the following key processes; firstly, control on dimensions of the ice sheet through the advection of moisture. Secondly, the asymmetric behaviour as a result of wind and orography. This is caused both by advection of humid air and the saturation of rising air. Thirdly, the drying of ice sheets as they grow due to higher elevations, less evaporation and increasing distance from moisture sources. These are the main processes generally believed to be governing large ice sheets such as the Eurasian Ice Sheet.

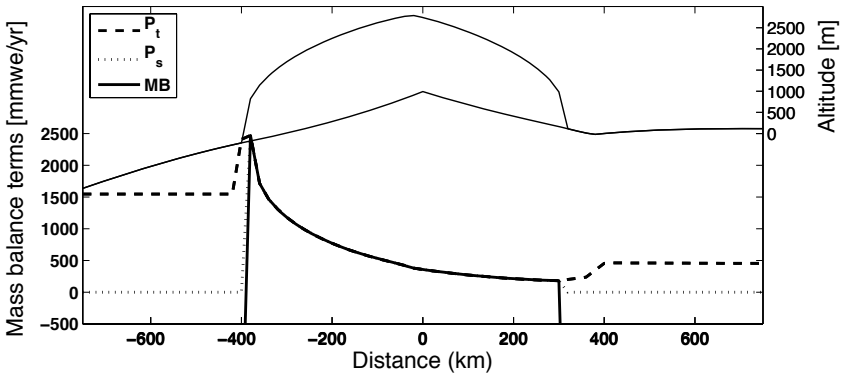

Figure 5.8: Mass balance (MB), solid precipitation (P_s) and total precipitation (P_t) for the steady state ice geometry for the synthetic experiment with an ocean on the left of the domain as shown by the thin solid line above the mass balance terms and a wind field of 3 m/s from left to right.

5.5 An application to Eurasia

In this section we discuss the results of a full glacial cycle over the last 120,000 years for the Eurasia Ice Sheet. Sea level was prescribed as a global eustatic adjustment. We compare these results to a recent data compilation as presented by the QUEEN program (Svendsen et al., 2004). There, the Eurasian ice history of the last 120,000 years is separated in three distinct time periods; (i) the Early Weichselian with a maximum ice extent between 100 and 80 kyr BP, (ii) the Middle Weichselian glaciation with a maximum ice extent between 60 and 50 kyr BP and (iii) the Late Weichselian culminating in the LGM between 25 and 10 kyr BP. In between those periods the QUEEN results indicate that the region remained largely ice free. We will discuss our results with respect to those periods. First we will briefly summarize the main conclusions of the QUEEN program with emphasis on aspects important for ice sheet modelling.

5.5.1 The QUEEN results

The QUEEN compilation is primarily based on geomorphological data complemented with the results of a dynamical ice flow model where data were sparse or absent (Siegert et al., 2001; Svendsen et al., 2004). This dynamical ice flow model was tuned to fit the available data as well as possible. The QUEEN results basically state that during the Early Weichselian there was a large ice sheet in the Barents and Kara Seas, whereas the ice cover in Scandinavia remained limited mostly to Norway and parts of Sweden. During the Middle Weichselian, the ice sheet over the Barents and Kara Seas was again large. The ice sheet over Scandinavia increased from the Norwegian and Swedish mountains to cover

the entire Baltic area and Finland. Then, in the Late Weichselian the ice sheet over the Arctic Seas and Islands only covered the Barents Sea. Thus, the Kara Sea was probably at least partially ice free. The Scandinavian ice sheet grew huge to cover the Baltic states, parts of the Russian plains and even the North Sea and the British Isles. Hence, in general the Arctic Seas and Scandinavia had opposing trends with an early, fast growth in the Barents and Kara Seas and a late, slow growth in the Scandinavian area. The ice sheet covering Scandinavia started relatively small growing towards a maximum around LGM. The ice sheet covering the Barents and Kara Seas grew very large in roughly 30,000 years to subsequently reach smaller and smaller sizes in the later periods.

5.5.2 Modelling results for the Early Weichselian: 100-80 kyr BP

Figure 5.9 shows ice volume as a function of time. It also shows ice thickness, the mass balance and the bedrock deformation at 86 kyr BP. Figure 5.9 shows an ice centre over the north of Scandinavia with limited ice in Sweden and Finland. A large, thin ice sheet covers the Kara Sea and the southwestern Barents Sea with the Arctic islands and the coast of Russia and Siberia as nucleation centres. The Polar Ural has little ice. This ice-covered region corresponds to the region with positive mass balance. The bedrock deformation shows a very smooth pattern from which the division into two distinct ice domes is clearly visible.

Interesting is the development of ice patches with thin ice south of the main ice sheet. These patches do not contribute to the bedrock deformation, because they are either too small or too recent. The ice is so thin that if the mass balance would turn negative, the patches would melt rapidly. Therefore, these patches are an indication of the transient state of the ice sheet.

Figure 5.10 shows a cross-section, as shown in Figure 5.9 by the white line in the mass balance figure, through southern Svalbard, Novaya Zemlya and the western part of the Kara Sea of the ice sheet topography, mass balance, solid precipitation and total precipitation. The ice sheet on the western side of Svalbard grew until it reached the edge of the continental slope. This situation closely resembles the synthetic example in Figure 5.8. The orographically induced asymmetry is clearly visible for Novaya Zemlya, but not for the ice sheet over the Kara Sea. This latter ice sheet started on the Siberian coast and has migrated toward the sea. This process has removed the asymmetries. The entire Barents Sea region has virtually no melt, but is also very dry because of the low temperatures. This means the mass influx from the Arctic islands into the Barents Sea is limited which causes the sea to be free of land based ice.

The calculated ice distribution as shown in Figure 5.9 compares well with the data presented by the QUEEN program (Svendsen et al., 2004). The approximate ice limits, as stated by the QUEEN report, are shown in the ice thickness plot in Figure 5.9 by the thick dashed red line. The major exception is the northwestern Barents Sea, but this is a region with few data where the ice limits in the QUEEN report were mainly drawn using results from modelling studies (Siegert et al., 2001; Svendsen et al., 2004). According to others, (e.g. Velichko et al., 1997), a more limited ice cover in that region is not unrealistic.

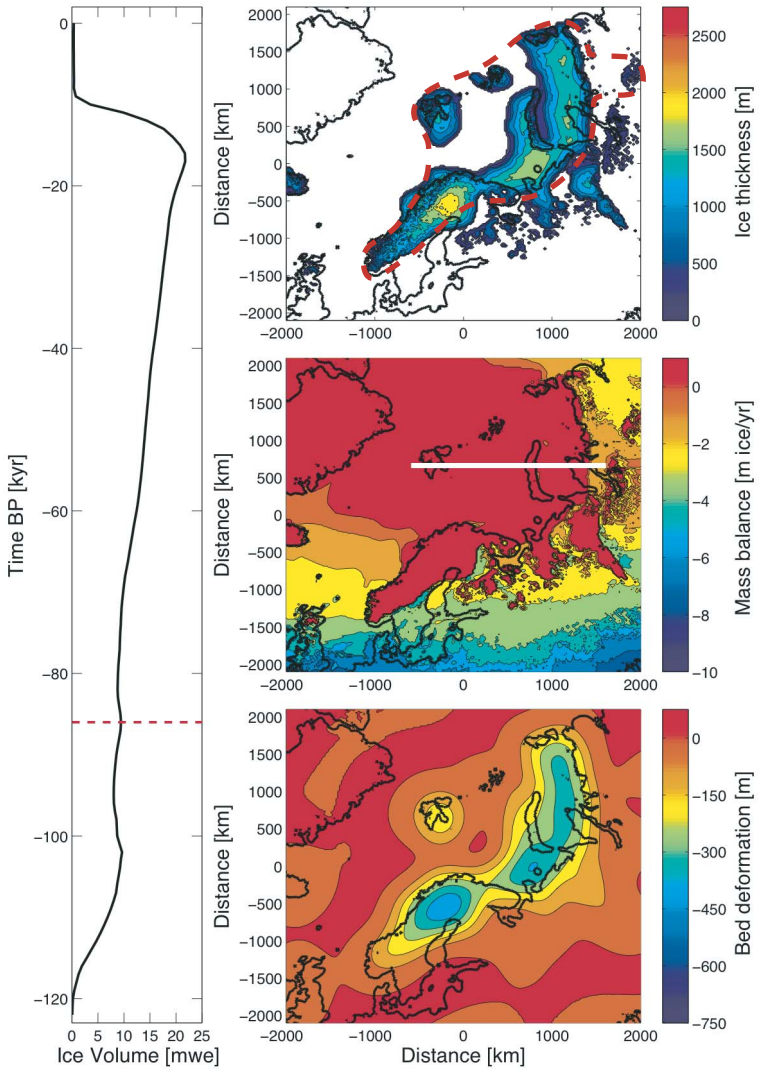

Figure 5.9: On the left is the modelled ice volume as a function of time, the red, dashed line shows the time 86,000 BP. For this time, modelled ice thickness, mass balance and bedrock deformation are shown on the right. The white line in the mass balance figure shows the location of a cross-section as shown in Figure 5.10. The red dashed line in the ice thickness plot shows the approximate imits in ice extent as predicted by the QUEEN compilation.

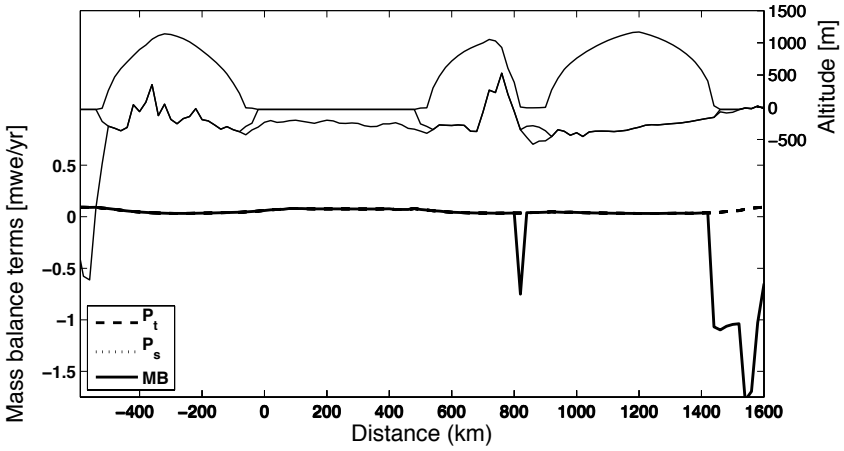

Figure 5.10: Modelled mass balance (MB), solid precipitation (P_s) and total precipitation (P_t) at time 86,000 BP for a cross-section through southern Svalbard, Novaya Zemlya and the southern Kara Sea. The modelled ice sheet topography (thin solid lines) is shown above the mass balance terms.

5.5.3 Modelling results for the Middle Weichselian: 60-50 kyr BP

Figure 5.11 shows ice volume as a function of time as well as the ice thickness, the mass balance and the bedrock deformation at 55 kyr BP. Whereas the QUEEN results (Svendsen et al., 2004) predict a new maximum around this time, it is immediately clear from the ice volume curve that the model predicts, with local exceptions, a continuous buildup of ice towards LGM. The variations in temperature forcing, Figure 5.2, are either too small or too fast compared to the time scales of the ice-dynamical processes to induce large, rapid volume changes.

The previously observed patches of thin ice in Figure 5.9 are thickening into proper ice domes in Finland and the Russian plains. Also, the Polar Ural starts to serve as an ice centre. The region of positive mass balance is extending towards the south compared to the Early Weichselian. This is in agreement with the QUEEN data. According to the QUEEN data the Scandinavian ice sheet should by now reach Denmark and the Baltic states in contrast with the ice sheet over the Arctic Seas which should decrease a little. The ice sheet model produces a much more limited ice growth in Scandinavia and a stable, slightly thickening ice sheet over the Barents and Kara Sea.

Figure 5.12 shows a cross-section, as shown in Figure 5.11 by the white line in the mass balance figure, of the topography, mass balance, solid precipitation and total precipitation through southern Norway and Sweden across the Baltic area. The wind and orography create an asymmetry in mass balance over the Norwegian ice sheet similar to the synthetic example in Figure 5.8. The temperature is on average about 11 degrees lower

than today. The summer temperatures however may still be above zero and with a summer insolation of about 450 W/m^2 the modelled ablation is with 3 m/yr still substantial. Compared to present day mass balance on the Arctic islands, the modelled ablation is not unrealistic. The western part of the Norwegian ice sheet blocks the moisture advection to the east. As a result, this region is too dry to overcome the amount of melt.

5.5.4 Modelling results for the Late Weichselian: 25-10 kyr BP

The maximum ice volume is found around 17 kyr BP as shown in Figure 5.13. This is in agreement with the QUEEN data. Again, we see patches of thin ice south of the main ice sheet. In the bedrock deformation it is clear that the patches do not contribute to the deformation pattern. The patches indicate that at LGM the ice sheet was not in balance, but would continue to grow if the temperatures would remain low. The region of positive mass balance has extended even further south compared to the Middle and Early Weichselian. The total ice volume is approximately 22 meters sea level equivalent, which is roughly in agreement with the QUEEN data.

As expected from the results in the Middle Weichselian, the ice sheet remains too large in the Barents and Kara Sea, and the ice does not reach its southern limit in the Scandinavian area.

Around present day, most of the ice has disappeared except for some ice over Svalbard, Franz Josef Land and the Norwegian mountains. The ice in Norway is too thick, but the fact that some ice remains is not unrealistic given the presence of numerous glaciers in the region.

5.6 Sensitivity tests

In this section we discuss the results of some elementary sensitivity tests for two parameters; the temperature and the wind field. We show three tests: (I) the temperature perturbation is multiplied by 1.2, hence 20 $\%$ uncertainty, (II) the lapse rate is -5^{o}km^{-1} when the slope-term ($\mathbf{v}\cdot\nabla h_s$) is larger than zero, -8^{o}km^{-1} when the slope-term is smaller than zero and -6.5^{o}km^{-1} when the slope-term is equal to zero to account for changes in the lapse rate as a result from interaction between the windfield and the surface slope, i.e. föhn effect. Finally, (III) instead of the simple parameterization for the windfield, the interpolated present day windfield from HADCM3M2 is used, Figure 5.3.

Figure 5.14 shows the resulting volume curves, where the reference situation is the glacial run from the previous section. Clearly, the uncertainty in the temperature perturbation (I) has the highest impact with a volume change of about 50$\%$ for a 20$\%$ increase in perturbation, followed by a change in the wind field (III) with a volume change of about 40$\%$. The local value of the lapse rate does not seem to be very important.

Figure 5.15 shows for case (I) and (III) the resulting difference in ice thickness for LGM. In both cases we see that there is a tendency for more ice in the Baltic area. Especially case (I) allows the ice to grow far more to the south. Both cases also show more ice on the Siberian coast, which is not in agreement with the data (Svendsen et al., 2004).

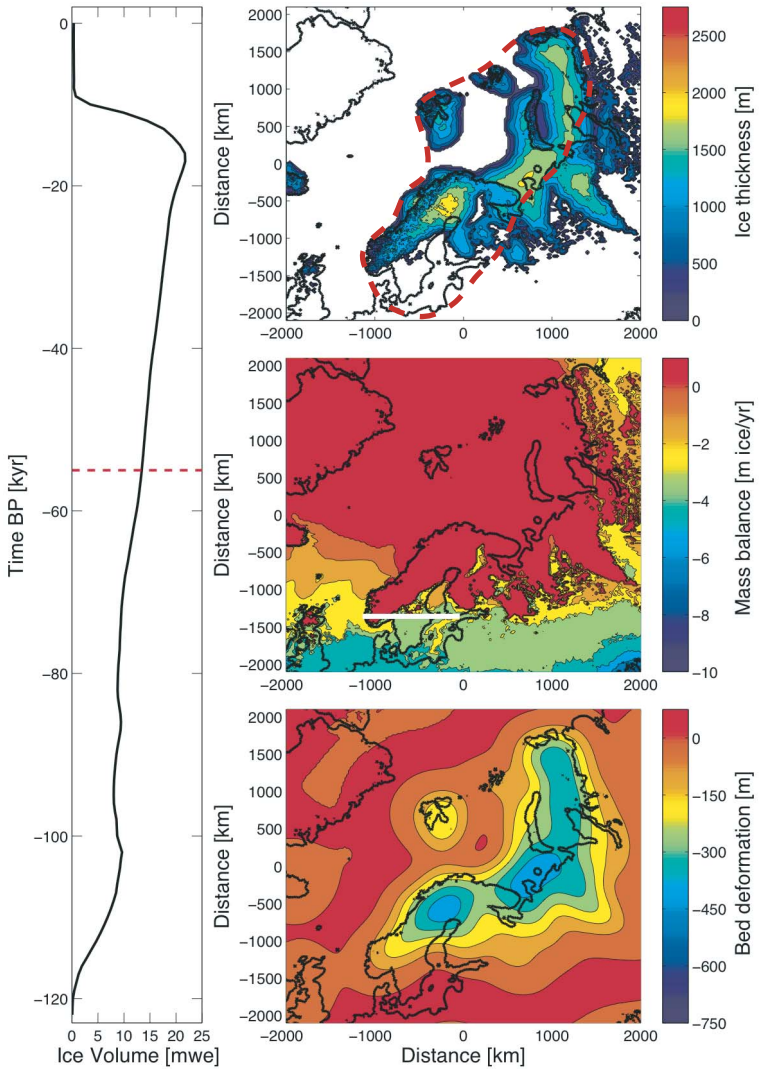

Figure 5.11: On the left is the modelled ice volume as a function of time, the red, dashed line shows the time 55,000 BP. For this time, modelled ice thickness, mass balance and bedrock deformation are shown on the right. The white line in the mass balance figure shows the location of a cross-section as shown in Figure 5.12. The red dashed line in the ice thickness plot shows the approximate imits in ice extent as predicted by the QUEEN compilation.

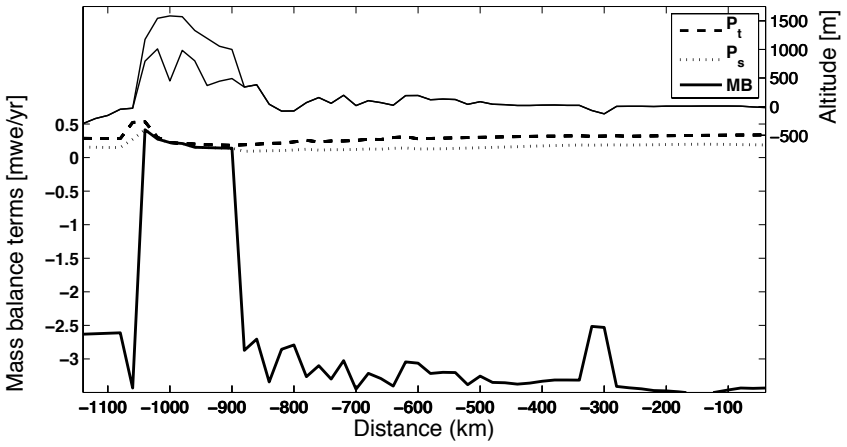

Figure 5.12: Modelled mass balance (MB), solid precipitation (P_s) and total precipitation (P_t) at time 55,000 BP for a cross-section through southern Norway, Sweden and the Baltic area. Modelled ice sheet topography is shown above the mass balance terms .

Case (I) shows less ice in the Barents and Kara Seas region compared to the reference case. The air over this region is so cold that there is hardly any moisture available for precipitation. Clearly, it is important to know the local temperature perturbation as a function of time. Coincidentally, the simple wind field parameterization results in a better overall ice distribution around LGM than the fully interpolated present day wind field. This illustrates the problem of knowing a detailed wind field, not just for present day conditions but as a function of time.

5.7 Conclusions

Instead of prescribing precipitation as a perturbed field throughout a glacial cycle, we introduced a mass balance model which calculates precipitation as a function of temperature, wind and altitude. Hence, the precipitation is dynamically coupled to the evolving ice sheet. The model is tuned to present day conditions only, and is otherwise allowed to evolve freely with the ice sheet. Key processes the model captures are (i) the control of advection of moisture on the dimensions of an ice sheet, (ii) asymmetric mass balance profiles and resulting ice sheets due to orography and wind, and (iii) drying of ice sheets as they grow.

We used 500 hPa temperatures from the model HADCM3M2 in the PMIP2 experiments instead of surface temperatures to calculate temperature perturbations throughout an ice age. These temperatures are better representative for precipitation and less sensitive to the surface properties in a GCM. This means that they represent a more robust measure

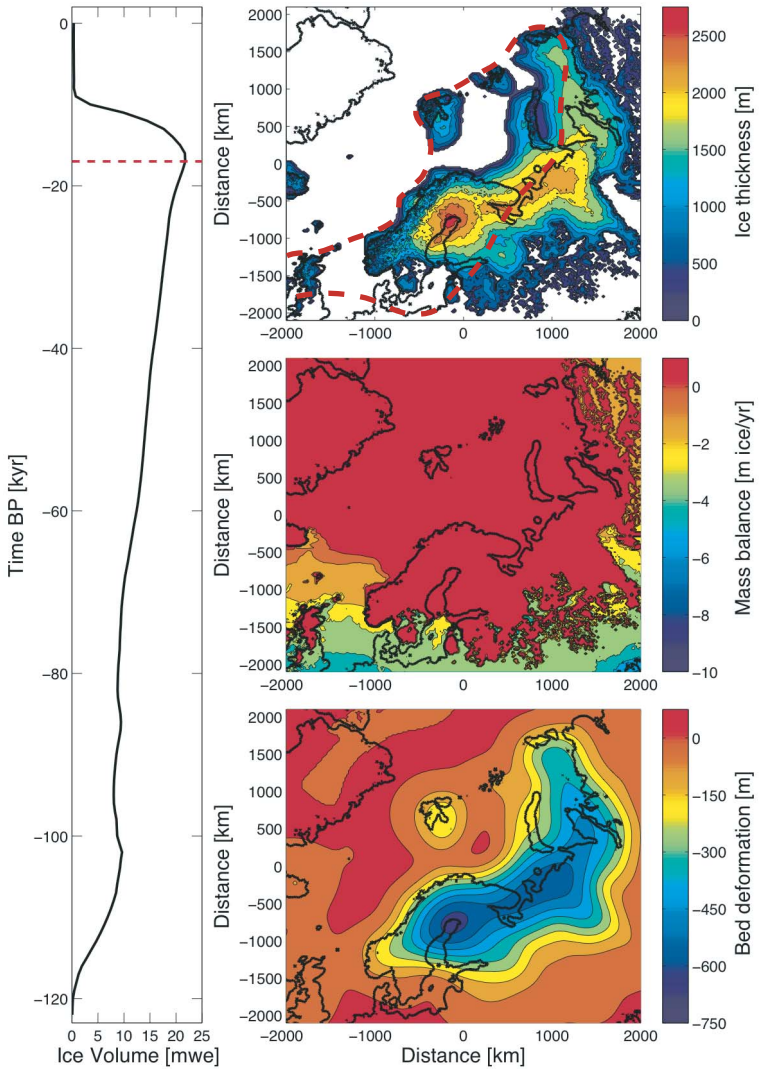

Figure 5.13: On the left is the ice volume as a function of time, the red, dashed line shows the time 17,000 BP. For this time, modelled ice thickness, mass balance and bedrock deformation are shown on the right. The red dashed line in the ice thickness plot shows the approximate imits in ice extent as predicted by the QUEEN compilation.

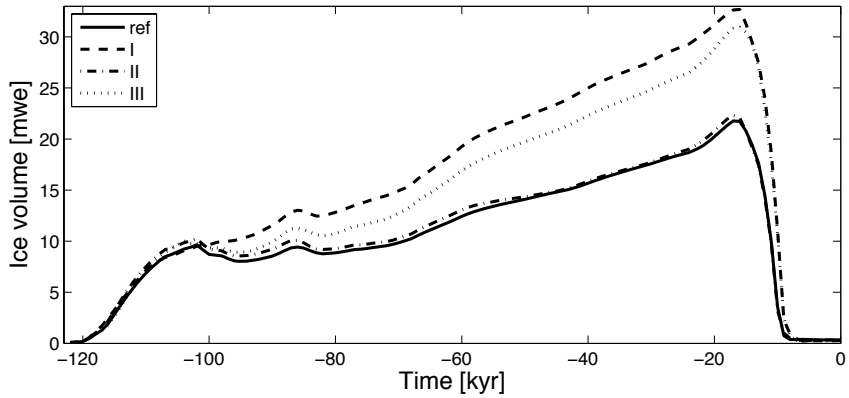

Figure 5.14: Ice volume as a function of time for the reference situation (solid line) and the three sensitivity tests for (I) temperature, (II) föhn effect, and (III) wind field, as further explained in the main text.

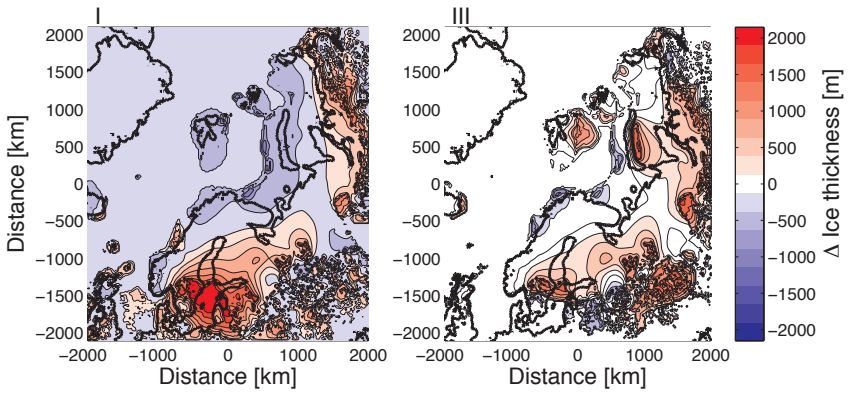

Figure 5.15: Difference in ice thickness between sensitivity tests I and III and the reference situation for LGM (Ice thickness$_{I,III}$-Ice thickness$_{ref}$).

of temperature change than surface temperatures.

We showed a full glacial cycle over the last 120,000 years for Eurasia. The model results compare well with a recent data compilation as performed during the QUEEN program (Svendsen et al. (2004)) for the Early Weichselian. During the Middle Weichselian and the Late Weichselian, the model picks up the trend that the Scandinavian part of the ice grows toward the south and east whilst the ice sheet covering the Barents and Kara Seas remains relatively stable. However, the model seriously underestimates the observed ice extent in the Baltic area. The modelling results show the occurrence of patchy regions of thin ice during several time slices including LGM, which tend to correspond to regions with many small variations in altitude. These patches are signs of imbalance of the ice sheet and indicate the ice sheet would continue to grow if temperatures would remain low.

We showed sensitivity tests for two highly uncertain and important parameters: (i) the temperature and (ii) the wind field. We used a perturbation valid for the region 60^oN to 80^oN, but local perturbations may be different. Uncertainties of the temperature perturbation of 20% resulted in an increase of the ice volume with approximately 50% at LGM. It caused the ice sheet to expand more to the south, but also influenced the ice thickness in the north. Hence, the resolution of the temperature perturbation record limits the reliability of regional modelling results.

Tests with the wind field showed a large sensitivity of the modelling results to the direction of the wind. The wind field is one of the most poorly known parameters as a function of time. It is likely that during an ice age the wind field is different from the present day situation. How the wind field changes depends amongst other reasons on the ice sheet geometry. Due to the lack of sensible alternatives we used a simple parameterization roughly based on the present day situation. However, it is clear that lack of knowledge on a changing wind field also limits the reliability of regional modelling results without a full coupling of a GCM to the ice flow model.

For a model of such simplicity the results are encouraging. We feel that the presented mass balance model is a worthwhile contribution to the set of mass balance models available, since it is very different from currently used parameterizations and has a fully coupled mass balance-ice sheet configuration scheme. Yet it is able to simulate realistic ice sheets. Moreover, it gains insight into the physical processes governing the development of ice sheets.

5.8 Acknowledgments

We acknowledge the international modeling groups for providing their GCM results for analysis, the Laboratoire des Sciences du Climat et de l'Environnement (LSCE) for collecting and archiving the model data. The PMIP2/MOTIF Data Archive is supported by CEA, CNRS, the EU project MOTIF (EVK2-CT-2002-00153) and the Programme National d'Etude de la Dynamique du Climat (PNEDC). More information is available on http://www-lsce.cea.fr/pmip2/. The calculations in this paper were performed on the RADON cluster of IMAU, which was partly funded by the Utrecht Center of Geosciences.

This work was financed by the Spinoza Award of NWO of Professor J. Oerlemans.

Chapter 6

The effect of isostasy on dynamical ice sheet modelling; a case study for Eurasia

Isostatic adjustment is an important process when modelling dynamical ice sheet evolution. A number of different types of earth model are used to model this isostatic response ranging from local or elastic lithospheres with a single relaxation time to account for temporal behaviour to spherically symmetric models of the crust-mantle system. We performed sensitivity tests to assess the dynamical response of ice sheets to isostatic adjustment. The resulting ice sheet geometries depend on the response times of the system, including the growth rate of ice sheets versus the relaxation time of the earth. Differences in lithospheric strength cause large differences in the modelled ice sheets, with the largest differences in isostatic adjustment in the vicinity of the ice margin. In addition, we compared predictions based on an often used flexural model with an elastic plate and a single relaxation time to a spherically symmetric self-gravitating viscoelastic approach. No flexural model was able to reproduce the viscoelastic response completely, due to the fact that the models have an intrinsically different spatial and temporal response. When applied to a full transient glacial cycle in Eurasia even the best fitting flexural model underestimated the ice volume at the LGM by 30 percent. Our results indicate that the commonly used value of 3000 years for the relaxation time in flexural models is too short for Eurasia by at least 3000 years.

6.1 Introduction

Isostatic depression of the solid earth as a result of ice loading can reach amplitudes of about one third of the ice thickness, and so crustal subsidence of up to one kilometer

This chapter has been submitted by to *Journal of Geophysical Research: Solid Earth*.

is common for large ice sheets. Since precipitation and melt both depend on surface elevation, it is clear that an accurate treatment of the isostatic response of the solid earth is important. In addition, the isostatic adjustment of the earth affects changes in relative sea level and so will influence the amount of calving and grounding line mechanics. Several studies have suggested isostatic adjustment as an internal feedback mechanism to generate the 100,000 year cycle evident in observational records (e.g. Oerlemans, 1980; Ghil and Le Treut, 1981; Le Treut and Ghil, 1983; Tarasov and Peltier, 1997). This is related to the nonlinear interaction between the different time-scales associated with isostatic adjustment and ice sheet response to climate changes.

Crucifix and others (2001) performed experiments with a local isostatic adjustment model, and demonstrated that isostatic adjustment always induces a negative feedback on ice volume change. For example, for an advancing ice sheet isostasy reduces the growth. For a retreating ice sheet however, isostatic rebound results in less melt. According to these results, lower elevations suggest higher temperatures, hence more melt. Based on this rationale, an increase in the relaxation time acts to reduce the degree of negative feedback. However, contrary to the results of Crucifix and others (2001), we think that if the subsidence is slower than the ice sheet growth rate, the ice sheet may be able to raise the surface elevation as the bedrock subsides. The ice sheet then "fills the isostatic gap" without moving to lower elevations. In this case the resulting ice sheet would be larger than without isostatic adjustment. So, the earth response may act as a positive or negative feedback mechanism depending on the response times in the coupled system, which amongst others depend on size of the ice sheet, geographical geometry and mass balance.

Le Meur and Huybrechts (1996) compared a number of earth models having a local or an elastic lithosphere and a single relaxation time (called LLRA and ELRA respectively) to a physically more realistic spherically symmetric self-gravitating viscoelastic earth model (SGVE) (Longman, 1963; Farrell, 1972; Peltier, 1974; Cathles, 1975; Wu and Peltier, 1982). (In the following, we adopt the same abbreviation as Le Meur and Huybrechts for the two earth models, ELRA and SGVE.) They showed that for the last glacial-interglacial transition in Antarctica, the ELRA model agreed well with the physically more realistic SGVE model. They concluded that the ELRA model with a flexural rigidity of $D = 10^{25}$Nm and a relaxation time $\tau = 3000$ years was a reasonable alternative to the computationally more demanding SGVE model. As a result, this ELRA model is now the most commonly used earth model in ice sheet modelling (e.g. Le Meur and Huybrechts, 1996; Fabre et al., 1997; Forsström and Greve, 2004; Charbit et al., 2002; Zweck and Huybrechts, 2003; Huybrechts et al., 2004; Siegert et al., 2001; Zweck and Huybrechts, 2005).

In this study, we extend upon the above described work in several respects. While Crucifix and others (2001) coupled a zonally averaged quasi-geostrophic model to a surface energy balance model to calculate mass balance, we used a mass balance model based on the conservation of moisture, and includes physical processes as advection of humid air, orographically induced precipitation and drying of the ice sheets as they grow (e.g. Sanberg and Oerlemans, 1983; Van den Berg et al., 2006b). This mass balance has a more realistic feedback with elevation and surface slope, both in the melt and the precipitation

patterns, and may therefore have an increased sensitivity to differences in earth models. Moreover, the mass balance is calculated on the same resolution as the ice model instead of being a zonal average, allowing for more detail. With an earth model consisting of an elastic lithosphere and a single relaxation time to account for temporal behaviour (ELRA) (e.g. Brotchie and Silvester, 1969; Watts, 2001; Turcotte and Schubert, 2002), we show that the feedback of isostatic adjustment on ice sheet growth is not always negative and depends on the strength or effective flexural rigidity of the lithosphere, this in contrast with the results of Crucifix and others (2001).

The comparison of earth models in Le Meur and Huybrechts (1996) was only conducted for a study in Antarctica with a focus on present day uplift patterns. The geometry of the Antarctic Ice Sheet is not representative for all large ice sheets that existed during the Quaternary. At present the Antarctic Ice Sheet covers practically the entire continent and has virtually no ablation zone. During glacial periods the expansion is controlled mainly by grounding line migration and thickening of the ice sheet in the areas where we now find the major ice shelves. In contrast, the Laurentide Ice Sheet formed for a large part on land, and as such is controlled more by ice deformation, ablation and sliding. The Eurasian Ice Sheet partly formed on land, but also in shallow seas. As such, the conclusion that the ELRA model is a reasonable alternative to the SGVE model is not necessarily valid for the major northern hemisphere ice sheets.

We compare a self-gravitating viscoelastic model (SGVE) with a flexural model (ELRA) for a wide range of effective flexural rigidities and relaxation times, focussed on an application to the entire Eurasian Ice Sheet history over the last 120,000 years. We chose to focus on the Eurasian Ice Sheet because it is fundamentally different to the Antarctic Ice Sheet and is representative of the Late Quaternary northern hemisphere ice sheets. Furthermore, the isostatic response of this region has been studied extensively and so relatively good constraints on the sub-surface earth structure are available. The results of this study provide an indication on the global applicability of the results of Le Meur and Huybrechts (1996).

Besides the issue of the global applicability of the ELRA model, both the value for the effective flexural rigidity and the relaxation time have considerable uncertainty. Le Meur and Huybrechts (1996) used only a limited number of relaxation times, and only a single value for the effective flexural rigidity in their study. Many studies in North America and Eurasia have have inferred values for the effective flexural rigidity ranging from $D = 10^{22}$Nm, for oceanic lithosphere, to $D = 10^{25}$Nm, for cratonic lithosphere (e.g. Walcott, 1970a,b; Fjeldskaar, 1997; Poudjom Djomani et al., 1999; Braitenberg et al., 2002; Audet and Marechal, 2004; Pérez-Gussinye and Watts, 2005). Uplift curves based on sea-level indicators from North America have indicated values for the relaxation time τ between 1500 and 3000 years (e.g. Andrews, 1968; Brotchie and Silvester, 1969). These were based on simple assumptions for the ice decay. Recent studies in Scandinavia based on uplift curves and strand line data suggested a value of 5000 plus or minus 1000 years (e.g. Mitrovica and Forte, 1997; Wieczerkowski et al., 1999; Mitrovica and Forte, 2004). Given the plausible range in these parameter values, we therefore compared the ELRA and SGVE earth models for a wide range of relaxation times and flexural rigidities.

6.2 Model formulation

6.2.1 Ice flow model

The ice flow model is based on the vertically integrated continuity equation (e.g. Van der Veen, 1999):

$$\frac{\partial H}{\partial t} = -\nabla \cdot (H\,\mathbf{U}) + B, \tag{6.1}$$

where H is the ice thickness, $\mathbf{U}$ is the vertically averaged horizontal velocity, and B is the mass balance, which is the net increase or decrease of local ice thickness in meters of ice per unit time due to snow fall or ice melt at the surface of the ice sheet. We used the shallow ice approximation (e.g. Hutter, 1983; Van der Veen, 1999), which assumes that the horizontal extent is much larger than the ice thickness. For a two-dimensional model the expression for the vertical mean horizontal velocity is given by

$$\mathbf{U} = \mathbf{U_S} - \frac{2}{n+2}\,(\rho_i\,g)^n\,A\left[\frac{\partial h_s}{\partial x}^2 + \frac{\partial h_s}{\partial y}^2\right]^{\frac{n-1}{2}} \nabla h_s\,H^{n+1}, \tag{6.2}$$

where h_s is the surface height, ρ_i is the ice density, g the gravitational acceleration, and A and n are rheological parameters, where n is set to 3. The parameter A is assumed to be constant throughout the ice. For the sliding velocity $\mathbf{U_S}$ a Weertman type sliding law is used (e.g. Van der Veen, 1999). Explicit calculation of the thermodynamics is neglected and sliding is restricted to areas with a negative mass balance.

The model corresponds to the type II ice models from the EISMINT experiments (Huybrechts et al., 1996), which is widely used by ice sheet modelers. For the time integration an Alternating Direction Implicit (ADI) method is used (e.g. Mahaffy, 1976; Huybrechts, 1992). The ice thickness at all boundaries is set to zero.

The ice flow model has an empirical parameterization for ice shelf formation based on distance to the grounding line and water depth (e.g. Oerlemans and van der Veen, 1984; Bintanja et al., 2002). The model is forced by temperature, solar insolation and eustatic sea level. The temperature perturbation with respect to present day conditions was derived by Bintanja and others (2005).

6.2.2 Description of the mass balance

We use a mass balance description based on the principle of moisture conservation. A detailed explanation of the model can be found in Van den Berg and others (2006b). The precipitation is calculated from the following equation for the conservation of moisture (Sanberg and Oerlemans, 1983):

$$\frac{\partial W}{\partial t} = -\mathbf{v} \cdot \nabla W - (f_0 + f_1 S)\,W + (W_m - W)\,/t^*. \tag{6.3}$$

In this equation W is the amount of water vapour in an atmospheric column extending from the surface to the top of the atmosphere. The first term on the righthand side describes the advection of moist air by a horizontal wind field $\mathbf{v}$. The second term is the

precipitation, which consists of two parts. The first part of the precipitation is the background precipitation governed by the constant f_0, the second part represents precipitation that forms when air is forced upslope and saturation occurs. This process is governed by the constant f_1 and a slope term S ($S = max(0, \mathbf{v} \cdot \nabla h_s)$), where h_s is the surface altitude. The last term on the righthand side is the evaporation, which is a function of a characteristic time scale t^* and the maximum amount of water vapour W_m. The evaporation is very important since it is the only source term in equation (6.3). The maximum amount of water vapour in a column of air has a strong dependency on temperature and altitude, and is approximated using an integrated Clausius-Clapeyron curve (Paul, 1996).

For a given annually averaged temperature field, topography, and wind field, a steady state W can be found by numerically evaluating equation (6.3). This precipitation model was tuned for conditions in Eurasia. Once a steady state W has been calculated, the monthly solid precipitation can be estimated. The distribution of total precipitation throughout the year as calculated by HADCM3M2 in the PMIP2 experiments (http://www-lsce.cea.fr/pmip2/) determines the monthly total precipitation. Finally, the monthly temperature determines if precipitation falls as snow or rain. The seasonal temperature variation with respect to the annual average temperature is equal to the present day seasonal variation as calculated by HADCM3M2. The yearly average temperature can be adjusted as a function of time.

The melt is calculated from monthly temperatures using a parameterization that contains a direct temperature and insolation effect (e.g. Pollard, 1980; Oerlemans, 2001):

$$M = \Delta t * \left[\tau_a \left(1 - \alpha\right) Q + c + 10\, T\right] / (1000\, L_m), \tag{6.4}$$

where M is the monthly melt in meters water equivalent, Δt is the number of seconds in a month, τ_a is the total transmissivity of the atmosphere, taken here as 0.5, $c + 10\, T$ is the sum of the longwave radiation and turbulent exchange, T is the surface temperature in degrees Celsius, Q is the monthly insolation at the top of the atmosphere in W/m^2, which is adjusted every 1000 years, and L_m is the latent heat of melt. Comparing modelling results with geomorphological evidence on ice extent resulted in an optimum value for c of -100 for our set of parameters and ice flow model.

The albedo is calculated as in Bintanja and others (2002)

$$\alpha = \min\left(\alpha_g + 10\left(\alpha_s - \alpha_g\right) d, \alpha_s\right), \tag{6.5}$$

where α_g is the ground albedo (0.2 for a bare surface, 0.45 for ice), α_s is the albedo for snow (0.8) and d is the snow depth in meters water equivalent. The snow depth varies throughout the year based on the cumulative monthly mass balance, but is limited to 10 meters.

6.2.3 Flexural earth model (ELRA)

The response of the solid earth to an ice-load can to first order be described by the bending or flexure of an elastic lithosphere combined with a time delay due to the viscous properties of the mantle below. If we assume that the elastic properties and the thickness

of the lithosphere are constant throughout the plate, the behavior of the lithosphere can be described by a well-known fourth-order differential equation (e.g. Turcotte and Schubert, 2002; Van der Veen, 1999; Brotchie and Silvester, 1969)

$$D\nabla^4 w - q = 0, \tag{6.6}$$

where w is the vertical deflection, ∇ is the two-dimensional biharmonic operator, $q = q_{load} - \rho_m g w$ is the load minus the buoyancy of the mantle, and D is called the effective flexural rigidity. This is a measure for the strength of the lithosphere and is defined as

$$D = \frac{Eh^3}{12\left(1-\nu^2\right)}, \tag{6.7}$$

where h is the thickness of the elastic lithosphere, and E and ν are elastic parameters, Young's modulus and Poisson's ratio respectively.

Equation (6.6) can be solved analytically for an impulse load. This results in a Green's function, which can be convolved with a more general spatial load distribution to find the overall earth response.

Equation (6.6) describes an instantaneous elastic response. The dominant component of the earth response is not instantaneous due to the viscous nature of the mantle. Therefore, the temporal response has a time delay and within the ELRA model this is calculated as (e.g. Van der Veen, 1999):

$$\frac{\partial b}{\partial t} = -\frac{1}{\tau}\left(b + w - b_0\right). \tag{6.8}$$

This is a simple first order approach in which the response of the mantle is characterized with one single relaxation time τ. The parameter w is the total subsidence as calculated by the lithospheric model, b is the height of the bedrock, and b_0 is the initial topography, hence the steady state topography without ice.

6.2.4 Spherically symmetric self-gravitating viscoelastic earth model (SGVE)

Compared to the ELRA model, the SGVE model provides a more accurate estimate of the earth response to a surface loading. Not only is the geometry of the model more earth-like (a series of concentric spherical shells) but the crust and mantle are defined as a viscoelastic material, and as such can respond to a given load with both an immediate elastic component of deformation and a time-delayed viscous component. The model is also self-gravitating, and so the interaction between changes in the gravitational potential and the density structure of the model, as deformation progresses, is incorporated (see, for example, Wu and Peltier (1982).

The SGVE model consists of an inviscid core surrounded by a viscoelastic mantle and crust. As for the case of the ELRA model, the response of the SGVE model to a specific loading history is calculated by convolving this history in space and time with

the so-called impulse response, the response of the model to an impulse loading (e.g. Peltier, 1974). The impulse response for the vertical surface deflection (w) is commonly expressed as,

$$w(R,\gamma,t) = \frac{\phi_{2,l}(R)}{g} \sum_{l=0}^{\infty} h_l^L(t)\, P_l\left(\cos(\gamma)\right), \tag{6.9}$$

where R is the radius of the earth model, γ is the great circle angle between the impulse load point and the observation point, t is time subsequent to the application of the impulse loading, $\phi_{2,l}$ represents the degree l component in the Legendre expansion of the perturbation to the surface gravity field caused by the direct attraction of the impulse loading, g is the surface gravitational acceleration, and the P_l are Legendre polynomials. The coefficients $h_l^L(t)$ are the surface load viscoelastic Love numbers for the radial displacement, and can be written more fully as,

$$h_l^L = h_l^E \delta(t) + \sum_{k=1}^{K} r_k^l \exp(-s_k^l\, t), \tag{6.10}$$

in which the $\delta(t)$ denotes the Dirac delta function. It is evident from equation (6.10) that the temporal aspect of the response is composed of an immediate elastic component, defined by h_l^E, and a non-elastic component which consists of a series of exponential functions defined by an amplitude, r_k^l, and inverse decay time s_k^l . These three parameters are defined by the density and rheological (elastic and viscous) structure assigned to the earth model. Note that the non-elastic response is described by a spectrum of decay times compared to a single decay time for the ELRA model.

In most applications of the SGVE model, the elastic and density structure are taken from seismic constraints and the viscous structure is constrained via forward or inverse modeling procedures. For our purposes, we define a reference model in which the elastic and density structure are taken from PREM (Dziewonski and Anderson, 1981) and defined with a depth resolution of 10 km in the crust and 25 km throughout the mantle. The viscous structure is more crudely defined into three spherical shells: an upper layer of thickness 96 km with very high viscosity (10^{43}Pas) to model the lithosphere, an upper mantle region of viscosity 5x10^{20}Pas that extends from the base of the lithosphere to the 660 km seismic discontinuity, and a lower mantle region of viscosity 10^{22}Pas from 660 km to the core-mantle boundary (2900 km depth). This viscosity structure is broadly compatible with recent isostatic adjustment modeling studies of data from Fennoscandia (e.g. Lambeck et al., 1998b,a; Milne et al., 2001, 2004). To compute the radial component of surface motion we employed the spectral technique described in Mitrovica and others (1994).

6.3 One-dimensional tests

We performed numerical sensitivity tests with an ice flow model with axial symmetry and the ELRA model to assess the effects of lithospheric strength and relaxation times on the

growth and decay of ice.

The experiments were performed on an initially linearly sloping bed

$$b_{init} = max\left(-2000, 1500 - 3.75\, r\right), \tag{6.11}$$

with b_{init} in meters and distance from the centre r in kilometers.

6.3.1 Modelling results

The resulting initial mass balance is shown in Figure 6.1 for a constant temperature and a constant value of the insolation of 236.6 W/m^2, the average present day value for 60^{o}N. The mass balance (i) reduces when the ice sheet grows due to less advection of humid air and less in situ evaporation, (ii) is asymmetric due to orographic effects and advection. Importantly, the maximum mass balance occurs not at the highest point of the ice sheet, but near the margin where the orography is steepest. For more details see Van den Berg et al (2006b).

We performed the experiments on two grids; one with a discretization distance of 2 km and one of 20 km. The latter discretization is most common in glaciological applications for reasons of computational efficiency. However, Van den Berg and others (2006a) showed that the numerical scheme may not be fully converged until Δx=2 km depending on local geometry. To fully examine the effect of isostatic adjustment on our results we show the results for both discretizations.

Figure 6.2 shows the results of the one-dimensional experiment for Δx=2 km. The plots show the ice volumes for the case without isostatic adjustment and for several values of the effective flexural rigidity and relaxation time. The response for $D = 10^{20}$Nm is very similar to the local isostatic response. There are several interesting features evident in Figure 6.2.

Given the results of Crucifix and others (2001) we would expect that a higher elevation means a higher mass balance, hence a larger ice sheet. Since weak lithosphere has the most local, deepest response, this situation should result in the smallest ice sheet. Figure 6.2 shows that this is not the case. Not only is the ice sheet for the weakest lithosphere the largest of all isostatic cases, the ice sheet is also comparable in size to the one calculated without isostatic adjustment. Remarkable is that the ice volume decreases when the flexural rigidity increases due to the spatial differences in earth response.

Depending on the local mass balance profile, a lower centre does not necessarily mean a lower mass balance. At altitudes without melting, a lower surface can result in a higher mass balance, since the higher temperature allows for more moisture in the atmosphere. Moreover, if the ice growth is fast compared to the downward movement of the bedrock, the ice surface may be able to keep up. This is also shown in Figure 6.2, where for a particular rigidity increasing the response time of the earth results in slightly larger ice sheets.

Whereas a lower centre does not necessarily mean a lower mass balance, a lower margin does. The ice margin is always in a region which experiences melt (except for Antarctica, where the margin is dominated by ice calving into the ocean). Hence, lowering

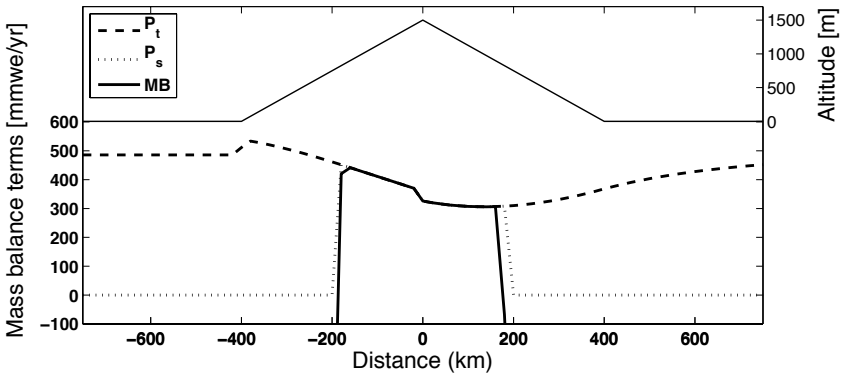

Figure 6.1: Mass balance (MB), solid precipitation (P_s) and total precipitation (P_t) for the initial geometry as shown by the thin solid line above the mass balance terms and a wind field of 3 m/s from left to right.

the surface in the margin area means increasing the melt. Figure 6.3 shows the steady state bedrock response for a constant parabolic load with a radius of 1000 km for several values of the effective flexural rigidity D. The bedrock in the margin area for a specific load is highest for the weakest lithosphere. The bedrock elevation is then consecutively lower for increasing rigidities. However, there is a minimum, since for very strong lithosphere the response is equal to no isostatic adjustment. This behaviour of the bedrock response in the margin area causes the difference in ice volume between the different rigidities. Thus, it is the ice margin which is most sensitive to the values for the flexural parameters.

Figure 6.4 shows the results of the one-dimensional experiment for Δx=20 km, similarly to Figure 6.2 for Δx=2 km. The absolute volumes for Δx=20 km are smaller than for Δx=2 km (note the difference in vertical scales between Figures 6.2 and 6.4), which is in agreement with the results from Van den Berg and others (2006a). However, for Δx=20 km, the most important feature, namely decreasing volumes for increasing values of the rigidity, is preserved. So, despite the differences between the two discretizations, we adopt the coarser grid to compare modelling results for different earth models.

6.4 A comparison between the earth models for parabolic loads

As a next step we compared the SGVE earth model to the ELRA model. We applied static, parabolic loads on an initially flat earth:

$$H(r) = \sqrt{10\,(R_L - r)}, \tag{6.12}$$

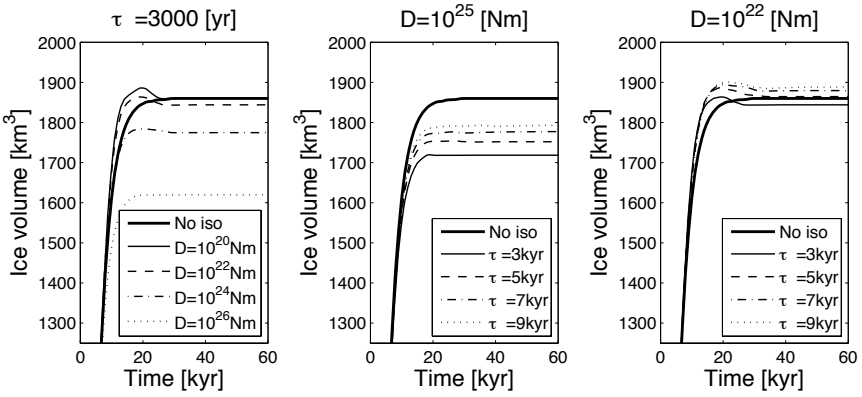

Figure 6.2: Ice volume relative to the case without isostatic adjustment for several values for the effective flexural rigidity D and the relaxation time τ. This for the mass balance based on the moisture balance concept as discussed in the main text for Δx=2 km.

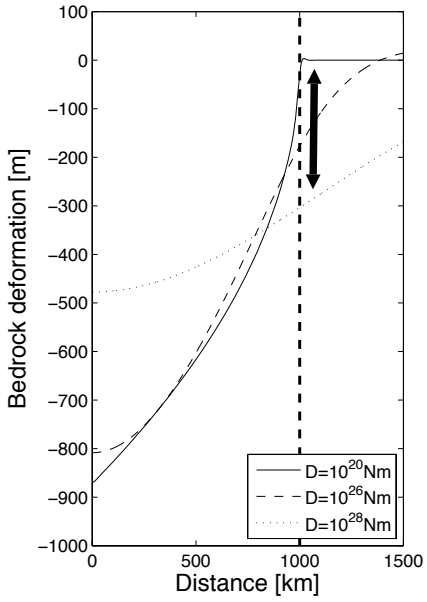

Figure 6.3: Bedrock deformation for several rigidities for a constant parabolic load. The load margin is at the thick dashed line.

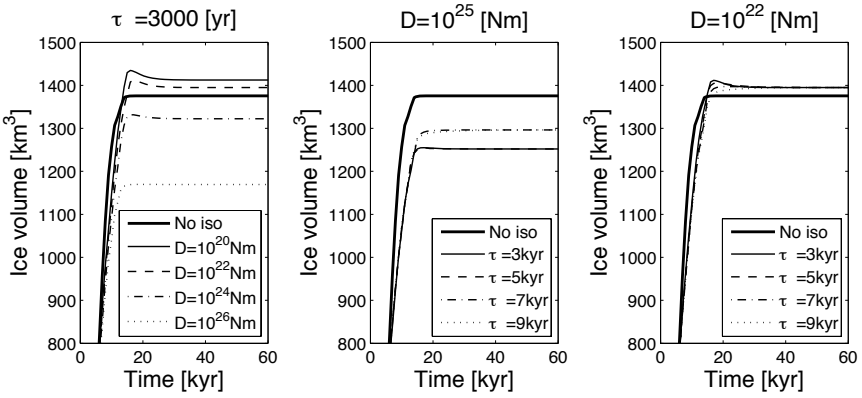

Figure 6.4: Ice volume relative to the case without isostatic adjustment for several values for the effective flexural rigidity D and the relaxation time τ. This for the mass balance based on the moisture balance concept as discussed in the main text for Δx=20 km.

with H the thickness of the (ice) load, r the distance from the centre and R the radius of the load. We performed three tests with radius R_L equal to 250 km, 500 km and 1000 km. The density of these loads was equal to 910 kg/m^3, the density of ice. Since steady state ice loads are close to parabolic shape, these loads represent typical ice loads.

We regard the response of the physically more realistic SGVE earth model as the reference case. We then compared this reference response to the response of the ELRA model for several combinations of effective flexural rigidity (D) and relaxation time (τ). Figure 6.5 shows the results of the comparison. The comparison was made with a standard L1-norm

$$L1(D,\tau) = \frac{\sum_A \sum_t \left| b^{(D,\tau)}_{ELRA}(x,y,t) - b_{SGVE}(x,y,t) \right|}{\sum_A \sum_t |b_{SGVE}(x,y,t)|}, \tag{6.13}$$

where the summations are over the spatial domain A and time t, and $b(x,y,t)$ is the bedrock corresponding to either the ELRA or the SGVE model as denoted by the subscript. The minimum in these plots represents the best fit between the response of a particular combination of D and τ and the SGVE earth model. The crosses in Figure 6.5 indicate the optimum fit.

As we can observe in Figure 6.5, the misfit plots are different for each load. The optimum fit is different for each load with in general larger relaxation times and a slightly smaller rigidity for larger loads. Large loads are more sensitive to deeper structure within the SGVE model, since they induce deformation deeper within the earth model, than small loads. In practice this means that the effective flexural rigidity and relaxation time are a function of the load size. Since the viscosity increases with depth, a large load will experience a longer relaxation time than a small load. With regards to dynamical ice flow

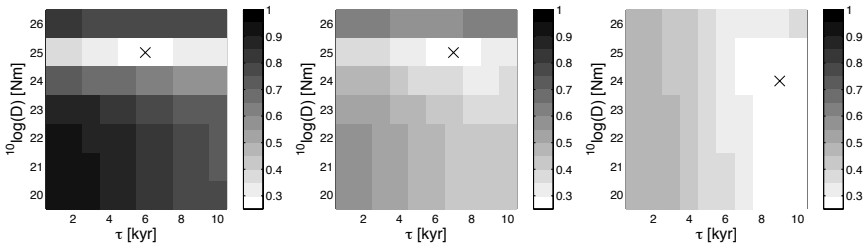

Figure 6.5: L1 norm for the bedrock deformation for a schematic parabolic load with radius 250 km (left), 500 km (middle) and 1000 km (right). The cross indicates the optimum fit in each plot.

modelling this is important, since during a glacial cycle an ice sheet moves through a whole range of sizes. No particular combination of effective flexural rigidity and relaxation time will fit perfectly during an entire glacial cycle, so differences in the bedrock response between the ELRA model with optimum values for D and τ and the SGVE earth model will always occur. Since ice responds nonlinearly to altitude differences through the mass balance-height feedback, this is a potential source of error. Moreover, any different ice evolution may result in a different optimum value for the effective flexural rigidity D and relaxation time τ.

The overall fit in Figure 6.5 improves for larger loads. For small loads the sensitivity is dominated by the effective flexural rigidity, whereas for large loads the sensitivity is dominated by the relaxation time. Figures 6.6 and 6.7 show, respectively, cross-sections of the vertical deformation for load radius R_L=250 km and R_L=1000 km for the SGVE earth model, the ELRA model with optimum combination of D and τ for that load. In addition, Figures 6.6 and 6.7 show the most commonly used ELRA model in glaciology with $D = 10^{25}$Nm and $\tau = 3$kyr, and an additional ELRA model with $D = 10^{22}$Nm and $\tau = 9$kyr to illustrate model sensitivity. Clearly, a decay time $\tau = 3$kyr is too fast for all cases considered in Figure 6.5. However, for R_L=250 km this is obscured by the much larger differences that occur between the different rigidities. For R_L=1000 km all rigidities produce a very similar response in the center. Therefore, in this case the relaxation time determines the largest error.

A key point is that no combination of D and τ for the ELRA model can reproduce the SGVE response completely. Both in the center and near the margin, the SGVE and ELRA earth models behave intrinsically different. The previous section showed that ice dynamical models are sensitive to isostatic behaviour near the ice margin, suggesting that this fundamental limitation of the ELRA model is a significant source of error. This sensitivity is explored in the following section where the model is applied to the Eurasian Ice Sheet.

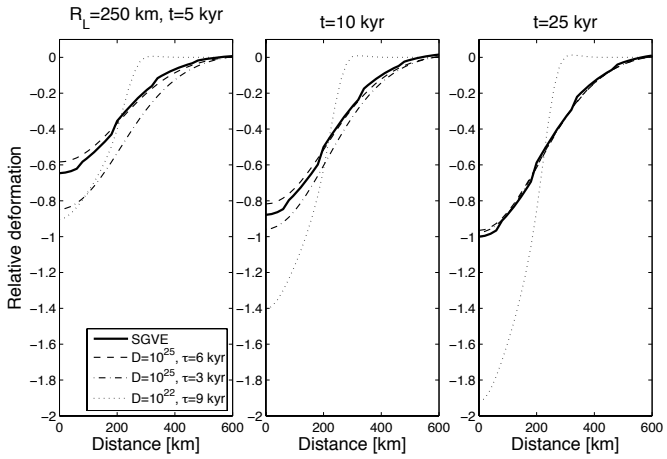

Figure 6.6: Relative deformation as a function of time for the SGVE, the optimum ELRA model with $D = 10^{25}$Nm and $\tau = 6$kyr, the commonly used ELRA model with $D = 10^{25}$Nm and $\tau = 3$kyr and an ELRA model with $D = 10^{22}$Nm and $\tau = 9$kyr for the parabolic schematic load with radius 250 km.

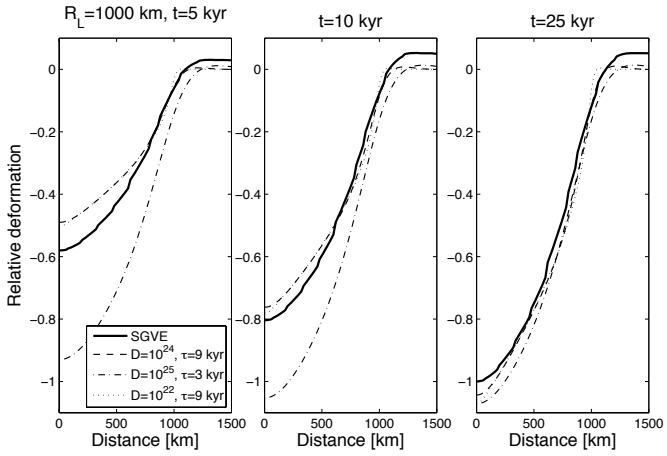

Figure 6.7: Similar to Figure 6.6, but now the optimum ELRA model has values $D = 10^{24}$Nm and $\tau = 9$kyr.

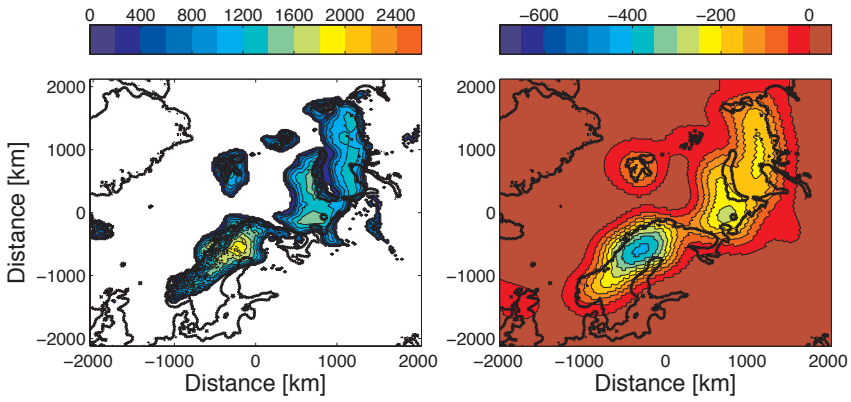

Figure 6.8: Ice distribution [m ice thickness] and bedrock deformation [m] for the SGVE earth model at 100,000 BP.

6.5 An application to Eurasia

In the following section we compare predictions based on the SGVE and ELRA earth models for a full glacial transient ice evolution of the Eurasian Ice Sheet. We coupled the mass balance as described in Section 6.2.2 to a dynamical ice flow model with a discretization distance of 20 by 20 kilometers. The temperature was forced by the temperature perturbation as a function of time as described in Bintanja and others (2005). The sea level changes were not internally generated, but prescribed as a eustatic signal. The sea water was assumed to have zero density, so that the eustatic changes in sea level did not influence the isostatic response. Unlike the previous experiments which had a schematic initial topography, the present day topography of Eurasia was assumed to be the same as 123,000 BP, the time at which the model run was started without initial ice.

Figure 6.8 shows the ice distribution and bedrock deformation at time 100,000 BP for the SGVE earth model. Note that the figure represents a time slice from a transient run and not a steady state. This ice distribution after only 25,000 years of modelling shows that in practice the ice sheet moves through the "$R_L = 250$km-stage" very fast. The ice sheet is already on the order of R_L=1000 km. Therefore, we expect that the optimum combination of effective flexural rigidity D and relaxation time τ will be more closely aligned with the values given in the right hand frame of Figure 6.5, which represents the R_L=1000 km case. Figure 6.9 shows the ice distribution and bedrock deformation near the time of the LGM around 17,000 BP for the SGVE model. Again, this figure represents a time slice from a transient run. A comparison between the results in Figures 6.9 and 6.8 shows that the separate ice domes over the Barents and Kara Seas and Scandinavia have merged.

Figure 6.10 shows the optimum fit between the modelled bedrock response for the SGVE and the ELRA model for several combinations of D and τ. We show the fit both

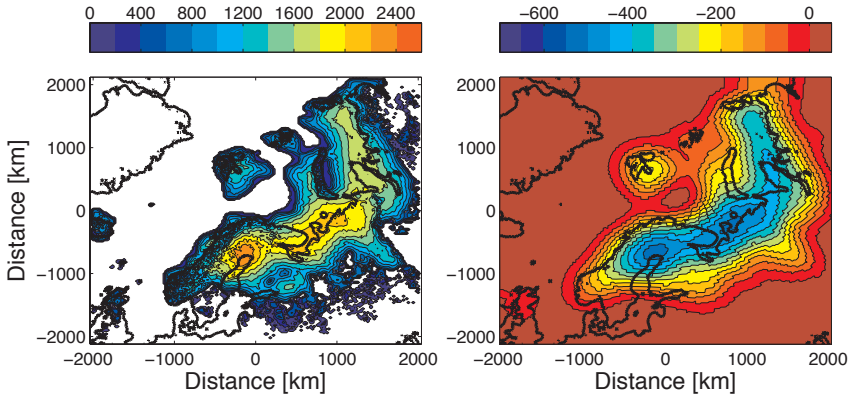

Figure 6.9: Ice distribution [m ice thickness] and bedrock deformation [m] for the SGVE earth model at LGM.

for the time 100,000 years BP and the LGM at 17,000 years BP. The plot for time 100,000 BP looks very similar to Figure 6.5 with the sensitivity to rigidity as in the $R_L = 250$km figure. As expected, the optimum relaxation time resembles the relaxation time for larger loads. The difference in sensitivity is caused by the fact that the ice had to pass several sizes, whereas in the schematic experiments the loads were constantly one size. The plot for LGM however, is different; the trend of longer relaxation times for larger loads is not reproduced. Instead, we see a smaller optimum relaxation time of only 5 kyr. Moreover, the fit is much worse for the LGM in comparison with the situation for 100,000 BP, whereas Figure 6.5 predicts that the fit should increase for larger loads. This is a result of the nonlinear response of the ice to differences in surface altitude. Accumulating errors in the ice distribution over time cause the observed trends in the misfit.

Besides comparing the bedrock response, we can also compare parameters directly related to the ice sheet, as ice thickness distribution and ice sheet volume. Figure 6.11 shows the optimum fit between the ice thickness distribution for the SGVE and the ELRA model for several combinations of D and τ both for the time 100,000 BP and the LGM. We see the same trend as in Figure 6.10 of reducing relaxation time and larger misfits for LGM. However, the optima are not the same as for the bedrock comparison.

The top frames in Figure 6.12 show the ice distribution and bedrock deformation at LGM for the optimum bedrock fit of $D = 10^{25}$Nm and $\tau = 5$kyr. The bottom frames in Figure 6.12 show the same for the optimum ice distribution fit for LGM of $D = 10^{24}$Nm and $\tau = 5$kyr. The ice for $D = 10^{24}$Nm is slightly thicker in the center of the domes and the bedrock pattern shows more variability. By comparing the top and bottom figures in Figures 6.12 to the SGVE reference results for LGM in Figure 6.9, we see that both optima underestimate the ice thickness generated by the SGVE model. The SGVE model produces thicker ice in the center of the domes. It also produces one, large dome centered over Scandinavia and the Russian coast, whereas the ELRA models do not produce

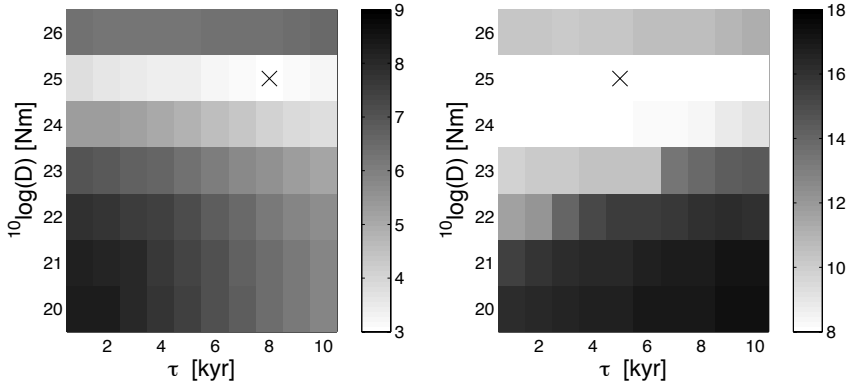

Figure 6.10: L1 norm for the bedrock fit at 100,000 BP (left) and LGM (right). The cross indicates the optimum fit in each plot.

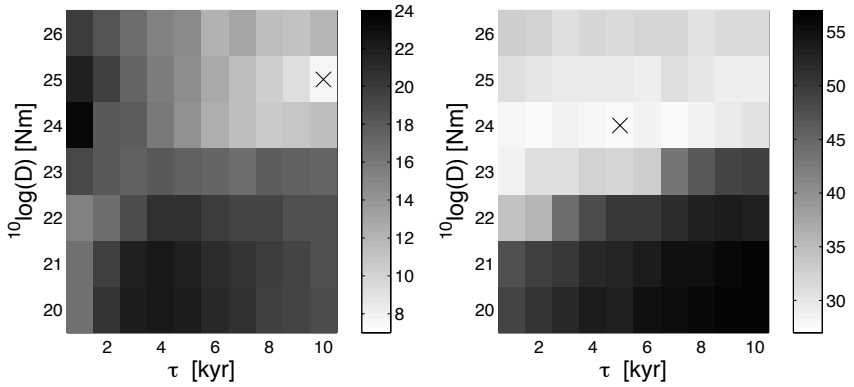

Figure 6.11: L1 norm for the ice distribution fit at 100,000 BP (left) and LGM (right), instead of the bedrock fit as shown in Figure 6.10. Note also the difference in scaling between these plots and the plots in Figure 6.10.

enough ice for their two separate domes to merge.

Figure 6.13 shows the ice volume as a function of time for both the SGVE model and the best fitting ELRA model with $D = 10^{22}$Nm and relaxation time $\tau = 9$kyr. It also shows the ice volume for the two optimum ELRA models for the LGM as derived from the bedrock deformation and the ice thickness. The middle plot shows the ice volume around the LGM, the right plot shows the ice volume in the last 10,000 years BP. Compared to the reference SGVE model, the ELRA models with best fitting bedrock deformation and ice thickness underestimate the LGM ice volume by as much as 30 percent.

Figure 6.14 shows the ice thickness distribution and bedrock deformation for the best fitting ELRA model for ice volume. Even though the total ice volume is very similar to the ice volume predicted by the SGVE model, the ice distribution and bedrock deformation are fundamentally different from the SGVE model in Figure 6.9 or the optimum combinations of D and τ for the ELRA model as shown in Figure 6.12. Instead of a large dome centered over the Russian coast and Scandinavia as predicted by the SGVE model, we see one single dome centered in the Barents Sea much further to the north. Even though the overall ice volume is the same as the SGVE ice volume, this ice distribution would never produce the same bedrock response and hence relative sea level curves as the SGVE ice distribution in large parts of the domain. This shows the danger of using only one integral variable, such as ice volume or mean bedrock elevation, to estimate the best fitting ELRA model. It also demonstrates the large difference in results that may occur between several realistic parameter combinations in an ELRA model.

We performed similar tests with another SGVE model with a different lithospheric thickness of 70 kilometers. Compared to the SGVE model with a lithospheric thickness of 96 kilometers, this model produced a 5 percent higher ice volume at the LGM. The optimum fits hardly changed and the conclusions that no ELRA model could fit all parameters as ice thickness, bedrock deformation and ice volume remains the same.

6.6 Conclusions

We performed several experiments to assess and compare the ice sheet evolution and the isostatic response to two types of earth models. The first is the most commonly used earth model in ice sheet modelling, a flexural model (ELRA) consisting of an elastic plate with an effective flexural rigidity D and a single relaxation time τ to account for temporal behaviour. The second is a self-gravitating viscoelastic spherically symmetric earth model (SGVE). This SGVE model was regarded as reference in this paper, since it more closely represents the geometry and rheology of the real earth.

Using the ELRA model we assessed the dynamical response of ice sheets to different values of the effective flexural rigidity and the relaxation time. Contrary to the results of Crucifix et al. (2001) the ice sheet for the smallest effective flexural rigidity was comparable to the ice sheet calculated without isostatic adjustment. With the mass balance model applied in this paper, which has a strong feedback with altitude and surface slope, the ice buildup was fast enough to keep up with the downward motion of the earth surface. This resulted in the ice surface ”filling up the gap” instead of lowering to regions with more

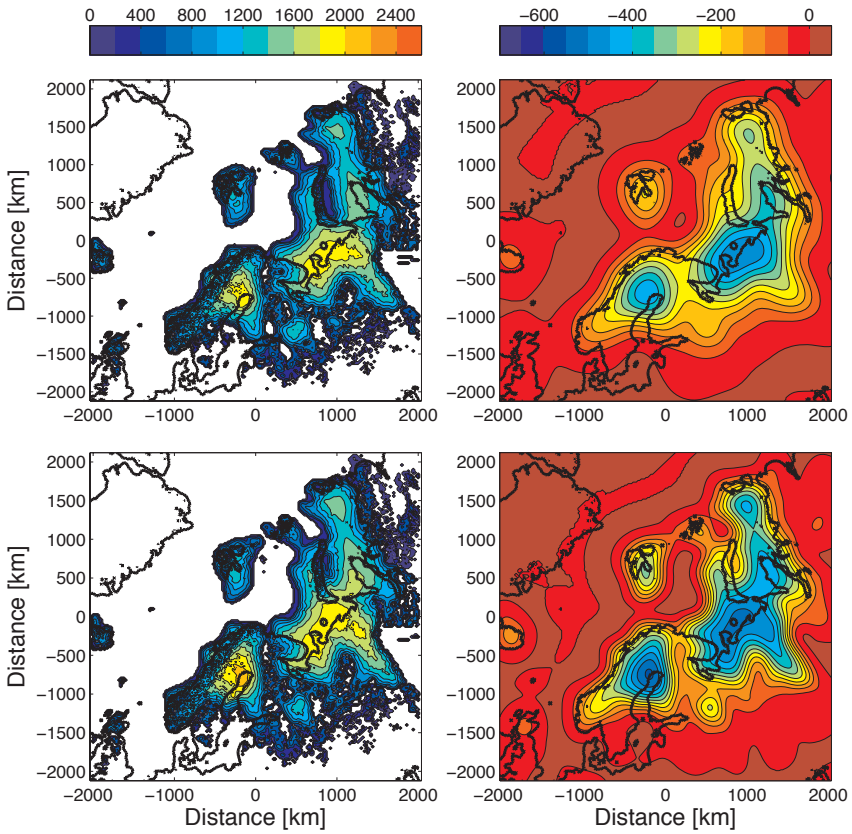

Figure 6.12: Ice distribution [m ice thickness] and bedrock deformation [m] for $D = 10^{25}$Nm (top figures) and $D = 10^{24}$Nm (bottom figures) and τ =5kyr at LGM.

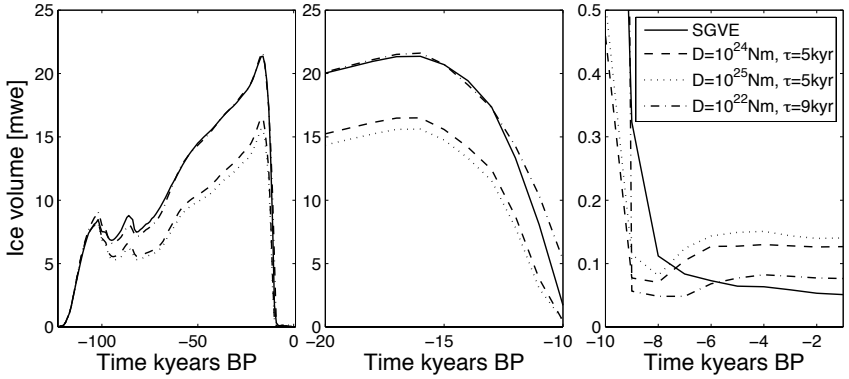

Figure 6.13: Ice volume as a function of time for several earth models. The two right plots are a zoom of the left plot.

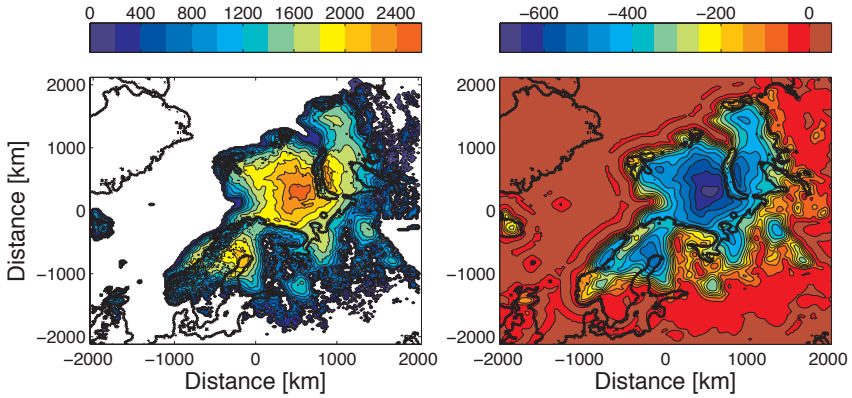

Figure 6.14: Ice distribution [m ice thickness] and bedrock deformation [m] for $D = 10^{22}$Nm and $\tau =$9kyr at LGM.

melt. Increasing flexural rigidities resulted in ice sheets with up to 15 percent less volume due to the geometry of the earth deformation in the region of the ice margin. This is the region most sensitive to changes in the surface elevation. Thus, the response of dynamical ice sheets to patterns in isostatic response turns out to be more complex than previously assumed.

We compared the ELRA and SGVE models with sensitivity tests using a parabolic loading. No combination of effective flexural rigidity D and relaxation time τ for the ELRA model was able to correctly model the SGVE response. The models have an intrinsic different spatial and temporal response. To illustrate the effects of this fundamental limitation of the ELRA model on a dynamical ice sheet, we also performed a transient glacial run for Eurasia. Eurasia is an interesting case study, partly because there are many data available on earth structure. Also, forming partly on land and partly in shallow seas with the existence of an ablation zone, it is representative for the Northern Hemispheric ice sheets. Le Meur and Huybrechts (1996) concluded for a study in Antarctica that the ELRA model is a reasonable computationally efficient alternative to the SGVE model. Our results for Eurasia showed that no ELRA model was able to correctly model both ice volume and ice thickness and bedrock deformation for the Eurasian Ice Sheet for a full glacial cycle. Uncertainties in the lithospheric thickness in the SGVE model did not change this result. The best fitting ice volume ELRA model had an ice sheet geometry that was completely different from that produced by the SGVE model. The best fitting ELRA model for bedrock deformation and ice thickness distribution underestimated the SGVE ice volume at the LGM by 30 percent.

6.7 Acknowledgments

We acknowledge the international modeling groups for providing their GCM results for analysis, the Laboratoire des Sciences du Climat et de l'Environnement (LSCE) for collecting and archiving the model data. The PMIP2/MOTIF Data Archive is supported by CEA, CNRS, the EU project MOTIF (EVK2-CT-2002-00153) and the Programme National d'Etude de la Dynamique du Climat (PNEDC). More information is available on http://www-lsce.cea.fr/pmip2/. The calculations in this paper were performed on the RADON cluster of IMAU, which was partly funded by the Utrecht Centre for Geosciences. This work was financed by Spinoza, awarded by NWO to Professor J. Oerlemans. We thank Sarah Bradley and Pippa Whitehouse for providing the required SGVE model input for the initial tests.

Chapter 7

Summary and outlook

The melting of ice sheets in response to increasing temperatures is an important contribution to present day sea level rise. A further increase of temperatures in the coming century as predicted by the fourth IPCC climate assessment report (2007) will accelerate the melt and enhance sea level rise. To predict the amount of sea level rise and to assess its impact on populated coastal regions, an increased understanding of the physical processes governing ice sheets is essential.

This thesis discusses modelling of the dynamical interactions between ice sheets, climate and the solid earth. We focussed on the physical processes involved and their potential influence on ice sheet evolution. We performed sensitivity experiments to examine ice sheet response to changes in the individual system components. We also studied the numerical behaviour of the ice sheet model. This approach leads to an improved understanding of an ice sheet's response to climate change, which is essential for understanding future sea level change.

An ice sheet is a complex, dynamically active part of the earth's climate system. The response of an ice sheet to changes in the climate is highly nonlinear mainly due to the nonlinear feedback between mass balance and elevation. Both precipitation in the form of snow, and melt are strongly dependent on the geometry of the ice sheet. Hence, it is important to accurately model any process affecting the elevation and geometry of an ice sheet. This not only includes temperature and precipitation, but also bedrock adjustment and the numerical properties of the system.

7.1 Numerical behaviour of the ice sheet model

Chapter 3 discusses a series of sensitivity experiments with one and two dimensional land-based ice sheet models. We showed that the numerical behaviour of these models is very sensitive to the precise initial conditions, local geometry and climate. This is mainly caused by the numerical estimation of the surface gradient in the vicinity of the ice margin. This gradient is badly constrained at the transition from ice to no ice as explained

in Figure 3.7. Since the physical ice margin usually does not coincide with a grid point, the usually applied central differencing scheme underestimates the surface gradient. This results in ice fluxes through the margin that are too low. Together with the value of the mass balance these ice fluxes determine whether the ice sheet grows or shrinks. As such, underestimation of the ice fluxes has serious implications for the time dependent solution of the system. Seemingly small errors accumulate nonlinearly over time due to the height-mass balance feedback. This effect is strongly dependent on the spatial resolution of the model grid. Synthetic experiments with ice sheets evolving to steady state for a simplistic, height dependent mass balance profile showed that the widely used spatial discretization distance of 20 by 20 kilometers is too coarse. Ice sheets calculated with such a resolution might underestimate the ice volume by 80 percent depending on local geometry. At grid resolutions of about 2 by 2 kilometers the solution becomes independent of the resolution.

T overcome these problems, we proposed a new operator for the calculation of the surface gradient in the vicinity of the margin. Instead of using a central differencing operator over the ice-no ice transition we used an operator containing only grid points inside the ice sheet domain. It exploits the information on the curvature in the last points before this transition. The new procedure significantly improved the modelling results. However, it did not completely solve the problem.

We derived a dimensionless "flux number" to assess in which situations numerical problems may occur:

$$\mathrm{Fluxnumber} = \frac{L_v\, U_c}{L_h\, a}, \tag{7.1}$$

where $L_{v,h}$ is the characteristic vertical ($_v$) or horizontal ($_h$) length scale, U_c is a characteristic ice velocity and a is a characteristic scale for the mass balance. For flux numbers approaching or surpassing the value one, the ice sheet evolution is dominated by the calculation of the ice flow. The numerical issues discussed above may then be important. On the other hand, when the flux number is much smaller than one, the ice evolution is dominated by the mass balance and less by the numerical inaccuracies in the calculation of the ice flow. This behaviour was confirmed in sensitivity experiments in which the values for important parameters as bedrock slope and maximum mass balance were varied. For example, as expected from the flux number, the numerical problems for ice sheets in wet (maritime) areas were not nearly as large as for dry (continental) areas. A wet area has a higher value for a then a dry area (assuming the same mass balance gradient), hence a smaller value for the flux number. This shows that the flux number is a good indicator regarding the issue of numerical inaccuracies. Compared to a mountain glacier with a typical flux number of less than 0.1, the ice margin of a large ice sheet has a much larger flux number of 1 or higher. This means that for large ice sheets this type of numerical inaccuracies are far more important than for mountain glaciers. For mountain glaciers inaccuracies in the calculation do not arise from the reasons mentioned above, but from subgrid geometrical features.

7.2 The resolving power of bedrock data

In chapter 4 we studied a flexural earth model which can incorporate lateral variations in lithospheric strength. There are strong indications that variations over several orders of magnitude exist in regions (formerly) covered with ice. For example, in Antarctica there is a division between West Antarctica having a weak, almost oceanic lithosphere, and East Antarctica having very a strong, cratonic lithosphere, with the Trans Antarctic Mountains as transition between the two regimes. In Scandinavia it is suggested that the lithospheric strength increases from weak, oceanic lithosphere toward strong continental lithosphere with a transition roughly in the Gulf of Bothnia. We considered a synthetic ice age cycle with a simplified bedrock geometry and mass balance profile coupled to a two dimensional vertically integrated dynamical ice sheet model. We used this to illustrate the response of the earth model, and to assess the potential of isostatic adjustment data to constrain the lateral earth structure. This example showed that differences in earth structure influence ice extent and thickness. The ice volume difference between different lithospheric strengths was about ten percent.

In addition, we presented a scheme which simultaneously solves for earth structure and the corresponding best ice sheet reconstruction. A synthetic pilot study indicated that even noisy data can constrain the lithospheric strength and detect lateral variations, as long as the data are spread around the variations in strength and the noise levels in the uplift data do not exceed twenty percent.

Most methods to constrain earth structure use prescribed ice loading reconstructions, which are generally based on optimization procedures using relative sea level data. The approach of using a dynamical ice sheet model is a worthwhile addition of information, since the resulting ice load is based on different data and assumptions than the ice sheet reconstructions, which are ice dynamically not inherently consistent.

7.3 A mass balance model for Eurasia

The actual impact of lithospheric strength on ice sheet evolution is difficult to assess in simplified experiments. Realistic ice sheets are subject to a more complex geometry and climate. Since ice sheets respond nonlinearly to changes in surface elevation, this complexity may result in different behaviour for the influence of earth structure on ice dynamics compared to simplistic sensitivity experiments.

To test the dynamical response of realistic ice sheets to differences in earth structure for more realistic conditions, we modelled the Eurasian Ice Sheet through the last glacial-interglacial from 120,000 years BP to present day. The Eurasian Ice Sheet is an interesting case study, because Eurasia is the continent with the most abundant data on earth structure and ice extent as a function of time, and because its ice dynamical characteristics. The Eurasian Ice Sheet formed partly on land and in shallow seas. As a result, both the mass balance parameterization as the ice shelf formation play an important role in the evolution of the ice sheet. Therefore, this ice sheet represents a mixture between the fully land-based Laurentide Ice sheet and the Antarctic Ice Sheet, where changes are mainly determined

by grounding line migration.

The linear mass balance profiles used in chapters 3 and 4 are too simplistic for a realistic, complex geometry. As we are specifically interested in the interactions between ice sheets and the other components of the climate system, we discussed a mass balance parameterization for Eurasia based on the elementary physical processes that govern the evolution of ice sheets (chapter 5). The Eurasian Ice Sheet receives its moisture primarily from the Atlantic Ocean. Orographically induced precipitation and advection of humid air are thought to control the dimensions and geometry of the ice sheet. Therefore, we used a precipitation parameterization based on the concept of a moisture conservation law. Key elements of the mass balance parameterization include; (i) advection of moisture controls the dimensions of the ice sheet, (ii) mass balance profiles and resulting ice sheets are asymmetric due to orography and wind, and (iii) the ice sheets dry as they grow, because advection only has a certain range and evaporation over ice is very small. Comparing the results of a test for present day conditions in Eurasia with precipitation data between 1960 and 1990 showed that the parameterization worked well with mean absolute differences of less than 200 mm/yr. Given the range of 100-3000 mm/yr and the simplicity of the model this is a remarkably good result. Compared to other widely used mass balance parameterizations, this approach has the advantage that the ice sheet evolution has a non-linear feedback with altitude both in the melt, which is a function of temperature, and in the precipitation, which is a function of temperature and surface slope. Moreover, the advection scheme allows for a consistent regional distribution of available moisture.

This mass balance model was coupled to a dynamical ice sheet model to simulate the glacial history in Eurasia over the last 120,000 years. The model was tuned to present day conditions only, and otherwise evolved freely with the changing geometry of the ice sheet. We compared the modelled ice sheet to the data compilation from the QUEEN program (Svendsen et al., 2004). In general, the model performs well during the early stages of the modelling period, after which the performance decreases towards the LGM around 17,000 BP. At the LGM the differences with the data are considerable. A possible explanation is that spatial and temporal changes in the wind and temperature field occurred over time, which were neglected. Tests to assess the impact of uncertainties in the wind field and the temperature perturbation showed that these parameters are very influential; a 20 percent increase in the temperature perturbation resulted in 50 percent more ice volume at the LGM, whereas using the present day wind field instead of a simplified parameterization resulted in 40 percent more ice volume at the LGM.

7.4 Effects of isostatic adjustment on ice sheet evolution; a case study in Eurasia

With the mass balance parameterization as discussed in Chapter 5, in Chapter 6 we continue with the effects of isostatic adjustment on ice sheet evolution for more realistic geometries than the simplified experiments in Chapter 4. In this chapter we focused on the importance of differences in the spatial and temporal response of earth models in the

evolution of ice sheets. Those differences may arise from differences in the earth structure or from different approaches to the modelling of the earth. Contrary to chapter 4, we used the mass balance model as described in chapter 5, since this model is more realistic and can be applied to more complex geometries.

Using a flexural model we studied the response of ice sheets to different values of the effective flexural rigidity and the relaxation time. We found that isostatic adjustment is not necessarily a negative feedback on ice sheet growth as previously assumed. In our experiments the mass balance was high enough so that the elevation of the ice surface increased faster than the bedrock subsided. This resulted in "filling of the isostatic depression", instead of subsiding to elevations with increased melt.

Increasing flexural rigidities from $D = 10^{20}$Nm to $D = 10^{26}$Nm resulted in ice sheets with up to 15 percent less ice volume. For larger flexural rigidities the spatial response of the earth is more regional and smooth. For higher values of the effective flexural rigidity the elevation of the bedrock in the vicinity of the ice margin decreases, which results in more melt. The ice margin is a region very sensitive to changes in elevation, since the mass balance in this region directly determines growth or retreat of the ice sheet. Thus, the response of dynamical ice sheets to patterns in isostatic response turns out to be complex, as it depends not only on the earth parameters, but also on the mass balance parameterization.

We compared the flexural model, with an elastic lithosphere and one relaxation time (ELRA), and the physically more realistic spherically symmetric self-gravitating viscoelastic earth model (SGVE). We performed sensitivity tests for parabolic loadings and for a transient run over a glacial-interglacial in Eurasia. No combination of effective flexural rigidity D and relaxation time τ for the ELRA model was able to correctly model the SGVE response. The models have an intrinsically different spatial and temporal response.

Le Meur and Huybrechts (1996) concluded for a study in Antarctica that the ELRA model is a reasonable computationally efficient alternative to the SGVE model. Our results for Eurasia showed that no ELRA model was able to correctly model both ice volume and ice thickness and bedrock deformation for the Eurasian Ice Sheet for a full glacial cycle. Accumulating errors in the ice reinforced by the nonlinear feedback between height and mass balance make the two types of earth models incompatible. Uncertainties in the lithospheric thickness in the SGVE model did not change this result. The best fitting ice volume ELRA model had an ice sheet geometry that was completely different from that produced by the SGVE model as observed in Figures 6.9 and 6.12 to 6.14. The best fitting ELRA model for bedrock deformation and ice thickness distribution underestimated the SGVE ice volume at the LGM by 30 percent.

7.5 Recommendations and outlook

In most of the experiments discussed in this thesis we encountered evidence for numerical problems regarding the calculation of the surface gradient in the vicinity of the ice margin with consequences of varying severity. Therefore, we recommend to examine the fluxnumber, as defined by equation (7.1), in any application. If the value for this number

approaches or surpasses one, underestimation of the surface gradient may cause problems in the calculation of ice sheet evolution. We also recommend to use the slope correction formula as defined in equation (3.17). Finally, since the flux number only provides an indication of numerical behaviour, we recommend to use different spatial grid discretization distances and assess the differences in resulting ice sheets.

In this thesis we focussed on the dynamical interactions between physical processes. The results for Eurasia were sufficiently good to encourage continuation of the research with a shift in focus towards data. To increase understanding of paleoclimate and earth structure in Eurasia, we need to improve the fit between modelled ice sheets and the available geomorphological indicators. More specifically, we need to compare the modelled ice sheets with the extensive database of relative sea level records in Eurasia (e.g. Lambeck et al., 1998b). To facilitate such a comparison, we need to incorporate the calculation of the relative sea level instead of using a eustatic sea level curve. In this thesis we used a eustatic sea level curve, mainly because it is computationally efficient and adequate when only interested in the influence of physical processes. For a comparison with relative sea level data however, using a eustatic signal is no longer an option. As demonstrated in the Introduction the relative sea level is very dissimilar to the eustatic signal in regions close to the ice sheet. This means we cannot accurately predict the relative sea level records in Eurasia with a eustatic forcing. Besides the direct influence on the observational records, relative sea level change is of importance to ice sheet dynamics in two aspects. Firstly, changing sea levels form an important contribution to the isostatic adjustment, which has a considerable influence on ice sheet evolution (as shown in Chapters 4 and 6). Secondly, the sea level is of importance in the calculation of the floating ice shelf and the position of the grounding line. Therefore, we recommend to calculate the relative sea level simultaneously with the ice sheet (see the derivation for the sea level equation in Chapter 2) instead of prescribing a eustatic sea level curve.

We can only increase the model's performance in Eurasia if a self-gravitating viscoelastic earth model is used instead of a flexural model. There are strong indications of a transition in lithospheric strength between Norway and Finland, with weak lithosphere in the west and strong, cratonic lithopshere in the east. Given the sensitivity of ice sheet evolution to lithospheric strength as found in Chapters 4 and 6, it would be interesting to use an earth model which can incorporate lateral variations in earth structure and assess the ice sheet's response to these transitions.

In addition, we need more information on changes in the wind and temperature field throughout a glacial period. The best available sources of information are General Circulation Models. Runs for several time periods before and after the LGM with several different ice sheet geometries may provide information on local temperature perturbations and changes in the large scale wind field.

Based on our results for the Eurasian Ice Sheet, we expect that the results of this thesis also apply to other ice sheets. For example, the Laurentide Ice Sheet is especially interesting for two reasons; firstly its size, which was about three times the size of the Eurasian Ice Sheet at the LGM. As this ice sheet completely disappears during interglacials it is responsible for the largest eustatic change in sea level of all the Quaternary ice sheets, including Antarctica. Secondly, its similarities in ice dynamical characteristics. The Lau-

rentide Ice Sheet was land-based and governed by ice flow and ablation, just like the Eurasian Ice Sheet. We expect that the calculation of any ice sheet which evolves through a large series of sizes in a glacial-interglacial is sensitive to the differences between the SGVE and ELRA models, but especially an ice sheet that starts a new glacial period without ice. Taking all this into account, we feel that the Laurentide Ice sheet could be an interesting case study for future research.

Bibliography

Andrews, J. T. (1968). Postglacial rebound in Arctic Canada: similarity and prediction of uplift curves. *Canad. J. Earth Sc.*, 5:39–47.

Audet, P. and Marechal, J. (2004). Variations in elastic thickness in the Canadian Shield. *Earth and Planet. Sc. Lett.*, 226:17–31.

Bannister, S., Yu, J., Leitner, B., and Kennett, B. L. N. (2003). Variations in crustal structure across the transition from West to East Antarctica, Southern Victoria Land. *Geophys. J. Int.*, 155:870–884.

Bassett, S., Milne, G. A., Mitrovica, J. X., and Clark, P. U. (2005). Ice Sheet and Solid Earth Influences on Far-Field Sea-Level Histories. *Science*, 309:925–928.

Bintanja, R., van de Wal, R. S. W., and Oerlemans, J. (2002). Global ice volume variations through the last glacial cycle simulated by a 3-D ice-dynamical model. *Quaternary International*, 95:11–23.

Bintanja, R., van de Wal, R. S. W., and Oerlemans, J. (2005). Modelled atmospheric temperatures and global sea levels over the past million years. *Nature*, 437:125–128.

Braitenberg, C., Ebbing, J., and Gotze, H. (2002). Inverse modelling of elastic thickness by convolution method- the eastern Alps as a case example. *Earth and Planet. Sc. Lett.*, 202:387–404.

Braithwaite, R. J. (1995). Positive degree-day factors for ablation on the Greenland ice sheet studied by energy-balance modelling. *J. of glaciology*, 41:153–160.

Brotchie, J. F. and Silvester, R. (1969). On Crustal Flexure. *J. Geophys. Res.*, 74, No. 22:5240–5252.

Bueler, E., Lingle, C., Kallen-Brown, J., Covey, D., and Bowman, L. (In press). Exact solutions and verification of numerical models for isothermal ice sheets. *J. of glaciology*.

Calov, R. and Hutter, K. (1996). The thermomechanical response of the Greenland ice sheet to various climate scenarios. *Clim.Dyn.*, 12:243–260.

Cathles, L. M. (1975). *The Viscosity of the Earth's Mantle*. Princeton University Press, New Jersey.

Charbit, S., Ritz, C., and Ramstein, G. (2002). Simulations of Northen Hemisphere ice-sheet retreat: sensitivity to physical mechanisms involved during the Last Deglaciation. *Quaternary Science Reviews*, 21:243–265.

Clark, P. U., Mitrovica, J. X., Milne, G. A., and Tamiseia, M. (2002). Sea-Level Fingerprinting as a Direct Test for the Source of Global Meltwater Pulse IA. *Science*, 295:2438–2441.

Crucifix, M., Loutre, M., Lambeck, K., and Berger, A. (2001). Effect of isostatic rebound on modelled ice volume variations during the last 200 kyr. *Earth and Planet. Sc. Lett.*, 184:623–633.

Darbyshire, F. A., Larsen, T. B., Mosegaard, K., Dahl-Jensen, T., Gudmundsson, O., Bach, T., Gregersen, S., Pedersen, H. A., and Hanka, W. (2004). A first detailed look at the Greenland lithosphere and upper mantle using Rayleigh wave tomography. *Geophys. J. Int.*, 158:267–286.

Di Donato, G., Vermeersen, L. L. A., and Sabadini, R. (2000). Sea-level changes, geoid and gravity anomalies due to Pleistocene deglaciation by means of multilayered, analytical Earth models. *Tectonophysics*, 320:409–418.

Dziewonski, A. M. and Anderson, D. L. (1981). Preliminary reference earth model (PREM). *Phys. of the Earth and Planet. Int.*, 25:297–356.

EPICA Community Members (2004). Eight glacial cycles from an Antarctic ice core. *Nature*, 429:623–629.

Fabre, A., Ritz, C., and Ramstein, G. (1997). Modelling of Last Glacial Maximum ice sheets using different accumulation parameterizations. *Ann. of Glaciology*, 24:223–228.

Farrell, W. E. (1972). Deformation of the Earth by surface loads. *Rev. Geophys. Space Phys.*, 10:761–797.

Farrell, W. E. and Clark, J. A. (1976). On Postglacial Sea Level. *Geophys. J. R. astr. Soc.*, 46:647–667.

Fastook, J. L. and Chapman, J. E. (1989). A map-plane finite-element model: three modeling experiments. *J. of glaciology*, 35(119):48–52.

Fjeldskaar, W. (1997). Flexural rigidity of Fennoscandia inferred from the postglacial uplift. *Tectonics*, 16(4):596–608.

Forsström, P. J. and Greve, R. (2004). Simulation of the Eurasian ice sheet dynamics during the last glaciation. *Global and Planetary Change*, 42:59–81.

Ghil, M. and Le Treut, H. (1981). A climate model with cryodynamics and geodynamics. *J. Geophys. Res.*, 86:5262–5270.

Greve, R. (1997). A continuum-Mechanical Formulation for Shallow Polythermal Ice Sheets. *Phil. Trans. R. Soc. Lond. A*, 355(1726):921–974.

Greve, R. and Calov, R. (2002). Comparison of numerical schemes for the solution of the ice-thickness equation in a dynamic/thermodynamic ice-sheet model. *J. Comput. Phys.*, 179:649–664.

Grootes, P. M., Stuiver, M., White, J. W. C., Johnsen, S., and Jouzel, J. (1993). Comparison of oxygen isotope records from the GISP2 and GRIP Greenland ice cores. *Nature*, 366:552–554.

Hindmarsh, R. and Payne, A. (1996). Time-step limits for stable solutions of the ice-sheet equation. *Ann. of Glaciology*, 23:74–85.

Hulton, N. R. J. and Sugden, D. E. (1995). Modeling mass balance on former maritime ice caps: a Patagonian exaple. *Ann. of Glaciology*, 21:304–310.

Hutter, K. (1983). *Theoretical glaciology*. Reidel, Dordrecht.

Huybrechts, P. (1990). A 3-D model for the Antarctic ice sheet: a sensitivity study on the glacial-interglacial contrast. *Clim.Dyn.*, 5:79–92.

Huybrechts, P. (1992). The Antarctic ice sheet and environmental change: a three-dimensional modelling study. *Reports on polar research*, 99.

Huybrechts, P. (2002). Sea-level changes at the LGM from ice-dynamic reconstructions of the Greenland and Antarctic ice sheets during the glacial cycles. *Quaternary Science Reviews*, 21:203–231.

Huybrechts, P. and de Wolde, J. (1999). The dynamic response of the Greenland and Antarctic ice sheets to multiple-century climatic warming. *J. Climate*, 12:2169–2188.

Huybrechts, P., Gregory, J., Janssens, I., and Wild, M. (2004). Modelling Antarctic and Greenland volume changes during the 20th and 21st centuries forced by GCM time slice integrations. *Global and Planetary Change*, 42:83–105.

Huybrechts, P., Payne, T., and The EISMINT Intercomparison Group (1996). The EISMINT benchmarks for testing ice-sheet models. *Ann. of Glaciology*, 23:1–12.

Kaufmann, G. and Wu, P. (2002). Glacial isostatic adjustment in Fennoscandia with a three-dimensional viscosity structure as an inverse problem. *Earth and Planet. Sc. Lett.*, 197:1–10.

Kaufmann, G., Wu, P., and Ivins, E. R. (2005). Lateral viscosity variations beneath Antarctica and their implications on regional rebound motions and seismotectonics. *J. Geodyn.*, 39:165–181.

Kaufmann, G., Wu, P., and Li, G. (2000). Glacial isostatic adjustment in Fennoscandia for a laterally heterogeneous earth. *Geophys. J. Int.*, 143:262–273.

Krinner, G., Boucher, O., and Balkanski, Y. (2006). Ice-free glacial northern Asia due to dust deposition on snow. *Clim. Dyn.*, 27:613–625.

Lambeck, K. and Chappell, J. (2001). Sea level change through the last glacial cycle. *Science*,

292:679–686.

Lambeck, K., Purcell, A., Funder, S., Kjaer, K. H., Larsen, E., and Möller, P. (2006). Constraints on the Late Saalian to early Middle Weichselian ice sheet of Eurasia from field data and rebound modelling. *Boreas*, 35:539–575.

Lambeck, K., Smither, C., and Ekman, M. (1998a). Tests of glacial rebound models for Fennoscandinavia based on instrumental sea- and lake-level records. *Geophys. J. Int.*, 135:375–387.

Lambeck, K., Smither, C., and Johnston, P. (1998b). Sea-level change, glacial rebound and mantle viscosity for northern Europe. *Geophys. J. Int.*, 134:102–144.

Le Meur, E. (1996). Isostatic postglacial rebound over Fennoscandia with a self-gravitating spherical visco-elastic earth model. *Ann. of Glaciology*, 23:318–327.

Le Meur, E. (2001). Effects of a Viscoelastic Lithosphere on the Isostatic Bedrock Response. *Earth and Planet. Sc. Lett.*, 188:221–227.

Le Meur, E. and Huybrechts, P. (1996). A comparison of different ways of dealing with isostasy: examples from modelling the Antarctic ice sheet during the last glacial cycle. *Ann. of Glaciology*, 23:309–317.

Le Meur, E. and Huybrechts, P. (1998). Present-day uplift patterns over Greenland from a coupled ice-sheet/visco- elastic bedrock model. *Geoph. Res. Letters*, 25 no. 21:3951–3954.

Le Treut, H. and Ghil, M. (1983). Orbital forcing, climatic interactions and glaciation cycles. *J. Geophys. Res.*, 88:5167–5190.

Letréguilly, A. and Ritz, C. (1993). Modelling of the Fennoscandian ice sheet. *Ice in the climate system, ed. W.R. Peltier*, NATO ASI series I: Global Environmental change12:21–46.

Leysinger Vieli, G. and Gudmundsson, G. (2004). On estimating length fluctuations of glaciers caused by changes in climatic forcing. *J. Geophys. Res.*, 109:F01007, 10.1029/2003JF000027.

Longman, I. M. (1963). A Green's Function for Determining the Deformation of the Earth under Surface Mass Loads. *J. Geophys. Res.*, 68, no. 2:485–496.

Mahaffy, M. W. (1976). A three-dimensional numerical model of ice sheets: tests on the Barnes ice cap, Northwest Territories. *J. Geophys. Res.*, 81(6):1059–1066.

Mangerud, J. (2004). Ice sheet limits in Norway and on the Norwegian continental shelf. *Quaternary Glaciations-Extent and Chronology. Part I: Europe (Developments in Quaternary Science, Volume 2*.

Milne, G. A., Davis, J. L., Mitrovica, J. X., Scherneck, H. G., Johansson, J. M., Vermeer, M., and Koivula, H. (2001). Space-Geodetic Constraints on Glacial Isostatic Adjustment in Fennoscandia. *Science*, 291:2381–2385.

Milne, G. A., Mitrovica, J. X., Davis, J. L., Scherneck, H. G., Johansson, J. M., Ekman, M., and Koivula, H. (2004). Continuous GPS measurements of Postglacial Adjustment in Fennoscandia. *J. Geophys. Res.*, 109:doi:10.1029/2003JB002619.

Milne, G. A., Mitrovica, J. X., and Schrag, D. P. (2002). Estimating past continental ice volume from sea-level data. *Quaternary Science Reviews*, 21:361–376.

Mitrovica, J. X., Davis, J. L., and Shapiro, I. I. (1994). A spectral formalism for computing three-dimensional deformations due to surface loads - I. Theory. *J. Geophys. Res.*, 99:7057–7073.

Mitrovica, J. X. and Forte, A. M. (1997). Radial profile of mantle viscosity: results from the joint inversion of convection and postglacial rebound observables. *J. Geophys. Res.*, 102:2751–2769.

Mitrovica, J. X. and Forte, A. M. (2004). A new inference of mantle viscosity based upon joint inversion of convection and glacial isostatic adjustment data. *Earth and Planet. Sc. Lett.*, 225:177–189.

Mitrovica, J. X., Tamiseia, M. E., Davis, J. L., and Milne, G. A. (2001). Recent Mass Balance of Polar Ice Sheets Inferred from Patterns of Global Sea-Level Change. *Nature*,

409:1020–1029.

Näslund, J. O., Rodhe, L., Fastook, J. L., and Holmlund, P. (2003). New ways of studying ice sheet flow directions and glacial erosion by computer modelling-examples from Fennoscandia. *Quaternary Science Reviews*, 22:245–258.

Oerlemans, J. (1980). Model experiments on the 100,000-yr glacial cycle. *Nature*, 287:430–432.

Oerlemans, J. (1981a). Modeling of Pleistocene European Ice Sheets: Some Experiments with Simple Mass-Balance Parameterizations. *Quaternary Res.*, 15:77–85.

Oerlemans, J. (1981b). Some basic experiments with a vertically-integrated ice sheet model. *Tellus*, 33:1–11.

Oerlemans, J. (2001). *Glaciers and Climate Change*. A.A. Balkema, Lisse.

Oerlemans, J. and van der Veen, C. J. (1984). *Ice Sheets and Climate*. D. Reidel Publishing Company, Dordrecht Holland.

Paterson, W. S. B. (1994). *The physics of glaciers*. Pergamon, Oxford.

Paul, A. (1996). A seasonal energy-balance climate model for coupling to ice-sheet models. *Ann. of Glaciology*, 23:174–180.

Payne, A. J., Huybrechts, P., Abe-Ouchi, A., Calov, R., Fastook, J. L., Greve, R., Marshall, S. J., Marsiat, I., Ritz, C., Tarasov, L., and Thomassen, M. P. A. (2000). Results from the EISMINT model intercomparison: the effects of thermomechanical coupling. *J. of glaciology*, 46:227–238.

Peltier, W. R. (1974). The Impulse Response of a Maxwell Earth. *Rev. Geophys. Space Phys.*, 12, no. 4:649–669.

Peltier, W. R. (1994). Ice Age Paleotopography. *Science*, 265:195–201.

Peltier, W. R. (2002). On eustatic sea level history: Last Glacial Maximum to Holocene. *Quaternary Science Reviews*, 21:377–396.

Peltier, W. R. (2004). Global Glacial Isostasy and the Surface of the Ice-Age Earth: The ICE-5G (VM2) Model and GRACE. *Annu. Rev. Earth Planet. Sci.*, 32:111–149.

Peltier, W. R. and Fairbanks, R. G. (2007). Global ice volume and Last Glacial Maximum duration from an extended Barbados sea level record. *Quaternary Science Reviews*, 25:3322–3337.

Pérez-Gussinye, M. and Watts, A. B. (2005). The long-term strength of Europe and its implications for plate-forming processes. *Nature*, 436:381–384.

Petit, J. R., Jouzel, J., Raynaud, D., Barkov, N. I., Barnola, J. M., Basile, I., Benders, M., Chappellaz, J., Davis, M., Delaygue, G., Delmotte, M., Kotlyakov, V. M., Legrand, M., Lipenkov, V. Y., Lorius, C., Pépin, L., Ritz, C., Saltzman, E., and Stievenard, M. (1999). Climate and atmospheric history of the past 420,000 years from the Vostok ice core, Antarctica. *Nature*, 399:429–436.

Pfeffer, W. T., Sassolas, C., Bahr, D. B., and Meier, M. F. (1998). Response time of glaciers as a function of size and mass balance: 2. Numerical experiments. *J. Geophys. Res.*, 103(B5):9783–9789.

Plummer, M. A. and Philips, F. M. (2003). A 2-D numerical model of snow/ice energy balance and ice flow for paleoclimatic interpretation of glacial geomorphic structures. *Quaternary Science Reviews*, 22:1389–1406.

Pollard, D. (1980). A simple parameterization for ice sheet ablation rate. *Tellus*, 32:384–388.

Pollard, D. and Thompson, S. L. (1997). Driving a high-resolution dynamic ice-sheet model with GCM climate: ice-sheet initiation at 116000 BP. *Ann. of Glaciology*, 25:296–304.

Poudjom Djomani, Y. H., Fairhead, J. D., and Griffin, W. L. (1999). The flexural rigidity of Fennoscandia: reflection of the tectonothermal age of the lithospheric mantle. *Earth and Planet. Sc. Lett.*, 174:139–154.

Purves, R. S. and Hulton, N. R. J. (2000). A climatic-scale precipitation model compared with UKCIP baseline climate. *Int. J. of Clim.*, 20:1809–2821.

Reeh, N. (1991). Parameterization of Melt Rate and Surface Temperature on the Greenland Ice Sheet. *Polarforschung*, 59:113–128.

Rennick, M. A. (1979). The parameterization

of tropospheric lapse rates in terms of surface temperature. *J. Atmos. Sci.*, 36:854–862.

Saltzman, B. (2002). *Dynamical Paleoclimatology, generalized theory of global climate change*, volume 80 of *International Geophysics series*. Academic Press.

Sanberg, J. A. M. and Oerlemans, J. (1983). Modelling of Pleistocene European ice sheets: the effect of upslope precipitation. *'Geologie en Mijnbouw'*, 62:267–273.

Siegert, M. J., Dowdeswell, J. A., Hald, M., and Svendsen, J. I. (2001). Modelling the Eurasian Ice Sheet through a full (Weichselian) glacial cycle. *Global and Planetary Change*, 31:367–385.

Spada, G., Antonioli, A., Cianetti, S., and Giunchi, C. (2006). Glacial isostatic adjustment and relative sea-level changes: the role of lithospheric and upper mantle heterogeneities in a 3-D spherical Earth. *Geophys. J. Int.*, 165:692–702.

Stern, T. A. and Ten Brink, U. S. (1989). Flexural Uplift of the Transantarctic Mountains. *J. Geophys. Res.*, 94, No. B8:10,315–10,330.

Svendsen, J. I., Alexanderson, H., Astakhov, V. I., Demidov, I., Dowdeswell, J. A., Funder, S., Gataullin, V., Henriksen, M., Hjort, C., Houmark-Nielsen, M., Hubberten, H. W., Ingólfsson, O., Jacobsson, M., Kjaer, K. H., Larsen, E., Lokrantz, H., Pekka Lunkka, J., Lysa, A., Mangerud, J., Matiouchkov, A., Murray, A., Möller, P., Niessen, F., Nikolskaya, O., Polyak, L., Saarnisto, M., Siegert, C., Siegert, M. J., Spielhagen, R. F., and Stein, R. (2004). Late Quaternary ice sheet history of northern Eurasia. *Quaternary Science Reviews*, 23:1229–1271.

Tamiseia, M. E., Mitrovica, J. X., Davis, J. L., and Milne, G. A. (2003). Long wavelength sea level and solid surface perturbations driven by polar ice mass variations: Fingerprinting Greenland and Antarctic ice sheet flux. *Space Science Reviews*, 108:81–93.

Tarasov, L. and Peltier, W. R. (1997). A high-resolution model of the 100 ka ice-age cycle. *Ann. of Glaciology*, 25:58–65.

Tarasov, L. and Peltier, W. R. (2002). Greenland glacial history and local geodynamic consequences. *Geophys. J. Int.*, 150:198–229.

Turcotte, D. L. and Schubert, G. (2002). *Geodynamics, 2nd edition*. Cambridge University Press.

Tushingham, A. M. and Peltier, W. R. (1991). Ice-3G: A New Global Model Of Late Pleistocene —Deglaciation Based Upon Geophysical Predictions Of post-Glacial Relative Sea Level Change. *J. Geophys. Res.*, 96, No. B3:4497–4523.

Van de Plassche, O., editor (1986). *Sea-level Research: A Manual for the Collection and Evaluation of Data*. Geobooks, Norwich.

Van de Wal, R. S. W. (1999). The importance of thermodynamics for modeling the volume of the Greenland ice sheet. *J. Geophys. Res.*, 104, No. D4:3887–3898.

Van de Wal, R. S. W. and Ekholm, S. (1996). On elevation models as input for mass-balance calculations of the Greenland ice sheet. *Ann. of Glaciology*, 23:181–186.

Van de Wal, R. S. W., Wild, M., and de Wolde, J. (2001). Short-term volume changes of the Greenland ice sheet in response to doubled CO_2 conditions. *Tellus*, 53B:94–102.

Van den Berg, J., van de Wal, R. S. W., Milne, G. A., and Oerlemans, J. (2007). The effect of isostasy on dynamical ice sheet modelling; a case study for Eurasia. *Submitted to Journal of Geophysical Research*.

Van den Berg, J., van de Wal, R. S. W., and Oerlemans, J. (2006a). Effects of spatial discretization in ice sheet modelling using the shallow-ice approximation. *J. of glaciology*, 52(176):89–98.

Van den Berg, J., van de Wal, R. S. W., and Oerlemans, J. (2006b). A mass balance model for the Eurasian ice sheet for the last 120 000 years. *Submitted to Global and Planetary Change*.

Van der Veen, C. J. (1999). *Fundamentals of Glacier Dynamics*. A.A. Balkema, Rotterdam.

Van Wees, J. D. and Cloetingh, S. (1994). A finite-difference technique to incorporate spatial variations in rigidity and planar faults into

3-D models for lithospheric flexure. *Geophys. J. Int.*, 117:179–195.

Velichko, A. A., Kononov, Y. M., and Faustova, M. A. (1997). The last glaciation of Earth: size and volume of ice-sheets. *Quat. Int.*, 41/42:43–51.

Vermeersen, L. L. A. and Sabadini, R. (1999). Polar wander, sea-level variations and ice age cycles. *Surveys in Geophysics*, 20:415–440.

Walcott, R. I. (1970a). Flexural rigidity, Thickness and Viscosity of the Lithosphere. *J. Geophys. Res.*, 75:3941–3954.

Walcott, R. I. (1970b). Isostatic response to loading of the crust in Canada. *Canad. J. Earth Sc.*, 7:716–734.

Watts, A. B. (2001). *Isostasy and Flexure of the Lithosphere*. Cambridge University Press.

Weertman, J. (1961). Stability of Ice-Age Ice Sheets. *J. Geophys. Res.*, 66(11):3783–3792.

Wieczerkowski, K., Mitrovica, J. X., and Wolf, D. (1999). A revised relaxation-spectrum for Fennoscandia. *Geophys. J. Int.*, 139:69–86.

Wolf, D. (1993). The changing role of the lithosphere in models of glacial isostasy: a historical review. *Global and Planetary Change*, 8:95–106.

Wu, P., editor (1998). *Dynamics of the ice age earth*. Trans Tech Publications, Zurich, Switzerland.

Wu, P. and Peltier, W. R. (1982). Viscous gravitational relaxation. *Geophys. J. R. astr. Soc.*, 70:435–485.

Zhong, S., Paulson, A., and Wahr, J. (2003). Three-dimensional finite-element modelling of Earth's viscoelastic deformation: effects of lateral variations in lithospheric thickness. *Geophys. J. Int.*, 155:679–695.

Zienkiewicz, O. C. and Taylor, R. L. (2000). *The finite element method*, volume 2: solid mechanics. Butterworth-Heinemann, Oxford, 5th edition.

Zweck, C. and Huybrechts, P. (2003). Modeling the marine extent of Northern Hemisphere ice sheets during the last glacial cycle. *Ann. of Glaciology*, 37:173–180.

Zweck, C. and Huybrechts, P. (2005). Modeling of the northern hemisphere ice sheets during the last glacial cycle and glaciological sensitivity. *J. Geophys. Res.*, 110(D07103, doi: 10.1029/2004JD005489).

Samenvatting (Summary in Dutch)

Er is op het moment veel aandacht voor klimaatverandering en de gevolgen daarvan voor de mens. Wanneer we het over klimaatverandering in Nederland hebben, wordt meestal naadloos de aansluiting gemaakt naar zeespiegelstijging. Gezien de lage ligging van Nederland is het erg belangrijk om te voorspellen wat er de komende paar honderd jaar met de zeespiegel gaat gebeuren.

Gedurende de hele geschiedenis van de aarde zijn er fluctuaties in het klimaat geweest. Er zijn aanwijzingen dat de aarde meerdere malen volledig met ijs bedekt is geweest, terwijl in andere tijden de aarde helemaal ijsvrij en warmer was dan tegenwoordig. Het klimaat van de laatste miljoen jaar wordt gekenmerkt door de opeenvolging van ijstijden. Een ijstijd duurt ongeveer 100,000 jaar waarin de temperatuur gemiddeld zo'n 15 tot 20 graden lager ligt dan nu, waarna er een relatief snelle opwarming plaatsvindt. Op dit moment bevinden we ons in zo'n warme periode tussen twee ijstijden in. Volgens sommige wetenschappers zou er zo langzamerhand weer een nieuwe ijstijd kunnen beginnen, volgens anderen kan het nog wel 20,000 jaar of langer duren. Duidelijk is dat het begrip ijstijd verbonden is met tijdschalen vele malen langer dan een mensenleven.

Maar ook op kortere tijdschalen fluctueert het klimaat. Gedurende de Middeleeuwen was er een warme periode van bijna 100 jaar, terwijl er in de achttiende eeuw juist een koude periode was die we de Kleine IJstijd noemen. Uit die tijd stammen veel beroemde schilderijen met ijstaferelen en veel gletsjers in de Alpen hadden toen een lengte die daarna nooit meer gehaald is. Deze klimaatfluctuaties zijn niet of nauwelijks beïnvloed door de aanwezigheid van de mens. Sinds de tweede helft van de negentiende eeuw, de start van het industriële tijdperk, zijn we echter begonnen met de grootschalige uitstoot van broeikasgassen, zoals koolstofdioxide, door de verbranding van koolwaterstoffen zoals aanwezig in kolen, olie en gas.

De aanwezigheid van broeikasgassen in de atmosfeer is op zichzelf niet bijzonder en zelfs essentieel voor het leven op onze planeet. Broeikasgassen houden warmte een tijdje vast in de atmosfeer, waardoor het aardoppervlak opwarmt. Zonder broeikasgassen zou de aarde zo'n 30 graden kouder zijn dan nu het geval is. Vergelijk dat met een afkoeling van zo'n 20 graden tijdens een grote ijstijd en het is duidelijk dat met 30 graden afkoeling de aarde vrijwel onleefbaar zou worden. De continue toevoeging van broeikasgassen aan de atmosfeer door de mens vergroot echter voortdurend de warmtecapaciteit van de atmosfeer wat tot verdere opwarming leidt. Deze niet-natuurlijke klimaatverandering heeft potentieel grote gevolgen voor onze samenleving. De temperaturen nemen toe, er is meer energie voor wind en verdamping, en grote klimaatsystemen zoals bijvoorbeeld de moesson veranderen. Een groot deel van de mensheid woont in kustgebieden vanwege de gunstige locatie voor handel en de vruchtbare grond in rivierdelta's. Opwarming van de aarde heeft ook gevolgen voor de zeespiegel; het water warmt op en zet uit, en het aanwezige

ijs, in de vorm van gletsjers en ijskappen op Antarctica en Groenland, gaat smelten.

Volgens het laatst verschenen klimaatrapport (IPCC (2007)) waarin de wetenschappelijke consensus over de klimaatverandering beschreven staat, is de huidige zeespiegelstijging zo'n 3.1 mm per jaar. Grofweg 20 procent van deze stijging wordt veroorzaakt door de ijskappen op Groenland en Antarctica. Maar er is een grote onzekerheid in deze getallen. IJskappen reageren op een complexe manier op veranderingen in temperatuur. In zijn algemeenheid geldt dat hoe groter het ijslichaam, hoe langer het duurt voor het ijs weer in evenwicht is met het heersende klimaat na een temperatuurfluctuatie. Bijvoorbeeld, een blok ijs dat uit de vriezer wordt gehaald smelt binnen een paar uur op een zomerse dag. Gletsjers reageren binnen tientallen jaren op klimaatverandering, terwijl de ijskappen op Antarctica en Groenland honderden tot duizenden en tienduizenden jaren nodig hebben om een nieuw evenwicht te bereiken. De ijskappen op Groenland en Antarctica reageren dus nog steeds op klimaatfluctuaties uit het verleden. Tegelijk reageren ze ook op hedendaagse klimaatschommelingen. Dit levert een zeer complexe respons op.

Om de zeespiegelstijging voor de komende eeuwen te kunnen voorspellen is het dus niet alleen belangrijk om het klimaat goed te voorspellen, we moeten ook begrijpen hoe ijskappen op die klimaatveranderingen reageren. In dit proefschrift wordt bestudeerd welke fysische processen belangrijk zijn voor ijskappen en hoe die processen elkaar beïnvloeden.

We focussen onze aandacht op de laatste ijstijd. Tijdens de laatste ijstijd lag er voor ongeveer 130 meter globale zeespiegel meer in landijs opgeslagen dan nu. Ter vergelijking, als de ijskap op Antarctica nu zou smelten, zou er voor ongeveer 60 meter aan globale zeespiegel bijkomen. Dit ijs lag verdeeld over een aantal grote ijskappen op Antarctica, Groenland, Canada en Noord-Europa. Deze ijskappen smolten over een periode van 10,000 jaar weg tot de ijskappen die we nu nog over hebben. Dit representeert een veel grotere verandering dan die paar millimeters per jaar die we tegenwoordig waarnemen. Dit maakt de ijstijden zeer geschikt om te leren hoe ijskappen reageren op klimaatverandering. Daarnaast moeten we de onzekerheid in de huidige schattingen van zeespiegelstijging terugbrengen door de lange termijn respons van de ijskappen te bestuderen. Als laatste zijn er van de laatste ijstijd een heleboel data beschikbaar over het toen heersende klimaat, de geometrie van de ijskappen en de zeespiegel.

Er zijn data over klimaat uit het verleden in de vorm van ijskernen. De samenstelling van het ijs geeft informatie over de temperaturen tijdens de vorming van het ijs en in het ijs zijn luchtbelletjes opgeslagen die directe informatie geven over de toenmalige samenstelling van de atmosfeer. Op het land hebben de ijskappen sporen achtergelaten, zoals bijvoorbeeld de stuwwallen en zwerfkeien. Ook zijn er veel data over de zeespiegel, bijvoorbeeld in de vorm van oude stranden en bodemtypen. Door deze data hebben we een goede indruk hoe de ijskappen uit de laatste ijstijd er ongeveer uitzagen en welk klimaat er ongeveer heerste. Alleen zijn data niet volledig; ze geven ons ten eerste geen volledig beeld van het klimaat en de ijskappen uit het verleden, en ten tweede geven ze ons ook niet het inzicht in de fysische processen dat nodig is om toekomstige zeespiegelfluctuaties te kunnen voorspellen. In dit proefschrift wordt daarom gebruik gemaakt van numerieke modellen.

Een model is een wiskundige versimpeling van de werkelijkheid. Modellen die ijskap-

pen beschrijven kunnen vrijwel nooit direct en/of snel uitgerekend worden vanwege de complexiteit van de wiskundige vergelijkingen en vanwege de lange tijdschalen waarop gerekend wordt. Daarom worden computers gebruikt waarin het wiskundige model numeriek benaderd wordt. De nauwkeurigheid van de oplossing hangt af van hoe goed die benaderde vergelijkingen het oorspronkelijke systeem beschrijven. Daarnaast is er een belangrijk verschil tussen wiskundige vergelijkingen en numerieke vergelijkingen; wiskundige vergelijkingen zijn analoog, terwijl een computer vergelijkingen alleen discreet kan oplossen. In het algemeen wordt daarom een grid geformuleerd waarop de oplossing van het systeem bepaald wordt. Hoe fijner het grid, hoe dichter de oplossing bij de analoge oplossing komt. Naast de juistheid van de benaderingen voor de vergelijkingen wordt de nauwkeurigheid van de numerieke oplossing dus ook bepaald door de fijnheid of resolutie van het grid. In hoofdstuk 2 en 3 van dit proefschrift wordt aandacht besteed aan de set wiskundige vergelijkingen en de werking van het computermodel.

De vorm en grootte van een ijskap is van verschillende processen afhankelijk die elkaar onderling weer beïnvloeden; het klimaat, de materiaaleigenschappen van het ijs en de deformatie van de aarde. In het algemeen wordt ijs gevormd in koude, vaak hoge gebieden waar sneeuw valt die niet volledig wegsmelt in de zomer. Het ijs stroomt als een zeer stroperige vloeistof onder de invloed van zwaartekracht naar lager gelegen of warmere gebieden. Dit proces gaat over tijdschalen van tientallen tot duizenden jaren tot het ijs uiteindelijk smelt of in zee stroomt en afbreekt in de vorm van ijsbergen. Het is duidelijk dat dit proces wordt gedomineerd door de hoeveelheid sneeuw, de temperaturen en de snelheid waarmee het ijs stroomt. Dit laatste wordt bepaald door de materiaaleigenschappen van ijs. Minder herkenbaar op het eerste gezicht is het effect van de respons van de vaste aarde.

Een ijskap zoals op Groenland en Antarctica is typisch zo'n 3 kilometer dik en heeft een doorsnede van een paar duizend kilometer. Het gewicht van deze ijsmassa vormt een grote belasting voor de aarde. Net zoals stroop en ijs kan de aarde deformeren, oftewel van vorm veranderen, over lange tijdschalen. Als een groot gewicht op de aarde wordt gelegd, reageert de aarde volgens de wet van Archimedes. Dit is vergelijkbaar met het gewicht van een schip in water; het schip zakt naar beneden en het water onder het schip wordt verplaatst totdat de druk van de omgeving op een bepaalde diepte net zo groot is als de druk van het schip. De aarde reageert op een vergelijkbare manier op het gewicht van een ijskap. In plaats van water bestaat de aarde uit gesteente. De aarde kan grofweg worden verdeeld in drie schillen; het binnenste deel van de aarde is een ijzeren kern met een straal van bijna 3000 kilometer. De kern is omgeving door een mantel van gesteente van ook ongeveer 3000 kilometer dikte. Dit gesteente is stroperig van aard door de hoge druk en temperatuur. Het buitenste dunne laagje van ongeveer 100 kilometer is de korst. Water reageert instantaan op drukverschillen, maar gesteente reageert over duizenden jaren. Een ijstijd van 100,000 jaar is dus lang genoeg om dit soort deformatie te induceren. Door de dichtheidsverschillen tussen ijs en aarde kan een ijskap typisch een kilometer diep wegzakken. Als de ijskap smelt, komt ook het land weer omhoog, een proces dat nog steeds duidelijk zichtbaar is in Scandinavië, dat nog steeds met een paar millimeters per jaar omhoog komt door het verdwijnen van de Europese ijskap zo'n 10,000 jaar geleden.

Dit naar beneden zakken van het aardoppervlak door het gewicht van het ijs, ook

wel isostasie genoemd, heeft een wisselwerking met het ijs. In het algemeen neemt de temperatuur af met de hoogte. Als een ijskap met het aardoppervlak mee naar beneden zakt, komt de ijskap op elevaties te liggen met hogere temperaturen. Dit kan meer smelt opleveren, maar er kan ook meer sneeuw vallen, aangezien een warmere atmosfeer meer vocht kan bevatten. Isostasie bepaalt dus mede aan welk klimaat de ijskap wordt blootgesteld en is daarmee een proces dat goed bestudeerd moet worden. Het begrijpen van de wisselwerking tussen aarde en ijs is het voornaamste doel van dit proefschrift.

Het complete model om de evolutie van ijskappen te simuleren met behulp van de computer bestaat uit grofweg drie grote modulen; de eerste bevat de fysica van het ijs zelf en is daarmee de basismodule die ijsdikte berekent als functie van de andere twee modules, de tweede beschrijft temperatuur en neerslag plus de wisselwerking met het ijs, en de derde beschrijft de respons van de aarde. In het proefschrift wordt aandacht besteed aan elk van die drie modules. In hoofdstuk 3 wordt gekeken naar de technische werking van de basismodule. Er wordt daar bekeken waaraan een goed grid moet voldoen en wanneer er problemen te verwachten zijn met de oplossing. Dit is belangrijk, we moeten weten of het model de correcte oplossing voorspelt voor we de wisselwerking met fysische processen kunnen begrijpen,

In hoofdstuk 4 wordt een aardmodel beschreven dat realistische variaties in aardstructuur kan meenemen. Met schematische experimenten is vervolgens bekeken of zeespiegeldata gevoelig zijn voor aardstructuur en hoe de ijskappen reageren op variaties in die structuur. Het blijkt dat zeespiegeldata zeer gevoelig zijn voor aardstructuur. Grote variaties in aardstructuur zijn zichtbaar in de data zolang er maar genoeg nauwkeurige data zijn rondom die variaties. Ook de ijskappen zelf blijken gevoelig voor veranderingen in aardstructuur, zowel de ijsdikte als de omvang de ijskappen varieerde als functie van de aardstructuur. De resultaten van deze tests met schematische experimenten zijn echter niet eenvoudig door te rekenen naar de werkelijkheid, aangezien die veel complexer is dan de schematische experimenten die hier gedaan zijn. Daarom wordt er in hoofdstuk 5 en 6 een realistische ijskap bekeken, namelijk de Noord-Europese ijskap.

De Noord-Europese ijskap is interessant vanwege de beschikbaarheid van data. Het voordeel ten opzichte van regio's als Groenland en Antarctica is dat er geen ijskap meer aanwezig is in Europa, waarmee het logistiek een stuk eenvoudiger is om data te verzamelen. Bovendien is er sinds de achttiende eeuw belangstelling voor dit onderwerp in Scandinavië, waardoor er over de loop der tijd veel data verzameld zijn. Daarnaast is de ijskap zelf ook interessant. De ijskap is gedeeltelijk op land ontstaan in de bergen in Noorwegen en Zweden en op de kust van Siberië. Gedeeltelijk echter is de ijskap ontstaan in de ondiepe Barentsz en Kara Zee rond Nova Zembla. De ijskap is daar ontstaan op de eilanden en uitgegroeid de zee in totdat een groot deel van de zee verdwenen was en vervangen door een dikke ijskap.

Om een realistische ijskap te kunnen simuleren moest er eerst aandacht worden besteed aan de tweede grote module, namelijk het lokale klimaat en de veranderingen in dat lokale klimaat door een ijstijd heen. Het hedendaagse klimaat is redelijk bekend, maar gedetailleerde klimaatwaarnemingen zijn er pas zo'n 100 jaar, wat te kort is voor de tijdschaal van 100,000 jaar voor een ijstijd. Er zijn wel data beschikbaar in de vorm van bijvoorbeeld ijskernen, maar deze zijn vaak lastig te interpreteren en bovendien zijn het maar een paar

puntwaarnemingen, die niet het hele verhaal van lokale klimaatverandering vertellen. Bijvoorbeeld, de winter van 2006-2007 is in Nederland als de warmste ooit bijgeschreven, terwijl de VS geteisterd werden door sneeuwstormen. Als er maar een waarneming uit een van beide gebieden zou zijn, zou dit een vertekend beeld van de werkelijke situatie geven. Dit is typerend voor vrijwel alle data van paleoklimaat. Daarom is het belangrijk om een zo simpel mogelijk model te construeren dat alleen de belangrijkste processen in het klimaat voor ijskappen meeneemt. Door het model simpel te houden is de kans kleiner dat gemodelleerde ijskappen heel goed lijken op de ijskap die werkelijk in Europa gelegen heeft. Daar staat tegenover dat de respons van ijskappen op veranderingen in het klimaat heel transparant is en goed te koppelen aan specifieke processen. In hoofdstuk 5 wordt zo'n model beschreven, waarbij alleen verdamping van vocht uit de oceaan en de bodem, vochttransport door wind, en neerslag worden meegenomen.

In hoofdstuk 6 wordt dat klimaatmodel vervolgens in een realistische simulatie voor de Europese ijskap gebruikt om het effect van de respons van de aarde te bestuderen. In dit hoofdstuk wordt veel aandacht besteed aan de wisselwerking tussen ijskappen en de vaste aarde. Daarnaast is bekeken hoe gedetailleerd de aarde moet worden beschreven om deze wisselwerking goed te kunnen modelleren. Een belangrijk resultaat van deze studie is dat het tot nu toe meest gebruikte aardmodel in dit soort toepassingen niet goed genoeg is om de evolutie van ijskappen op een realistische manier te beschrijven.

Dankwoord (Acknowledgments)

Ik wil op deze plaats graag iedereen bedanken die me de afgelopen jaren geholpen heeft met het stand komen van dit boekwerkje.

Als eerste wil ik graag Hans Oerlemans en Roderik van de Wal noemen. Jullie zijn altijd actief betrokken geweest bij het project, maar hebben me tegelijk gestimuleerd om zelf mijn weg te vinden. Ik heb daardoor enorm veel geleerd en het heeft me veel zelfvertrouwen gegeven. Bedankt voor het vertrouwen in een goede afloop!

Ik wil ook graag iedereen van de IJs en Klimaat groep, in wisselende samenstelling over de jaren, bedanken voor de gezellige sfeer en de altijd getoonde belangstelling voor elkaar en elkaars werk.

Glenn, I really enjoyed our working together over the last year and a half. I think we obtained nice results which form a great component of the thesis. I very much enjoyed my time in Durham, for which I also wish to thank Sarah, Pippa, Chris, Tim and Christa.

Verder wil ik iedereen op het IMAU bedanken voor alle gezelligheid tijdens koffie- en lunchpauzes, uitjes, etc. Ik wil hier ook nog even Han van Dop noemen, zonder wie ik waarschijnlijk nooit bij het IMAU terecht was gekomen, bedankt! En natuurlijk Marcel en Henk Mos, bedankt voor al jullie werk om de rekenwondertjes topfit te houden. Yvonne, dank je wel voor je behulpzaamheid en al onze gezellige praatjes.

Ik wil graag al mijn kamergenoten bedanken, Irene and Cesca, I worked only a relatively short time with you, but thank you for your cheer and laughter. Lisette en Rianne, bedankt voor alle belangstelling, hulp en gezelligheid. Ik vond (en vind) het erg leuk om jullie kamergenoot te zijn.

Bert en Hugo, bedankt voor alle discussies, sommige wat meer werk gerelateerd dan andere.

Karin, Peter, Remco, Carolien, Dirk-Jan, Idsard, Jet, Arjen, Erik, Willem Jan, Petra, Guy, Carlijn, Nick, heel erg bedankt voor alle gezelligheid tijdens de vele filmbezoeken, etentjes, spelletjesavonden en andersoortige feestjes. En bedankt voor het luisteren als er eens wat frustratie uit moest.

Iedereen van de vakgroep seismologie, bedankt voor de blijvende belangstelling en gezelligheid, ook al ben ik alweer een paar jaar weg. Ik hoop ook de komende jaren nog regelmatig langs te komen.

Lieve familie, papa en mama, bedankt voor al jullie steun. Robbert, mijn lieverd, mijn grote steun zowel rond werk als met alles daarbuiten. Dank je wel voor alles!

Curriculum vitae

Jojanneke van den Berg was born on the 31st of July 1979 in Gouda, The Netherlands. She attended the Marnix Gymnasium in Rotterdam, The Netherlands, where she obtained her 'VWO-diploma' in 1997. In the same year she commenced the study Geophysics at the University of Utrecht, The Netherlands. In 2001 she went four months to Cambridge, UK, where she worked for Schlumberger Cambridge Research as part of her Masters research on 'Bayesian experimental design'. She specialized in inverse theory, seismology and tectonophysics. In 2002 she earned her Masters Degree and commenced the PhD at the University of Utrecht as described in this thesis.

Scientific Publications

J. van den Berg, R.S.W. van de Wal, G.A. Milne and J. Oerlemans (2007). The effect of isostasy on dynamical ice sheet modelling; a case study for Eurasia. *Submitted to Journal of Geophysical Research, Solid Earth*.

J. van den Berg, R.S.W. van de Wal and J. Oerlemans (2006). A mass balance model for the Eurasian Ice Sheet for the last 120 000 years. *Submitted to Global and Planetary Change*.

J. van den Berg, R.S.W. van de Wal and J. Oerlemans (2006). Recovering lateral variations in lithospheric strength from bedrock motion data using a coupled ice sheet-lithosphere model. *J. Geophys. Res.* **111**, B05409, doi:10.1029/2005JB003790.

J. van den Berg, R.S.W. van de Wal and J. Oerlemans (2006). Effects of spatial discretization in ice-sheet modelling using the shallow ice approximation. *J. Glaciol.* **52(176)**: 89-98.

J. van den Berg, A. Curtis and J. Trampert (2005). Corrigendum to 'Optimal nonlinear Bayesian experimental design: an application to amplitude versus offset experiments (*Geophys. J. Int.* **155(2)**: 411-421)'. *Geophys. J. Int.* **161**: 265.

J. van den Berg, A. Curtis and J. Trampert (2003). Optimal nonlinear Bayesian experimental design: an application to amplitude versus offset experiments. *Geophys. J. Int.* **155(2)**: 411-421.